UNIVERSITÀ DEGLI STUDI DI TRIESTE

XXIII CICLO DEL
DOTTORATO DI RICERCA IN FISICA

# Disclosing the ultrafast dynamics of competing phases in high-temperature superconductors by time-resolved optical spectroscopy


Giacomo Coslovich

Anno Accademico 2009-2010

Responsabile del Dottorato di Ricerca:
Prof. Paolo Camerini

Relatore:
Prof. Fulvio Parmigiani

Referees:
Prof. Michele Fabrizio
Prof. Dr. Uwe Bovensiepen

Membri della Commissione:
Prof. Alberto Morgante
Prof. Michele Fabrizio
Prof. Francesco Ancilotto

(supplenti)
Prof. Silvio Modesti
Prof. Sandro Sorella
Prof. Lapo Casetti

Data Esame Finale: 23 Marzo 2011

# Abstract

Understanding the interplay between the phases present in a high-temperature superconductor (superconducting, pseudogap, strange metal and Fermi-liquid-like) is the key-concept for shining light on the nature of the superconductivity mechanisms in copper-oxide based superconductors.

Here, I set the bases for addressing this physics by developing an approach based on ultrafast time-resolved optical spectroscopy in the infrared and visible spectral regions.

The experiments performed disclose the real-time evolution of the optical properties while the system is suddenly brought out-of-equilibrium by an ultrashort laser pulse. The data obtained show how a competing admixture of two or more phases in a high-temperature superconductor can be created and observed evolving.

Finally by using new models for interpreting the experimental results the ultrafast dynamics of the competing phases start to be revealed.

*Alla mia famiglia, Carlo, Daniele, Cloe.*
*E ad Amalia.*

*Flectere si nequeo superos,*
*Acheronta movebo.*
Eneide (VII, 312)

# Contents

## CONTENTS

# List of Figures

## LIST OF FIGURES

## GLOSSARY

# Glossary

| | |
|---|---|
| **ARPES** | Angle-resolved photoemission spectroscopy |
| **BCS** | Bardeen-Cooper-Schrieffer theory of superconductivity |
| **Bi2212** | $Bi_2Sr_2CaCu_2O_{8+\delta}$ |
| **CDW** | Charge-density wave system |
| **CT** | Charge transfer |
| **CP** | Cooper pair |
| **$\Delta$R/R** | Relative variation of the reflectivity |
| **EDM** | Extended Drude model |
| **FWHM** | Full width at half maximum |
| **HFP** | High-frequency phonon |
| **HTSC** | High-temperature superconductor |
| **IR** | Infrared |
| **KK** | Kramers-Kroning relations |
| **MIR** | Mid-infrared |
| **NS** | Normal state |
| **OPA** | Optical parametric amplifier |
| **OD78** | Y-Bi2212 overdoped sample, $T_C$=78 K |
| **OD86** | Y-Bi2212 overdoped sample, $T_C$=86 K |
| **OP96** | Y-Bi2212 optimally sample, $T_C$=96 K |
| **UD83** | Y-Bi2212 underdoped sample $T_C$=83 K |
| **PCF** | Photonic crystal fiber |
| **PIPT** | Photoinduced phase transition |
| **PG** | Pseudogap |
| **QCP** | Quantum critical point |
| **QP** | Quasi-particles |
| **RT** | Rothwarf-Taylor model |
| **RTE** | Rothwarf-Taylor equations |
| **SC** | Superconducting |
| **SCS** | Superconducting $\Delta$R/R signal |
| **SDW** | Spin-density wave system |
| **SVD** | Singular value decomposition |
| **SW** | Spectral weight |
| **UV** | Ultraviolet |
| **YBCO** | $YBa_2Cu_3O_{7-\delta}$ |
| **Y-Bi2212** | $Bi_2Sr_2Ca_{1-x}Y_xCu_2O_{8+\delta}$ |
| **ZRS** | Zhang-Rice singlet |

## GLOSSARY

# Chapter 1

# Introduction

## 1.1 Overview

Understanding the phenomenon of superconductivity at high critical temperatures is one of the major challenge of contemporary physics. The reason being not only the complexity of the problem, often refereed as "the mystery that defies solution" (1), but also its potential applications (2, 3, 4). This fascinating phenomenon stimulated over one hundred thousands scientific publications since its discovery in 1986 (5), with a profound impact on both experimental and theoretical physics, urging scientists to develop and use the most advanced experimental techniques (6, 7, 8) and theoretical methods (9).

Besides the high critical temperature, an high-temperature superconductor (HTSC) exhibits many unconventional features when compared to conventional BCS superconductors (6, 7, 10, 11). For example HTSCs are characterized by strong electron-electron interactions with a rather complex and still unclear temperature-doping phase diagram. In this phase diagram, above the superconducting dome, a peculiar non-superconducting phase, called the pseduogap phase, with many unusual properties is present (12). This phase is believed to contain

important clues on the origin of high-temperature superconductivity (9, 13, 14, 15). Therefore, an understanding of the phase diagram is of prime importance for addressing the HTSCs problem.

Despite the effort so far done by the scientific community to tackle the problem, some fundamental questions remain open. For example, the relationship between the pseudogap states and superconductivity is not clear yet (16). On this matter in the literature there is significant disagreement. In particular there are two main claims, namely the mutual competition between the pseudogap phase and superconductivity (17, 18) or conversely their collaboration, with the pseudogap being a precursor of superconductivity (19, 20). Angle-resolved photoemission experiments (ARPES) at equilibrium has been the prime experimental technique used to measure the two distinct energy scales associated with the pseudogap and the superconducting gap respectively (21), however no conclusive answer has been reached so far.

Here I adopt a different approach to this problem by exploiting a novel experimental technique suitable for studying the HTSC out-of-equilibrium, i.e., when quasi-particles are photoexcited by an ultrashort laser pulse and the low-energy gaps are perturbed. At variance with conventional BCS superconductors, where this perturbation would produce no significant spectral weight rearrangements in the near-infrared and visible spectral regions (22), in HTSC superconductivity-induced spectral weight shifts are observed in these spectral regions (23, 24). The dynamical measurement of this spectral weight transfer is the main argument in this Ph.D. thesis.

Here the experimental novelty is the extension of standard pump-probe optical techniques in the time-energy space, with a broad spectral range, from 0.5 eV to 2.2 eV, with temporal resolution between 100 fs and 200 fs. The major achievement being the capability of disentangling signals originated by quasi-particles of different nature by the measurement of their dynamics and their optical spectral response.

To perform and correctly interpret this experiment the control of the non-equilibrium state induced by light is of fundamental importance. In facts, laser pulses produce many and diverse effects on the sample under study. This long-standing question started from the pioneering work of

Testardi (25) who shed light for the first time on the possibility of a non-thermal destruction of a conventional superconducting condensate with $\mu s$ laser pulses. Thus the issue on the stability of the superconducting state of HTSC under the action of photons is critical and must be disentangled by laser-induced heating (26, 27). Only recent all-optical pump-probe experiments on underdoped and optimally doped HTSC (28, 29, 30) have achieved control of the impulsive vaporization of the superconducting condensate in the high-intensity regime.

A similar photoinduced phase transition to the metallic phase has been recently reported on charge-density-wave (31, 32) and spin-density wave (33) compounds. While in such systems the photoinduced phase transition exhibits quasi-thermal character, as it is accompanied by the same critical slowing down observed in quasi-equilibrium conditions at $T_C$ (31, 32, 33), the origin of the photoinduced phase transition in HTSC remains unclear. In this work I demonstrate the non-thermal character of this photoinduced phase transition, developing some phenomenological models to describe this behavior.

Such a photoinduced phase transition can unlock the gate to understand the ultrafast dynamics of competing phases in real-time. In facts, under such non-equilibrium conditions, the homogeneous superconducting phase becomes unstable as its free energy increases during the light pulse duration (29, 34, 35), while the superconducting order parameter can dynamically coexist with pseudogap or normal state excitations. Here I show that the novel time-resolved optical spectroscopy is the experimental tool suitable to explore the real-time dynamics of competing phases present after the impulsive quench of the superconducting state. This technique is opening a new possibility to study the interplay between high-temperature superconductivity and the pseudogap phase.

## 1.2 Outline

The outline of this Ph.D. thesis is the following. The relevant models and previous experiments in the field are reviewed in chapter 2. This

section includes a brief overview of the problem of high-temperature superconductivity, the description of the optical properties of cuprates at equilibrium and a review of the main experimental results and models concerning the non-equilibrium properties of cuprates and BCS superconductors.

In chapter 3 the experimental methods and set-ups to perform the time-resolved spectroscopic experiment in the optical spectral region from 0.5 eV to 2.2 eV are described.

In the following chapter (chapter 4) all the results obtained at low excitations density through this novel technique are reported. The results are discussed within the framework of the extended-Drude analysis, adopting a differential model for the dielectric function able to describe the non-equilibrium response of each phase considered. A detailed analysis of quasi-particles decay time as a function of temperature and doping is then discussed in section 4.4. In particular the decay time divergence in the vicinity of the superconducting critical temperature is discussed within an analytical model based on the Rothwarf-Taylor equations.

The exploration of the high-fluence regime is introduced in chapter 5. Here the abrupt saturation of the superconducting time-resolved signal is studied on an overdoped single crystal, where the underlying normal phase is Fermi-liquid-like (9, 10). This allows a more transparent interpretation of the time-resolved traces, leading to the important conclusion that a photoinduced superconducting-to-normal phase transition occurs within few hundreds of femtoseconds and that the non-equilibrium superconducting gap, 1-2 ps after the pump pulse, is finite. To quantitatively interpret the data, an extension of the Rothwarf-Taylor model in the case of a time-dependent superconducting gap is proposed and applied. The final result is that within this model one can rule out a second-order quasi-thermal phase transition. The origin of the photoinduced phase transition is non-thermal and possibly of first-order character, as the the non-equilibrium superconducting gap after 2 ps remains finite above the threshold fluence.

This finding set the basis for the study of the real-time dynamics of an admixture of competing phases after an impulsive quench of the

superconducting phase, which is investigated in chapter 6 where I exploit the broad spectral range of the experimental technique developed in this thesis to disentangle pseudogap and superconducting phase signals. Here I obtain the superconducting phase reconstruction dynamics and I show that its rise time is limited by the relaxation of pseudogap quasi-particles.

# 1. INTRODUCTION

# Chapter 2

# State-of-the-Art

In this chapter, the experimental and theoretical results that set the state of the art relevant to my thesis are briefly reviewed.

## 2.1 Physical properties of HTSCs

Copper-oxide based high-temperature superconductors (HTSC) are a peculiar class of ceramic compounds with a perovskite-like layered structure, where a proper doping can produce superconductivity at temperatures much higher than any conventional ($T_C < 39$ K, in $MgB_2$ (36)) and unconventional superconductor ($T_C < 33$ K for organic compounds, in $RbCs_2C_{60}$, $T_C < 10$ K for heavy fermion materials). Before the recent discovery of high temperature superconductivity in Fe-based pnictides (37), HTSCs were believed to belong only to the family of copper oxides (cuprates). Still it is an hole-doped cuprate which exhibit the highest critical temperature ($T_C = 135$ K in $HgBa_2Ca_2Cu_3O_{10+x}$). In this thesis I mostly focus my attention on a cuprate compound, namely the Y-substituted Bi2212 compound ($Bi_2Sr_2Ca_{0.92}Y_{0.08}Cu_2O_{8+\delta}$). This compound have a slightly higher attainable $T_C$ ($\sim$ 96

K) due to chemical substitution (38), but have similar electronic properties to the well-known Bi2212 ($Bi_2Sr_2CaCu_2O_{8+\delta}$).

### 2.1.1 Electronic structure

All the cuprates share the same layered structure constituted by one or more Cu-O planes and a *charge reservoir layer* made of several oxide planes involving different elements depending on the compound.

In Fig. 2.1 I show the crystalline structure of a Bi2212 compound. A set of oxide planes can be recognized in the crystalline structure and in particular a stack made of two Cu-O planes is present in this compound. The electronic properties of cuprates are mostly determined by the Cu-O planes and are highly anisotropic when $c$-axis and $ab$-axis properties are compared.

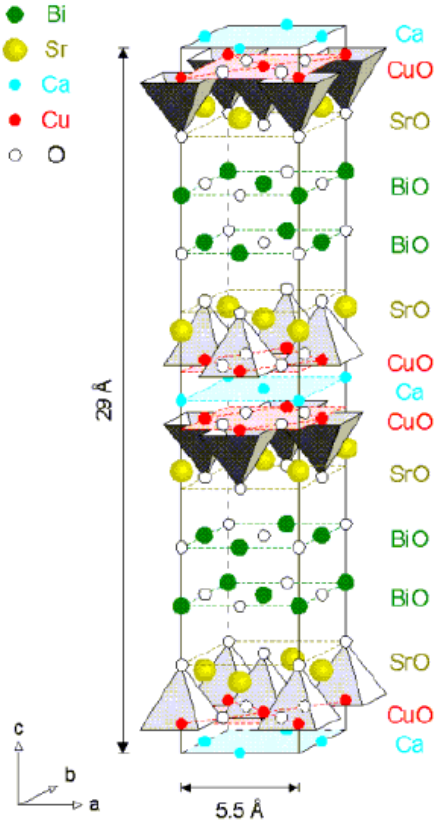


**Figure 2.1: Bi2212 crystal structure** - Crystal structure of Bi2212. Image from (39)

In the following I focus on the electronic structure of a single Cu-O plane in the parent compound, i.e., when the oxygen doping is zero. The $Cu^{2+}$ ions are in the electronic configuration $3d^9$ and the $O^{2-}$ has electronic configuration $2p^6$. The copper atom is surrounded by the four oxygens in the Cu-O plane and the apical oxygens forming an octahedral environment (see Fig. 2.1). The distortion from a perfect octahedron due to the shift of the apical oxygens splits the $e_g$ orbitals so that the highest partially occupied $d$ orbital is of the type $x^2 - y^2$. The lobes of this Cu orbital point directly to the $2p$ orbital of the neighboring oxygen, forming a strong covalent bond with a

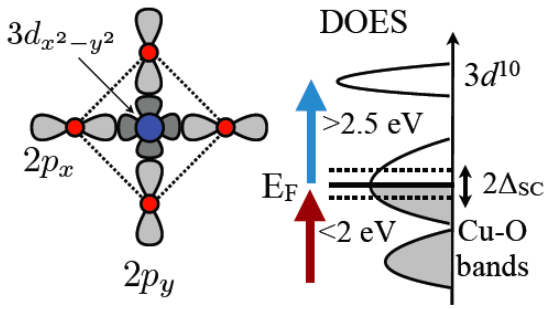


**Figure 2.2: Cu and O electronic orbitals and DOS** - a) Electronic orbitals responsible for the covalent bonding between Cu and O atoms in the Cu-O planes. b) Density of states for Cu and O bands.

large hopping integral $t_{pd}$ (see Fig.2.2). Thus the electronic state of the cuprates can be described by the so-called three-band model, where in each unit cell we have the Cu $d_{x^2-y^2}$ orbital and two oxygen $p$ orbitals (40, 41).

The Cu orbital $d_{x^2-y^2}$ is singly occupied while the $p_x$ and $p_y$ orbitals are doubly occupied, with all these orbitals being admixed by $t_{pd}$ and by ibridization with other oxygen orbitals. In the hole picture, the Cu $d^9$ configuration is represented by an energy $E_d$ and it is occupied by a single hole with $S = \frac{1}{2}$, while the oxygen $p$ orbitals are empty of holes and lie at an energy $E_p > E_d$. Due to the high Coulomb on-site repulsion, $U_d$, the energy of the doubly occupied Cu orbital $d^8$ is much higher than both $E_d$ and $E_p$, thus identifying the parent compound of HTSC as a *charge-transfer insulator* in the classification of strongly correlated systems (42).

In analogy to the case of the one-band Mott-Hubbard insulator, the virtual hopping to doubly occupied $d^8$ states leads to a gain in kinetic energy for anti-ferromagnetically ordered holes in the Cu sites (see sketch of Fig. 2.3). The exchange integral of the anti-ferromagnetic interaction is given by

$$J = \frac{t_{pd}^4}{(E_p - E_d)^3} \tag{2.1}$$

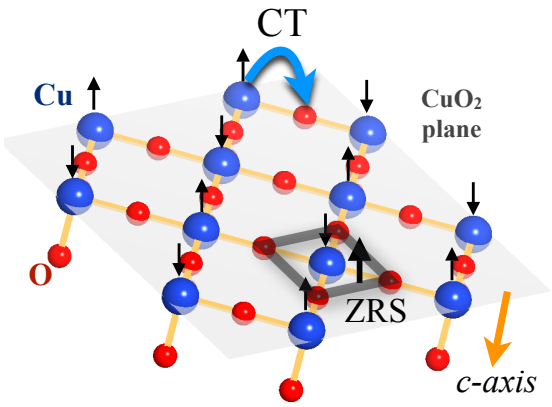


**Figure 2.3: Cu-O plane structure** - Atomic structure of the Cu-O plane with a representation of the Zhang-Rice singlet (ZRS) and of the in-plane charge-transfer process between Cu and O atoms. Cu atoms are sketched in blue, while Oxygen atoms in red, the arrows indicate the direction of spin the anti-ferromagnetic phase

which results in a relatively high value for cuprates ($J \sim 0.13\ eV$ (9)) causing a robust anti-ferromagnetic phase at zero doping. Moreover, a lower energy state is obtained considering a fully symmetric linear combination of oxygen hole states around the Cu site with the Cu hole spin that couples anti-ferromagnetically to the O hole spins. This singlet state, known as Zhang-Rice singlet (ZRS, see the sketch in Fig.2.3), can hop from site to site like a single hole does in a simple single-band Hubbard model (43).

In theory it is possible to recover the single-band Hubbard model only in the case of a single hole added to the undoped compound. When additional holes are present in the Cu-O planes the single-band approximation is not valid anymore because the interactions between neighboring Zhang-Rice singlets must be considered.

For hole-doped samples the anti-ferromagnetic phase is strongly suppressed. By further hole-doping the superconducting phase is achieved, as it will be discussed in more details in section 2.1.2. Thus the role of

hole-doping in the Cu-O planes is critical for the physical properties of cuprates.

Although spin-resolved photoemission measurements (44) and theoretical calculation using Dynamical Mean Field Theory (DMFT) recently confirmed that the lowest energy excitations have a singlet nature providing a direct support to the stability of the Zhang-Rice singlet in hole-doped cuprates, the question whether the single-band Hubbard model can satisfactorily describe the physics of HTSC is still an open problem. Despite its apparent simplicity the Hubbard model is very difficult to apply. In this light one of most studied simplified Hamiltonians is called t − J model and it is obtained from the Hubbard model by treating the hopping term as a perturbation:

$$H = -t \sum_{\langle i,j \rangle} (c^{+}_{i,\sigma} c_{j,\sigma} + H.c.) + J \sum_{\langle i,j \rangle} (S_i \cdot S_j - \frac{1}{4} n_i n_j) \tag{2.2}$$

The t − J Hamiltonian is widely used as a starting point to describe the electronic properties of HTSC. However there are several indications that a purely electronic mechanism is not sufficient to explain the pairing of the electrons in cuprates (9). For this reason, many efforts have been devoted to study the electron-phonon interaction effects in the t − J model (45).

To summarize, a very simple sketch of the density of states for a cuprates after the introduction of holes in Cu-O planes is shown in Fig. 2.2b. This scheme will be useful to recognize the origin of the optical transition. The Fermi level lies in the ibridized Cu-O band, which have a bandwidth of about 1.5 eV. Just below the conduction band , within 2 eV below $E_F$, some other completely filled bands are present, which are again Cu-O ibridized bands, and can be recognized in the broad mid-IR absorption peaks appearing in the optical spectra of strongly underdoped Bi2212 samples (11). On the side of empty bands, at least 2.5 eV above the Fermi level there is the upper Hubbard Cu band, corresponding to the $d^{10}$ electronic configuration on the Cu atom.

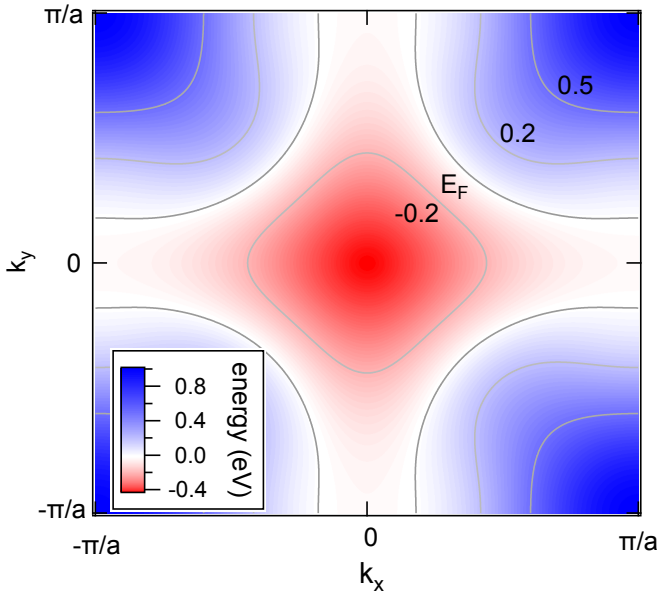


**Figure 2.4: Energy band dispersion for Bi2212** - Energy band dispersion in First Brillouin Zone for Bi2212 calculated from the Tight-binding parametrization proposed by Norman (46) to fit the ARPES data, see table 2.1. The used values are the one referred to the normal state.

A more detailed description of the conduction band structure and of the Fermi surface can be obtained through the tight-binding parametrization proposed by Norman (46). This parametrization was obtained by fitting ARPES experimental data for Bi2212 with a basis set of tight-binding functions. The large amount of ARPES data collected on these samples allows a thorough verification of the correctness of this parameterization. The relevant functions and coefficients are shown in table 2.1 while the numerical results obtained from this calculation is shown in Fig. 2.4.

With this calculation the shape of the Fermi surface can be obtained, together with a precise determination of the density of states in the vicinity of the Fermi level. The Fermi surface of cuprates is highly unstable and mainly two distinct low-energy gaps have been recognized in the low-energy excitation spectrum by ARPES (21, 47, 48, 49). A superconducting gap appears below $T_C$, while a pseudo-gap, whose ori-

| $\eta_i(\vec{k})$ | **coefficient** |
|---|---|
| 1 | 0.1305 |
| $\frac{1}{2}(cos(k_x)+cos(k_y))$ | -0.5951 |
| $(cos(k_x)cos(k_y)$ | 0.1636 |
| $\frac{1}{2}(cos(2k_x)+cos(2k_y))$ | 0.0519 |
| $\frac{1}{2}(cos(2k_x)cos(k_y)+cos(k_x)cos(2k_y))$ | -0.1117 |
| $(cos(2k_x)cos(2k_y)$ | 0.0510 |

**Table 2.1: Tight-binding parametrization of Bi2212 band dispersion** - Tight-binding parametrization of Bi2212 band dispersion obtained from (46)

gin is still under debate (15, 16, 50), is observed below a temperature T*(12).

These gaps have distinct k-space dependence (48, 49) and are characterized by different energy scales (21). In particular it has been shown that the superconducting gap has a node in the ($\pi$,$\pi$) direction (51) (see Fig.2.4) and its k-space dependence in the vicinity of the nodal point follows the one predicted for a *d-wave* gap. At the anti-node ((0,$\pi$) direction), i.e., where the superconducting gap is maximum, the situation is more complex as the pseudogap is also present in the low-energy spectrum. In facts, while the pseudogap it is strongly suppressed in the nodal region it dominates at the anti-node (48, 49, 52).

### 2.1.2 Phase diagram

The critical parameter that determines the properties of cuprates is the amount of holes in the Cu-O planes. In the case of $Bi_2Sr_2CaCu_2O_{8+x}$ samples this amount can be controlled by tuning the oxygen content $x$. The resulting phase diagram in the temperature-doping plane of hole-doped cuprates is schematically shown in Fig. 2.5.

The anti-ferromagnetic phase at zero doping have a Neel temperature, $T_N$, of about 300-400 K and it is rapidly quenched by hole doping, completely disappearing at a doping $x < 0.05$. At increasing doping the phase diagram is characterized by a superconducting phase (SC)

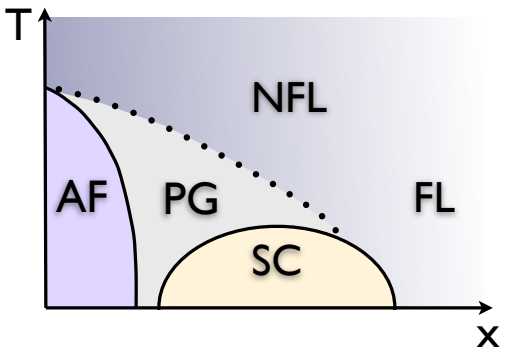


**Figure 2.5: Scheme of the universal phase diagram of hole-doped cuprates** - In this scheme SC denote the superconducting state, AF the anti-ferromagnetic phase, PG the pseudogap phase and NFL and FL the normal state with Non-Fermi liquid and Fermi-liquid properties respectively. The solid lines represent critical temperatures of a phase boundary ($T_N$ for AF and $T_C$ for SC), while dashed lines are used for crossover lines (T* for PG). The crossover between FL and NFL is not shown as experimental data are not enough to draw these crossover line. Similar schematization of the phase diagram can be found in (7, 9, 10)

that reaches the maximum $T_C$ at the so called optimal doping, $x_{opt}$. The side of the phase diagram at lower dopings is called *underdoped* side, while the one above $x_{opt}$ is called the *overdoped* side.

The *underdoped* side is characterized by the enigmatic pseudogap (PG) phase. In this phase a pseudogap (as described in previous section) is present in the low-energy excitation spectrum. This region of the phase diagram presents many unusual properties not encountered before in any other metal (9). Recent evidences on the magnetic ordering below T* (53) favor its interpretation as a well-defined phase in the phase diagram, even if a definite finite-temperature phase boundary has not been found so far. The line drawn in Fig. 2.5 should be regarded as a tentative phase separation and several ways of drawing the phase diagram exist (21).

The key issue on the relationship between the pseudo-gap and the superconductive state is the subject of an intense debate (15, 16, 54).

This is a pivotal question on the entire problem of high-Tc superconductivity and remains without an answer, the main perspectives being:

- pseudogap as *precursor* of superconductivity, where pairing is present below T*, but lacks of long-range order and coherence. Condensation of Cooper pairs takes place below $T_C$.
- a *competitive* picture, where PG and SC phases represent competing orders.

Experimental evidences of both CP *pre-formation* (19, 20) and PG-SC *competition* (17, 18) are present in the literature. Thus the question on their mutual relationship is open and a possible picture reconciling the two different set of evidences have to be found, also suggested by recent ARPES measurements where both behavior are observed (52).

The region of the normal state above $x_{opt}$ also exhibits unusual properties. The resistivity is linear in T (10) and the Hall coefficient is temperature dependent (55). These and others properties are manifestation of non-Fermi-liquid behavior of this region of the phase diagram, sometimes called *strange metal region*. Beyond the optimal doping the normal state gradually become a Fermi-liquid, as demonstrated by the conventional $T^2$ resistivity (10). The crossover between the two regions is very faint and no separation line has been drawn in Fig. 2.5.

## 2.2 Equilibrium optical properties of cuprates

A very powerful and widely used technique to investigate the electronic properties of solids is optical spectroscopy. This technique measures the optical properties, such as the reflectivity $R$ and the transmittivity $T$, in a wide spectral range. These experimentally accessible quantities are univocally determined by the optical constants of the material, i.e., the dynamical complex conductivity, $\sigma(\omega)$, or equivalently the complex dielectric function $\epsilon(\omega)$.

Optical spectroscopy can be used to extract information on these functions and consequently on the electromagnetic linear response of

the system. When the experiment is performed at different polarization of the incident light or a different angles of incidence the technique is called ellipsometric and it provides a direct measurement of the dielectric function, $\epsilon(\omega)$, at each wavelength.

The dynamical conductivity of solids is characterized by several electronic transitions, being them direct and phonon-assisted, interband and intraband transitions. A very useful model to describe the optical conductivity, $\sigma(\omega)$, and consequently $R(\omega)$ and $T(\omega)$, is the Drude-Lorentz model, where the fundamental hypothesis is that electrons in the conduction band constitute a classical gas of non-interacting particles. Within this model, the optical conductivity $\sigma(\omega)$ is given by:

$$\sigma(\omega) = \frac{1}{4\pi} \frac{\omega_{p,D}^2}{1/\tau_D - i\omega\tau_D} + \frac{1}{4\pi} \sum_j \frac{\omega_{p,j}^2 \omega}{\omega/\tau_j + i(\omega_j^2 - \omega^2)} \tag{2.3}$$

where the first term (Drude term) is related to the intraband optical transitions and describes the motion of the free carriers, $\omega_{p,D}^2$ being the Drude plasma frequency and $1/\tau_D$ the free carriers scattering rate. The second term describes the interband optical transitions in term of a sum of optical oscillators with characteristic plasma frequencies $\omega_{p,j}$, resonance frequencies $\omega_j$ and relaxation times $\tau_j$.

The model outlined above describes very well the optical properties of a good metal, while it fails to account for strong electron-bosons interactions in the intraband term of the optical properties of poor metals, and for example of cuprates. To generalize this framework to this case of special interest for this thesis we present in the following sections the Extended Drude model, section 2.2.1, and its application to the optical properties of cuprates, section 2.2.2.

### 2.2.1 Extended Drude model

The generalization of the Drude model to the case of boson-assisted optical transitions is called Extended Drude model (EDM) (56, 57). This model has been used for the first time by Allen to analyze the

far infrared optical response of the metals at T=0 and later on it was generalized to the case of finite temperature (58). In the following years the EDM has been extensively applied to strongly correlated materials like HTSC. In the EDM all the effects of the strong interactions are accounted for by an optical self-energy $\Sigma_{opt}(\omega)$ and the corresponding expression of the complex conductivity is:

$$\sigma(\omega) = \frac{i\omega_p}{\omega + \Sigma_{opt}(\omega)} \tag{2.4}$$

where the optical self-energy $\Sigma_{opt}(\omega)$ has the same analytical properties of the self-energy $\Sigma(\omega, \vec{k})$ with the important difference of being a k-space integrated quantity, namely, along the Fermi surface. The optical self energy can be also written as

$$\Sigma_{opt}(\omega) = \Sigma'_{opt}(\omega) + \Sigma''_{opt}(\omega) = \omega \left( \frac{m*(\omega)}{m} - 1 \right) + i\frac{1}{\tau(\omega)} \tag{2.5}$$

where the imaginary part is a frequency dependent scattering rate due to the electron-phonon scattering, while the real part cause an effective mass renormalization, in practice a mass enhancement due to the correlations and boson scattering. Thus the main difference in respect to the Drude model is that the single Lorentzian peak centered at zero frequency is substituted by an infinite set of Lorentzian peaks each one describing $\sigma\omega$ in the vicinity of a particular frequency $\omega$ with parameters $\frac{1}{\tau(\omega)}$ and $m^*(\omega)$.

A less transparent but more useful definition of the optical conductivity can be obtained starting from the single particle self-energy and by omitting vertex correction (Migdal approximation):

$$\sigma(\omega) = \frac{\omega_p^2}{i4\pi\omega} \int_{-\infty}^{+\infty} \frac{f(\omega+\epsilon, T) - f(\omega, T)}{\omega - \Sigma^*(\omega+\epsilon, T) + \Sigma(\omega, T) + i\Gamma_{imp}} d\epsilon \tag{2.6}$$

where $\omega_p$ is the plasma frequency, $f$ is the Fermi-Dirac distribution function and $\Gamma_{imp}$ is the scattering rate term due to impurities. $\Sigma(\omega, T)$

is given by a convolution integral between the Eliashberg boson spectral function $\alpha^2F(\Omega)$ (refs) and a Kernel function $L(\omega, \Omega, T)$ describing the thermal dependence of the phononic excitations coupled to electrons,

$$\Sigma(\omega, T) = \int_0^\infty \alpha^2 F(\Omega) L(\omega, \Omega, T) \tag{2.7}$$

where the Kernel function is an integral containing the Bose-Einstein distributions of phonons, $n(\Omega)$, and the Fermi-Dirac distribution of electrons, $f(\omega)$ and can be solved analytically obtaining the expression

$$L(\omega, \Omega, T) = -2\pi i \left[ n(\Omega) + \frac{1}{2} \right] + \Psi\left( \frac{1}{2} + i\frac{\Omega - \Omega'}{2\pi T} \right) - \Psi\left( \frac{1}{2} - i\frac{\Omega + \Omega'}{2\pi T} \right) \tag{2.8}$$

This formalism can be generalized to the case of complex systems, such as cuprates, where strong interactions with several kind of bosons are present, such as magnetic and other electronic excitations. In this case a general "glue function" is defined as a sum of several bosonic spectral functions,

$$\Pi(\Omega) = \alpha^2 F(\Omega) + I^2\chi(\Omega) + ... \tag{2.9}$$

where for example $I^2\chi(\Omega)$ account for the interaction between electrons and spin-fluctuations. This generalized formalism has been successfully applied to interpret the optical spectra of cuprates (59) and it will be used in the next section to analyze the optical properties of optimally doped Bi2212.

### 2.2.2 Reflectivity of optimally doped Bi2212

In Fig. 2.6 the reflectivity measured on the sample OP96 (see Chap. 3) by spectroscopic ellipsometry at 300 K and 100 K is shown. The reflectivity measured at 20 K is not reported, since, on the scale of Fig. 2.6, it overlaps with the 100 K results. In the top inset to Fig. 2.6 the real ($\epsilon_1$) and imaginary ($\epsilon_1$) parts of the dielectric function, measured for OP96 at 100 K, are reported. From these data we can argue that,

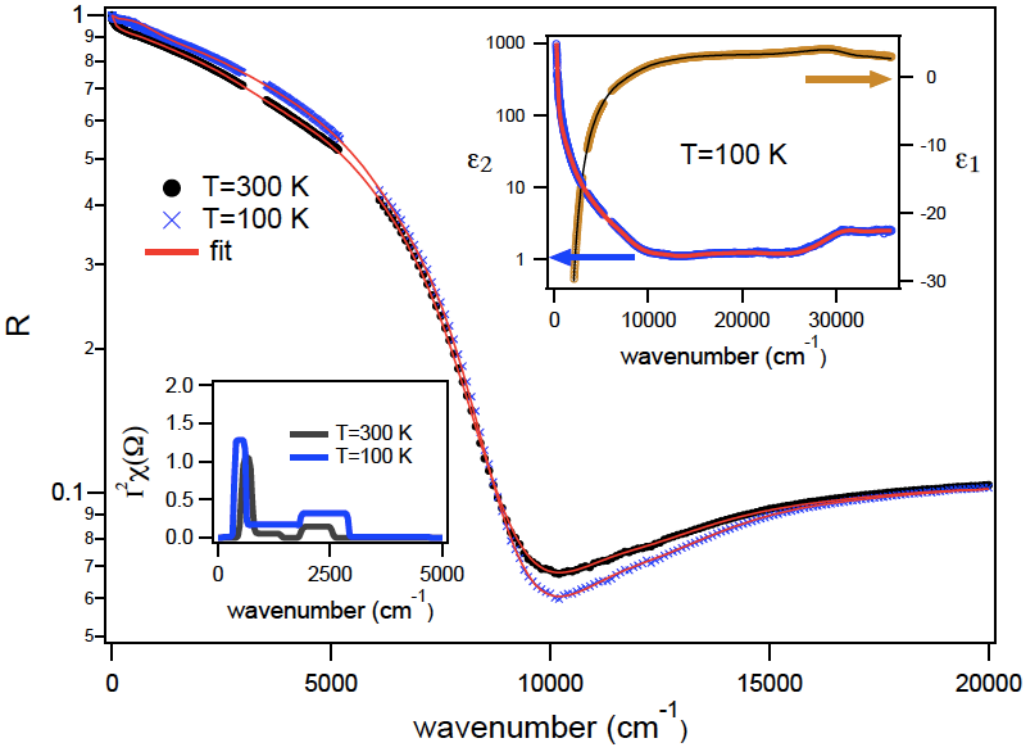


**Figure 2.6: Reflectivity, OP96 sample** - Static reflectivity data for optimally doped $Bi_2Sr_2Ca_{0.92}Y_{0.08}Cu_2O_{8+\delta}$, $T_C$=96 K. The shown data are taken at T=300 K and T=100 K respectively and the fit obtained through the EDM and the glue function formalism (see section 2.2.1). In the left inset the fitted glue functions at the two temperatures are shown, while in the upper right inset the dielectric function and the corresponding fit are shown

below 10000 $cm^{-1}$ (1.25 eV), $\epsilon(\omega)$ is dominated by the Drude response of free carriers coupled to a broad spectrum of bosons (59), whereas in the high-energy region ($\hbar\omega$ >1.25 eV), a major role is played by the interband transitions. The best fit to the data (solid black lines) is obtained modeling the equilibrium dielectric function with the EDM as discussed in section 2.2.1 and consequently calculating the reflectivity through the formula:

**Table 2.2: Dielectric function parameters of optimally Bi2212-**
Parameters for the static dielectric function for the sample OP96

| | parameters | T=20 K | T=100 K | T=300 K |
|---|---|---|---|---|
| | $\epsilon_\infty$ | 2.67 | 2.67 | 2.62 |
| extended Drude | $\omega_p\,(cm^{-1})$ | 17418 | 17392 | 16901 |
| | $\Gamma_{imp}\,(cm^{-1})$ | 53 | 155 | 625 |
| | $\omega_0\,(cm^{-1})$ | 4234 | 4929 | 4264 |
| | $\omega_{p0}^2\,(cm^{-2})$ | 10454991 | 13871222 | 22041800 |
| mid-infrared | $\gamma_0\,(cm^{-1})$ | 3535 | 4706 | 4069 |
| peaks | $\omega_1\,(cm^{-1})$ | 6490 | 6959 | 6789 |
| | $\omega_{p1}^2\,(cm^{-2})$ | 11001998 | 6489852 | 8142014 |
| | $\gamma_1\,(cm^{-1})$ | 3519 | 2949 | 3925 |
| | $\omega_2\,(cm^{-1})$ | 11800 | 11800 | 11650 |
| | $\omega_{p2}^2\,(cm^{-2})$ | 5560610 | 7460610 | 5307060 |
| | $\gamma_2\,(cm^{-1})$ | 3644 | 3944 | 3500 |
| | $\omega_3\,(cm^{-1})$ | 16163 | 16163 | 15409 |
| | $\omega_{p3}^2\,(cm^{-2})$ | 40768500 | 41268500 | 45542000 |
| | $\gamma_3\,(cm^{-1})$ | 8304 | 8304 | 8905 |
| | $\omega_4\,(cm^{-1})$ | 21947 | 21947 | 21300 |
| interband | $\omega_{p3}^2\,(cm^{-2})$ | 225776000 | 230776025 | 223159025 |
| transitions | $\gamma_4\,(cm^{-1})$ | 13998 | 13898 | 13898 |
| | $\omega_5\,(cm^{-1})$ | 31057 | 31057 | 30756 |
| | $\omega_{p5}^2\,(cm^{-2})$ | 288626121 | 288626121 | 320536896 |
| | $\gamma_5\,(cm^{-1})$ | 6191 | 6191 | 6908 |
| | $\omega_6\,(cm^{-1})$ | 35146 | 35146 | 34946 |
| | $\omega_{p6}^2\,(cm^{-2})$ | 217474009 | 217474009 | 214474009 |
| | $\gamma_6\,(cm^{-1})$ | 6396 | 6396 | 6396 |
| | $\omega_7\,(cm^{-1})$ | 40421 | 40421 | 40421 |
| | $\omega_{p7}^2\,(cm^{-2})$ | 750212100 | 750212100 | 756371984 |
| | $\gamma_7\,(cm^{-1})$ | 7518 | 7518 | 7518 |

$$R(T,\omega) = \left| \frac{1-\sqrt{\epsilon(T,\omega)}}{1+\sqrt{\epsilon(T,\omega)}} \right|^2 \tag{2.10}$$

The bosonic spectral function $I^2\chi(\Omega)$ is usually characterized by a narrow peak at 60-70 meV and a broad spectrum extending up to 400 meV (59). In the bottom inset to Fig. 2.6 we report the boson spectra extracted from the fit at T=300 K and T=100 K. Below $T_C$ the far-infrared reflectivity is dominated by the opening of the superconducting gap and by the emergence of the condensate $\delta(0)$ function. For this reason, the extraction of the boson spectral function below $T_C$ is difficult and is still subject of debate (59). To fit the reflectivity at T=20 K we used the $I^2\chi(\Omega)$ determined at T=100 K. In Fig. 2.6, the solid lines are the fit to the data. In Table 2.2 we report all the parameters obtained from the fitting procedure on OP96, at T=300 K, T=100 K and T=20 K.

The optical properties are satisfactorily reproduced over the whole spectrum, considering, in addition to the extended Drude model, two mid-infrared (MIR) peaks in the intraband region ($\hbar\omega$ ~0.5,0.8 eV). The interband transitions in the near-IR/visible/UV spectral range are reproduced using six Lorentz oscillators at $\hbar\omega_{0i}$ =1.46, 2, 2.72, 3.85, 4.4 and 5 eV. The number of the interband oscillators has been fixed to the minimum necessary to obtain a stable fit. Adding more oscillators does not significantly improve the $\chi^2$ of the fit in the 1-5 eV region. The detail of the fit components is shown in the 0.5-4 eV spectral region at 20 K in Fig. 2.7.

The attribution of the interband transitions in cuprates is a subject of intense debate. As a general phenomenological trend, the charge-transfer (CT) gap edge (hole from the upper Hubbard band with $d_{x^2-y^2}$ symmetry to the O-$2p_{xy}$ orbitals) in the undoped compounds is about 2 eV (11). Upon doping, a structure reminiscent of the CT gap moves to higher energies, while the gap is filled with states at the expenses of spectral weight at $\hbar\omega > 2$ eV (11). Dynamical mean field calculations of the electron spectral function and of the *ab*-plane optical conductivity for the hole-doped three-band Hubbard model recently found that

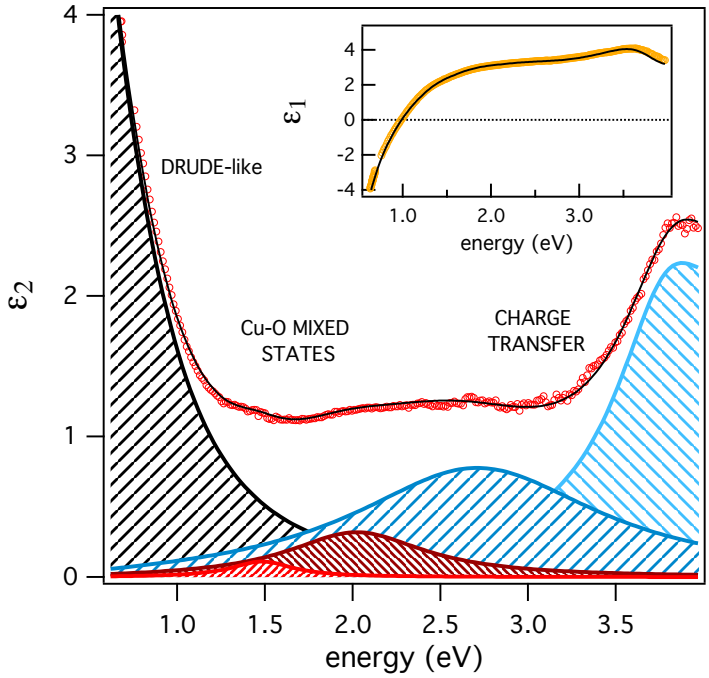


**Figure 2.7: Optical properties, OP96 sample, at 20 K** - Dielectric function of sample OP96 at 20 K and the fit obtained within the EDM (see text). The different components of the fit, i.e., the Drude term and the Lorentz oscillators at energies $\hbar\omega_{0i}$ =1.46, 2, 2.72 and 3.85 eV are shown separately.

the Fermi level moves into a broad (∼2 eV) and structured band of mixed Cu-O character, corresponding to the Zhang-Rice singlet states (60). The empty upper Hubbard band, which involves Cu-3$d^{10}$ states, is shifted to higher energies with respect to the undoped compound, accounting for the blue-shift of the optical CT edge to 2.5-3 eV. The structures appearing in the optical conductivity at 1-2 eV, i.e., below the remnant of the CT gap, are mostly related to transitions between many-body Cu-O states at binding energies as high as 2 eV (e.g. such as singlet states) and states at the Fermi energy.

The dielectric functions of UD83 and OD86 have been extrapolated from the $\epsilon_{eq}(T,\omega)$ of OP96, following the trend of the optical properties

at different dopings, reported in Ref. (61). In particular, for UD83, the main modification to the dielectric function are: i) $\epsilon_\infty = 2.55$; ii) the plasma frequencies of the Drude ($\omega_p$) and MIR peaks ($\omega_0$ and $\omega_1$) are decreased by $\sim 3.7\%$; iii) the plasma frequencies $\omega_2$ and $\omega_3$ are decreased by $\sim 3.7\%$; iv) the plasma frequency $\omega_4$ is decreased by $\sim 13\%$; v) the plasma frequency $\omega_5$ is increased by $\sim 30\%$; vi) the plasma frequencies $\omega_6$ and $\omega_7$ are decreased by $\sim 4.8\%$. For OD86, the main modification to the dielectric function are: i) $\epsilon_\infty = 2.79$; ii) the plasma frequencies of the Drude ($\omega_p$) and MIR peaks ($\omega_0$ and $\omega_1$) are increased by $\sim 2.9\%$; iii) the plasma frequencies $\omega_2$ and $\omega_0$ are increased by $\sim 2.9\%$; iv) the plasma frequency $\omega_4$ is increased by $\sim 14\%$; v) the plasma frequency $\omega_5$ is decreased by $\sim 17\%$; vi) the plasma frequencies $\omega_6$ and $\omega_7$ are increased by $\sim 3.7\%$.

## 2.3 Non-equilibrium properties of superconductors

The experimental investigation of the non-equilibrium properties of superconductors is a very active field since the 60', when first experiments on the quasi-particles (QPs) lifetime in a BCS superconductor were performed with tunneling junction experiments (62, 63) These experiments showed a serious discrepancy (of several order of magnitude) between the expected QPs lifetime and the measured one. This discrepancy lead to the formulation of the Rothwarf-Taylor model (64) which has been largely used by the scientific community, until nowadays (65) when surprisingly the model has been shown to be useful to describe also the ultrafast dynamics measured on cuprates through time-resolved optical pump-probe experiments. This model is reviewed in section 2.3.1.

In the early 70' the pioneering experimental work of Testardi (25) showed the possibility of non-thermally quench the superconducting state in Pb films on the nanoseconds timescale with a light pulse. This work fueled a series of theoretical works on the effect of light pulses on superconducting condensates. The amount of literature on the field is vast (34, 66, 67, 68, 69), however there are two simple and prototypical

models, namely the T* (68) and the $\mu$* (34), which are the good starting point for an analysis of non-equilibrium effects on superconductors. These models are reviewed in section 2.3.2.

Pump-probe optical experiments on HTSC with sub-ps time resolution started in the early '90. A review of the common features evidenced by the large amount of data collected is proposed in section 2.3.3, together with some specific models that have been discussed in the literature, such as the two-temperature and the three-temperature models.

### 2.3.1 Quasi-particles dynamics: the Rothwarf-Taylor model

A very useful model to interpret the non-equilibrium dynamics of superconductors, in the case of a small perturbation of the excitation densities, is the Rothwarf-Taylor (RT) model (64, 65, 70). In this model, two QPs recombine to form a Cooper pair emitting a boson with energy larger then $2\Delta$, where $\Delta$ is the superconducting gap. As the reverse process is also allowed, the QP and the boson populations are in quasi-equilibrium and the actual relaxation is determined by inelastic processes. This phenomenological model have been successfully used to interpreted the non-equilibrium dynamics of both conventional (64, 70) and unconventional superconductors (65, 71) and it is based on the Rothwarf-Taylor equations (64),

$$\dot{n} = I_{QP}(t) + 2\eta N - \beta n^2 \tag{2.11}$$

$$\dot{N} = I_{ph}(t) - \eta N + \beta n^2/2 - \gamma_{esc}(N - N_T) \tag{2.12}$$

describing the density of excitations $n$ coupled to phonons, $N$ being the gap-energy phonon density. The non-equilibrium QP and phonons are photo-injected in the system through the $I_{QP}(t)$ and $I_{ph}(t)$ terms. $I_{QP}(t)$ and $I_{ph}(t)$ are the source terms and in the case of a laser pulse a gaussian temporal profile with full-width at half-maximum equal to the pump pulse duration is assumed. The coupling of the electronic and phonon population is obtained through a) the annihilation of a

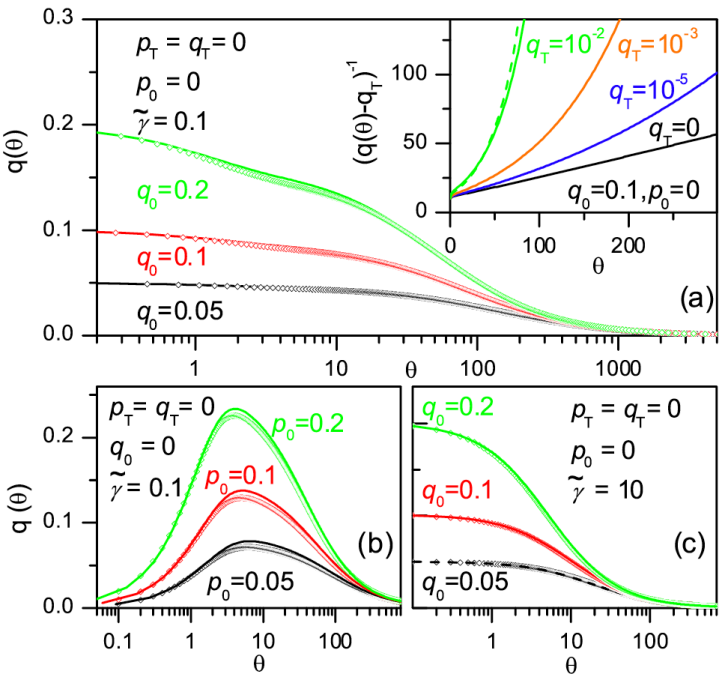


**Figure 2.8: Analytical and numerical solutions of the Rothwarf-Taylor equations** - Analytical and numerical solutions of the Rothwarf-Taylor equations in their a-dimensional formulation (65). The graph have been taken form (65)

Cooper pair via gap phonon absorption ($N\eta$ term) and b) the emission of gap phonons during the two-body direct recombination of excitations to form a Cooper pair ($\beta n^2$ term). In the phonon bottleneck regime ($\eta > \gamma_{esc}$) the excitation relaxation is ultimately regulated by the escape rate of the non-equilibrium gap-energy phonons ($\gamma_{esc}(N - N_T)$ term, $N_T$ being the thermal phonon density). The $\gamma_{esc}$ value is determined both by the escape rate of the non-equilibrium phonons from the probed region and by the energy relaxation through inelastic scattering with the thermal phonons. The $\Delta R/R$ superconducting signal (SCS) is assumed to be proportional to the solution $n(t)$ of (2.11), in agreement with previous works (27, 28, 29, 30, 65, 71, 72, 73, 74, 75, 76, 77, 78).

Only recently (65) an analytic solution of the RTE has been found in some important limiting cases, namely the weak and the strong bot-

tleneck regimes (64, 65). The analytic solutions are better expressed in terms of an a-dimensional formulation of the RTE,

$$dq/d\theta = p - q^2 \tag{2.13}$$

$$dp/d\theta = -p/2 + q^2/2 - \tilde{\gamma}(p - p_T) \tag{2.14}$$

where $q = \beta n/\gamma$ and $p = \beta N/\gamma$ are the dimensionless excitation densities, $\theta = \gamma t$ and $\tilde{\gamma} = \gamma_{esc}/\gamma$ are the dimensionless time and high-frequency phonons decay rate.

Within this notation the weak bottleneck regime correspond to the case $\tilde{\gamma} >> 1$, while $\tilde{\gamma} << 1$ is the strong bottleneck regime. The analytic solution of the RTE for these two regimes and for various initial conditions is shown in Fig. 2.8 (taken form (65)), together with the corresponding numerical solution. Two important observations arising from these results are: i) the decay dynamics at low temperatures is equivalent to a simple bi-molecular dynamics ii) if the initially photoexcited number density is dominated by quasi-particles the rise time dynamics coincide with the source term, while if it is dominated by high-frequency phonons $q(t)$ have a maximum at a delayed time.

The decay dynamics is reproduced by a set of exponential decays, with decay rate temperature and excitation intensity dependent. The dependence of the decay rate in the strong bottleneck regime can be expressed through the relation (65),

$$\gamma\left(T, q_0, p_0\right) = 2\left[q_s\left(q_0, p_0\right) + q_T\left(T\right)\right]\tilde{\gamma}\left(T\right) \tag{2.15}$$

with $q_s$ is the quasi-stationary quasi-particle density, reached at quasi-equilibrium between QPs and HFPs, and $q_T$ is the quasi-particle density at thermal equilibrium. In the weak bottleneck regime the relation becomes (65),

$$\gamma(T, q_0) = 2(q_0 + q_T(T)) \tag{2.16}$$

where we notice that the dependence from $p_0$ and $\tilde{\gamma}$, i.e., the quantities related to the phonon subsystem, has disappeared in the weak bottleneck regime.

### 2.3.2 Non-equilibrium superconductivity: T* and $\mu$* models

In the BCS theory the dependence of the superconducting gap on the excitation distribution function is obtained through the gap equation:

$$1 = N(0)U_{pair}\int_0^{\hbar\omega_D}\frac{d\epsilon_k}{\sqrt{\epsilon_k^2+\Delta^2}}tanh\left(\frac{\sqrt{\epsilon_k^2+\Delta^2}}{2k_BT}\right) \tag{2.17}$$

where $N(0)$ is the electronic density of states at the Fermi level, $\Delta$ is the superconducting gap and $U_{pair}$ is the attractive pairing potential. In non-equilibrium superconductivity, an excess of excitations with respect to their thermal equilibrium density ($n_T$) is photo-injected by the pump-pulse. The perturbation of the electron distribution can be mimicked both by introducing an effective temperature T* (68) and an effective chemical potential $\mu$* (34). Both the models predict a decrease of the superconducting gap $\Delta(n_I, T)$ with the excitation density $n_I$ (expressed in units of $4N(0)(0,0)$) but with important differences (35).

Let's consider first the case of a d-wave superconducting gap, which is the case of cuprate superconductors. In the T* model the gap dependence can be approximated by $\Delta(n,0)/\Delta(0,0) \sim 1-32(3n_I)^{3/2}/\pi^3$ and a complete closing is obtained at $n_{cr} \approx 0.33$, causing a second-order phase transition to the normal state. The $\mu$* model reproduces a shift of the excitation distribution function decoupled from phonons. In this case the gap closing is slower, i.e., $\Delta(n,0)/\Delta(0,0) \sim 1-4\sqrt{2}n_I^{3/2}/3$, and, before the complete gap collapse at $n_I \approx 0.65$, the free energy of the superconducting state equals the normal state one. The free energy difference between the two phases, in units of the condensation energy $U_{cond} = N(0)2(0)/2$, is expressed (35) by $\Delta F(n_I) \sim -1/2 + 16\sqrt{2}n_I^{3/2}/3$ and reduces to zero at $n_{cr} \approx 0.16$. The most important consequence is that, within the $\mu$* model, a first-order phase transition from the superconducting to the normal state can take place. A remarkable result is that the differences between

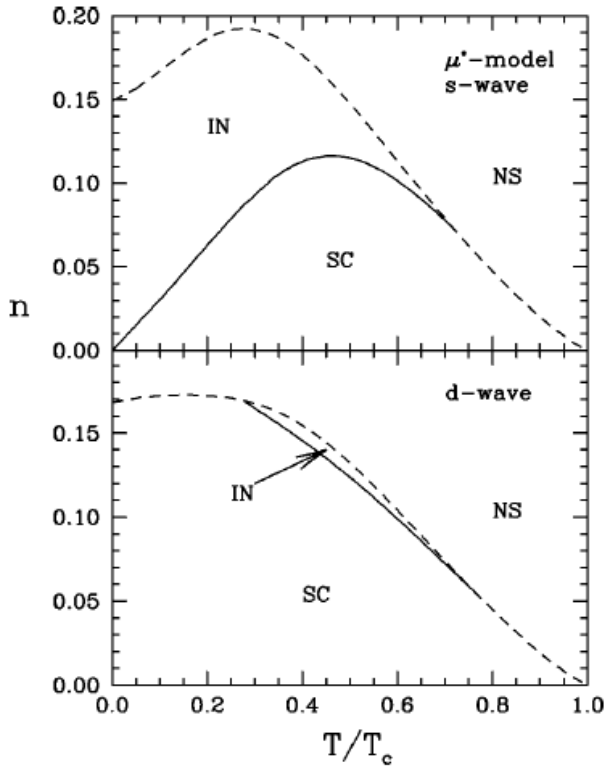


**Figure 2.9: Non-Equilibrium phase diagram, $\mu$* model** - Excess excitation vs temperature phase diagram predicted by the $\mu^*$ model in the case of a s-wave symmetry (top panel) and d-wave symmetry (bottom panel). SC is the superconducting phase, IN is the inhomogenous phase and NS is the normal state in the BCS picture.

the predictions of two models are not related to number of excitation injected into the system but rather to their energy distribution.

A similar situation is realized in the s-wave case. The non-equilibrium superconducting gap in this case has a linear dependence on the excitation density and it has the same analytic expression in both models for small perturbations, i.e., $\Delta(n,0)/\Delta(0,0) \sim 1 - 2n_I$. The free energy in $\mu^*$ model increases as $\Delta F(n_I) \sim -1 + 8n$, reaching zero and thus causing the first-order phase transition to the normal state at about $n_{cr} \approx 0.15$.

The phase diagram predicted by the $\mu^*$ model for both s-wave and

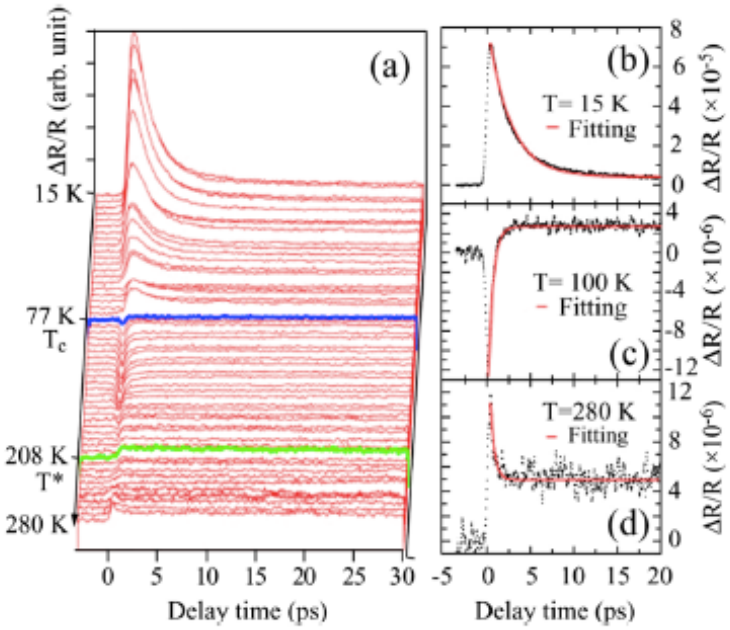


**Figure 2.10: Temperature dependence of $\Delta R/R$ signal at 1.5 eV on an underdoped Bi2212 sample** - $\Delta R/R(t)$ signal measured at low fluence on an underdoped Bi2212 sample as function of temperature. Figure taken from (79)

d-wave symmetry is reported in Fig. 2.9 (figure taken form (35)). An important difference between the two phase diagrams is the extension of the inhomogenous phase where superconducting and normal phases coexist. In both cases the transition is first-order but in the d-wave case it happens between homogenous phases, while in the s-wave case it results in phase separation and an inhomogenous admixture of normal and superconducting phases in most part of the non-equilibrium phase diagram.

### 2.3.3 Pump-probe optical experiments on cuprates

In the early '90, just after the advent of ultrafast laser sources, the HTSC and many other materials have been subject of ultrafast time-resolved experiments in non-equilibrium conditions. At the beginning

the investigation on HTSC mainly focused on the determination of the room temperature e-phonon coupling constant $\lambda$ (80), following the theoretical work of Allen on the Two-Temperature model (81) and the experimental work of Brorson on BCS superconductors (82). In the Two-temperature model, electrons and phonons are treated as two different subsystems, with two different temperatures during the time-resolved experiment. The set of coupled equations governing their dynamics is:

$$C_e \frac{dT_e}{dt} = I(t) - G \cdot (T_e - T_L) + \vec{\nabla} \cdot (k_e \vec{\nabla} T_e) \tag{2.18}$$

$$C_L \frac{dT_L}{dt} = G \cdot (T_e - T_L) + \vec{\nabla} \cdot (k \vec{\nabla} T_L) \tag{2.19}$$

where G is giving the coupling between the electronic and phononic subsystem and it can be expressed as (81),

$$G = \frac{3\hbar\gamma_e}{\pi k_B} \lambda \langle \omega^2 \rangle \tag{2.20}$$

with $\gamma_e$ being the linear coefficient of the electronic specific heat, $\lambda$ being the e-ph coupling parameter obtained from the Eliashberg theory of BCS superconductivity and $\langle \omega^2 \rangle$ is the second moment of the phonons distribution.

However this simple model is not sufficient to account for the double-decay dynamics of the optical properties observed in cuprates and an extension of this model, called the Three-Temperature model has been proposed (83, 84). In this model the first, very fast, dynamics represent the interaction between the electronic system and a subset of highly coupled phonons, while the slower dynamics account for the subsequent relaxation of energy towards the other phononic modes.

In the superconducting state the dynamics is much different. When the experiment is performed at low pump fluence intensity (*low-excitation regime*), several common trends have been recognized based on the large amount of experimental data reported on HTSC: i) the appearance

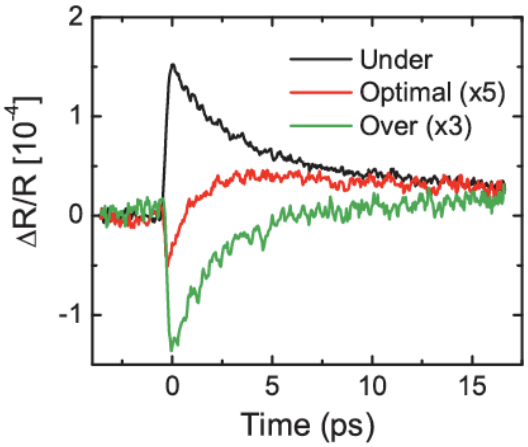


**Figure 2.11: Doping dependence of $\Delta R/R$ signal at 1.5 eV** - $\Delta R/R(t)$ signal measured at low fluence on three different Bi2212 single crystals. The underdoped sample exhibit a positive variation of the reflectivity, with the same variation has opposite sign on the overdoped sample. The crossover between the two behavior is locate at optimal doping. Figure taken from (76)

below $T_C$ of a $\Delta$R/R signal proportional to the photoexcited quasiparticle (QP) density (27, 28, 29, 30, 65, 71, 72, 73, 74, 75, 76, 77, 78), ii) an intensity and temperature dependent decay time of this superconducting component (30, 65, 71, 72, 74, 75, 76, 77, 78) iii) the substantial equivalence of the decay time observed probing at 800 nm and both the condensate and superconducting gap recovery dynamics observed in the THz (77) and in the mid-infrared spectral region (85) respectively iv) a different sign of the superconducting optical response at 1.5 eV between the underdoped and the overdoped side of the phase diagram (see Fig.2.11) (76).

At low fluence, the superconducting signal (SCS) reported in figure 5.3 is satisfactorily reproduced by the RTE when considering only the $I_{ph}(t)$ term, i.e. assuming that the pump energy is mainly absorbed through excitation of the phonon population. This result is in agreement with both theoretical predictions within the T* model (35) and experimental observations on YBCO (86, 87) and $MgB_2$ (70). In the

fitting procedure we assume $\beta = 0.1\text{cm}^2/\text{s}$, as reported in the literature (71). The determined free parameters at low fluence ($\Phi = 1\ \mu\text{J/cm}^2$) are $\gamma = (4.5\pm0.5)\ \text{ps}^{-1}$ and $\gamma_{esc}$=$(3.3\pm0.1)\ \text{ps}^{-1}$. These value are compatible with both the results obtained on LSCO (28) and the theoretical estimations of anharmonic processes in YBCO (72).

# Chapter 3

# Materials & Methods

Broadband time-resolved techniques with femtosecond time resolution has been applied in the past on liquids and transparent substrates to study ultrafast processes in molecules and their environment (88, 89, 90). However their application to condensed matter systems and in particular to superconducting materials at low temperatures required the development of new high-resolution tunable repetition rate spectroscopic techniques (26, 27), which have become available only recently (91).

The experimental results reported in this thesis work are the widest spectroscopic time-resolved data reported so far on a superconducting sample and come from a series of measurements with several kind of optical pump-probe techniques. These experiments have been performed in the T-Rex Lab (Fermi@Elettra, Trieste) and in the Elphos Lab (Universitá Cattolica, Brescia). In the former a 800 nm, 50 femtoseconds, tunable-repetition rate (below 300 kHz) amplified Ti:Sa laser source, coupled to a Optical Parametric Amplifier (OPA) has been used for tunable wavelength pump-probe experiments in the spectral range 0.5-1.1 eV and 1.8-2.2 eV. Concerning the latter a cavity dumped Ti:Sa oscillator (repetition rate below 27 MHz) has been coupled to a Photonic

Crystal Fiber (PCF) to generate Supercontinuum light and perform broadband pump-probe experiments in the spectral region 1.1-1.9 eV.

Single color pump-probe measurements at 1.5 eV have been done in the Elphos Lab to take advantage of the easily tunable and higher repetition rate. The details of the two set-ups are described respectively in sections 3.1 and 3.2. Finally the section (3.3) is devoted to sample preparation and characterization.

## 3.1 Infrared pump-tunable wavelength probe set-up

The scheme of the set-up for the generation of the pulses used in this technique is shown in Fig. 3.1. Only a brief description of the pulse generation process is given here and more details can be found elsewhere (92, 93). A solid-state diode-pumped Nd:vanadate (Nd:YVO4) laser (Coherent Verdi V18) generates continuous light at a wavelength of 532 nm and power of 18 W. This laser constitutes the pump for both an optical Ti:sapphire oscillator (Coherent Mira Seed), using about 8 W of the Verdi power, and a Regenerative Amplifier (Coherent RegA Model 9050), using the remaining 10 W.

The 40 nm broad and 50 fs short laser pulse produced by Mira Seed is temporally broadened up to 30 ps by the Stretcher in order to minimize peak intensity before amplification and thus increase the efficiency of the process. The seed pulse enters the RegA system and it is amplified in a Ti:$Al_2O_3$ crystal by coupling with the 532 nm pump laser. After several trips in the cavity, the amplified pulse is switched out by a RF-controlled $SiO_2$ Bragg-cell (Cavity Dumper). The 800 nm amplified pulse is then compressed down to of 50 fs by the Compressor. The repetition rate of the RegA system is tunable, with $f_{rep.rate} < 300$ kHz. The maximum energy per pulse is reached at 100 kHz and it is about 5 $\mu$J.

After amplification and compression the laser beam is split into two parts by a beamsplitter: the reflected part (between the 10 and the 30%) is used as the pump pulse in the pump-probe experiment,

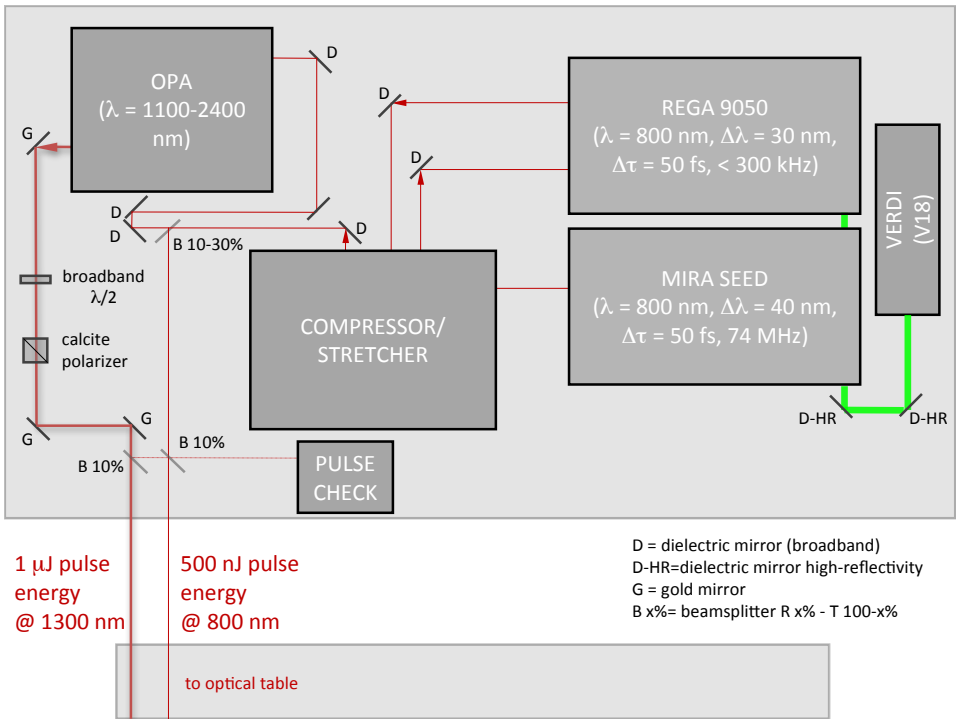


**Figure 3.1: Set-up for generation of tunable IR pulses** - See text for the description of the generation process.

while the transmitted one is used to generate tunable wavelength IR pulses through optical parametric amplification in the OPA 9850. This device is based on a non-linear process of four-wave mixing where, under proper phase matching conditions and spatial and temporal coincidence with a Supercontinuum pulse, a pump photon ($\omega_p$) is converted through a BBO crystal into two photons called *signal* and *idler* with frequencies respectively $\omega_s$ and $\omega_i$ respectively. The sum of their frequencies is fixed, by the energy conservation principle, to the value of the pump frequency: $\omega_p = \omega_s + \omega_i$. Their values are determined by the phase matching conditions which vary with temperature and with the angle between the pump and the optical axis of the crystal. Changing the angle between the crystal and the 800 nm pump, it is possible to tune

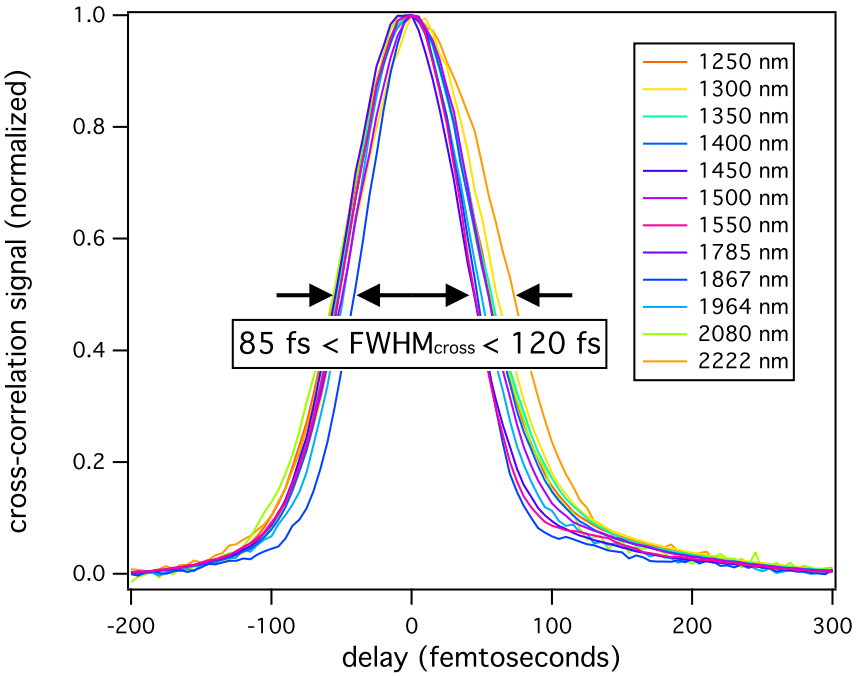


**Figure 3.2: OPA pulse characterization** - OPA pulse characterization through OPA - 800 nm cross-correlation.

$\omega_s$ and $\omega_i$ in a frequency range from 1100 nm to 1600 nm for the signal and from 1600 nm to 2600 nm for the idler. As the idler and the signal are orthogonally polarized (s and p respectively), a broadband waveplate and a polarizer is introduced to select one of the two pulses and possibly rotate its polarization (see Fig. 3.1).

The OPA pulse profile has been measured both with an auto-correlation technique and a cross-correlation measurement on the 50 fs pump pulse. The results obtained in the latter case are shown in Fig. 3.2 at several wavelengths in the full spectral range used. The cross-correlation signal, which gives the temporal resolution for the pump-probe experiment presented here, has a FWHM between 85 fs and 120 fs.

The detailed dependence of the pulse width as a function of the pulse wavelength is given in Fig. 3.3. The pulse is slightly broader in the outer part of the spectral range considered.

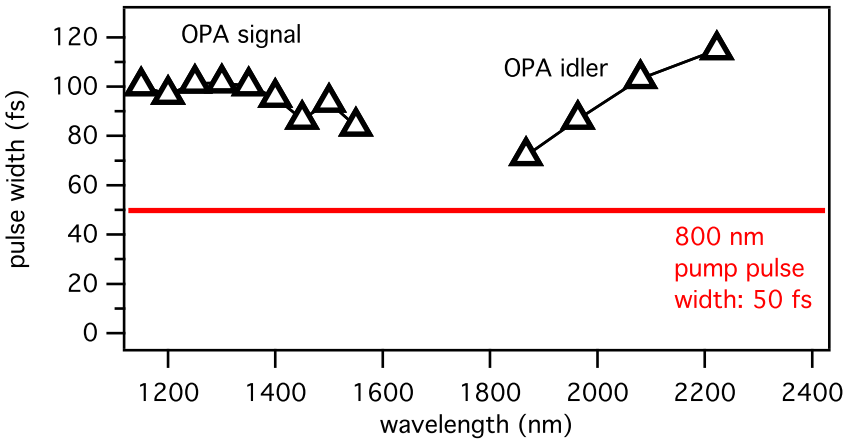


**Figure 3.3: OPA pulse widths** - OPA pulse widths at several wavelengths obtained from the data of Fig. 3.2.

The set-up for the pump-probe experiment is represented in Fig. 3.4. The pump (800 nm) beam passes through a delay stage based on two high-precision motorized translators, a 30 cm long PI delay line for slow movements and a small and fast APE delay line continuos movements at frequencies of about 1-2 Hz. The precision of both delay stages is of the order of 1 $\mu m$. The control of the pump beam path allows the time-resolved scan of the optical properties. Because of the double passage of light a 1 $\mu m$ step corresponds to 6.6 fs in terms of delay between pump and probe. The delay stage is controlled in real-time by the same PC used for acquisition.

A motorized variable attenuator precisely controls via software the intensity of the pump pulse, while a mechanical high-speed chopper allows the high-frequency modulation of this pulse for lock-in detection. The main advantage of high-speed modulation is to minimize the $1/f$ shot noise in the detection. In the experiments reported in this thesis the modulation frequency was set to 13 kHz. The pump beam is then focused on the sample with a plano-convex lens with focus of 300 mm.

The tunable wavelength probe beam is properly attenuated to avoid self-induced effects on the sample and then it is focused on the sample with a silver spherical mirror with effective focal length of 200 mm. The

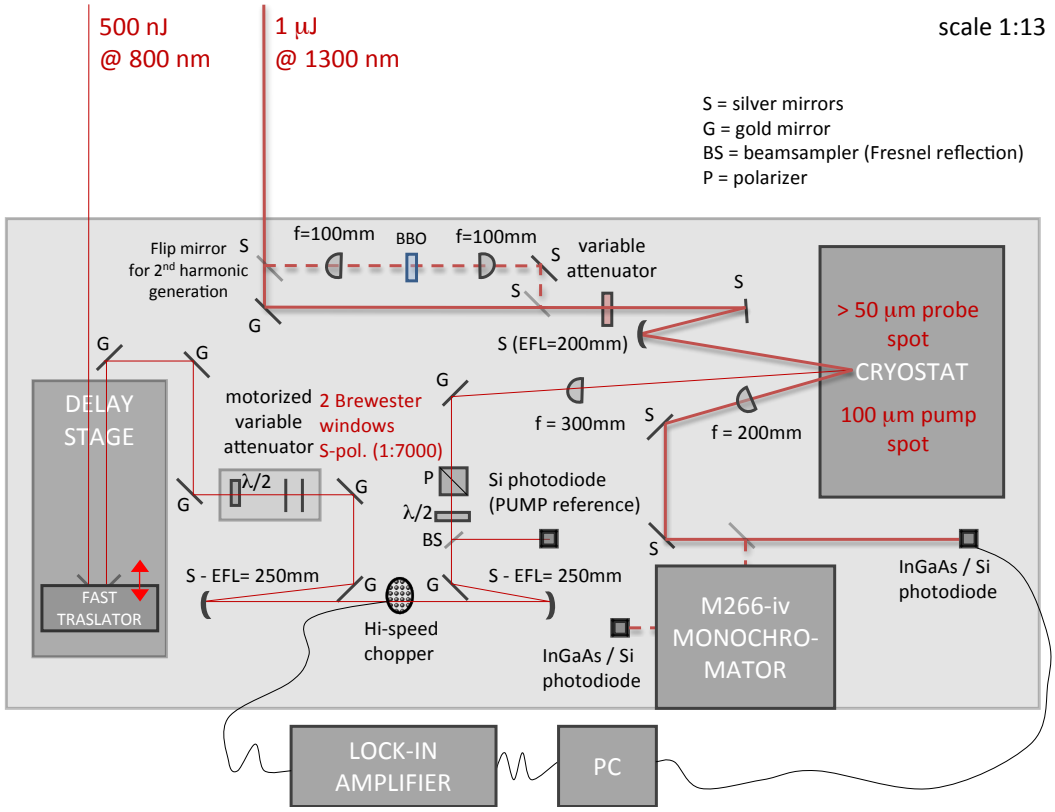


**Figure 3.4: Set-up for tunable IR measurements** - See text for the description of the pump-probe scheme.

use of the spherical mirror instead of a plano-convex lens minimizes the beam position variations at different wavelength. A stage for second harmonic generation can be used to double the probe frequency to reach the wavelength range of 700-550 nm (only the *signal* is doubled in the experiments reported). In this case two plano-convex lenses are used to focus the pulse on a BBO crystal properly oriented for phase matching.

The size of the pump and probe beams on the sample are measured by imaging the spots in the focal plane of a CCD camera. The pump spot is generally about 90-100 $\mu m$, while the probe spot varies between 50-80 $\mu m$. The sample is placed in an open-cycle cryostat which cool down the sample to a minimum temperature of 10 K.

The detection is based on a single photodiode (generally InGaAs or

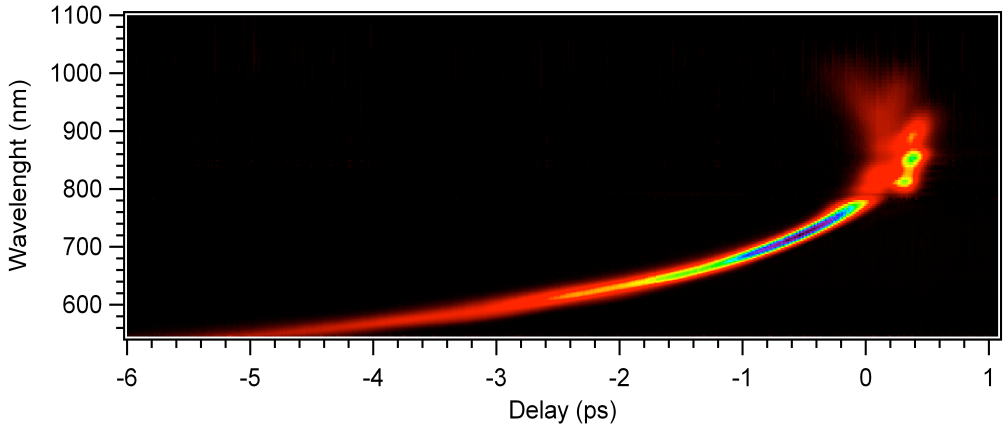


**Figure 3.5: Supercontinuum pulse characterization** - Supercontinuum pulse characterization through frequency-resolved optical gating via two-photon absorption in thick ZnSe plate (gap 2.1 eV).

Si) and subsequent lock-in amplification of the signal modulated at the chopper frequency ($\sim$ 13 kHz). A Solar M266-iv imaging monochormator is also used to increase the spectral resolution of the measurements.

## 3.2 Infrared pump-Supercontinuum probe set-up

The first stage of the laser system is a diode pumped Nd:Yag laser (Coherent Verdi V10) which provides a beam with wavelength $\lambda$=532 nm and maximum output power of 10 W. This laser pumps a Ti:sapphire oscillator (Coherent Mira 900) converting the input continuous wave beam into a train of ultrafast pulses characterized by a wavelength $\lambda$=800 nm and a temporal width of 120 fs. The cavity of the oscillator is equipped by a cavity dumper which is an acousto-optical switch that allows to vary continuously the repetition rate of the laser from 1 MHz to 200 Hz and to increase the energy per pulse. The output energy per pulse is about 50 nJ at 100 KHz of repetition rate.

While the optical pump-probe scheme is very similar to the one described in the previous section, the main difference arises on the

probe line, where Supercontinuum light is produced by focusing the probe pulses with an aspherical lens into a photonic crystal fiber. The fiber is positioned on a home-made launch system equipped by three translational degrees of freedom and a tilting mechanism, in order to optimize the coupling of the laser into the fiber itself. Strongly non linear processes inside the fiber broaden the 800 nm pulse generating a broadband pulse characterized by a spectral content ranging from 450 nm to 1500 nm and a complex spectral chirp. After the fiber the white light pulse is parallelized by an achromatic doublet and then refocused by another doublet with focal length f =100mm. An optical window, placed before the last doublet, samples the probe. This reference is used to monitor and compensate the probe intensity oscillations during the measurements. Both the reference and the signal reflected by the sample are dispersed by a prism and collected by two Si-array of 128 pixels. A spectral slice, whose width ranges from 2nm at 700nm to 6nm at 1100nm, is acquired by each pixel of the array, corresponding to a constant temporal resolution of $\sim$ 120 fs. A fast digitizer performs the scan of the arrays. Because of the large difference between the scan frequency of the array and the repetition rate of the laser, a single-shot detection is not feasible and it is necessary to integrate many pulses. The pump beam is chopped at a low frequency (typically 30 Hz), and, at the same time, the pump modulation is acquired by a photodiode and digitalized by a data acquisition device (NI-DAQmx M-series) which is synchronized with the fast digitizer. In this way it is possible to discriminate between pumped and the unpumped pulses. At the end of a single acquisition the pump-induced variation of signal is obtained by mediating and subtracting the two signals. To prevent the probe intensity fluctuations from affecting the measurement, the reflectivity variation is divided by the reference signal. The sensitivity of the array of photodiodes ranges from 500 nm to about 1000 nm, outside this range the response of the photodiodes drops. Only this portion of the supercontinuum light will be used in the measurements reported in this work.

The temporal properties of the supercontinuum pulse as a function of frequency are characterized with through optical gating via two-photon absorption in a thick ZnSe plate. The gating pulse is the 800 nm pump pulse which is focused on the plate, in coincidence with the supercontinuum pulse. After the plate, the supercontinuum pulse is dispersed by a prism and it is collected on the linear photodiode array, as reported above. This method is based on the fact that carriers can be excited across the gap of ZnSe (2.1 eV), through a two-photon absorption process only if temporal coincidence between part of its spectrum and the gate pulse, is realized. The result of this measurement is shown in Fig. 3.5. With this technique it is possible to obtain the temporal dispersion of the pulse and the pulse width at each frequency. The pulse is short ($\sim$ 150 fs) and have a gaussian profile in the high energy region (below 800 nm in Fig. 3.5). On the contrary at low energies the pulse width become larger than 200 fs and the pulse shape deviates from a gaussian profile. The effect of this broadening can be clearly seen as a pre-pulse (t $< 0$) effect in the experimental $\Delta R/R(\omega, t)$ matrices reported in this thesis work. This effect is an artifact of the supercontinuum pulse broadening at low energies.

## 3.3 Sample preparation and characterization

Pump-probe measurements have been performed on $Bi_2Sr_2Ca_{0.92}Y_{0.08}Cu_2O_{8+\delta}$ single crystals. The Y-substituted Bi2212 single crystals were grown in an image furnace by the traveling-solvent floating-zone technique with a non-zero Y content in order to maximize Tc (38). Overdoped crystals were annealed in flowing oxygen in order to increase the hole concentration and reach the overdoped side of the phase diagram. The samples were subsequently homogenized by further annealing in a sealed quartz ampoule, together with ceramic at the same oxygen content. The results of the magnetic susceptibility measurements on the sample under study in this thesis are shown in Fig. 3.6 for the sample OD86, OP96 and UD83. For convention the critical temperature $T_C$ is

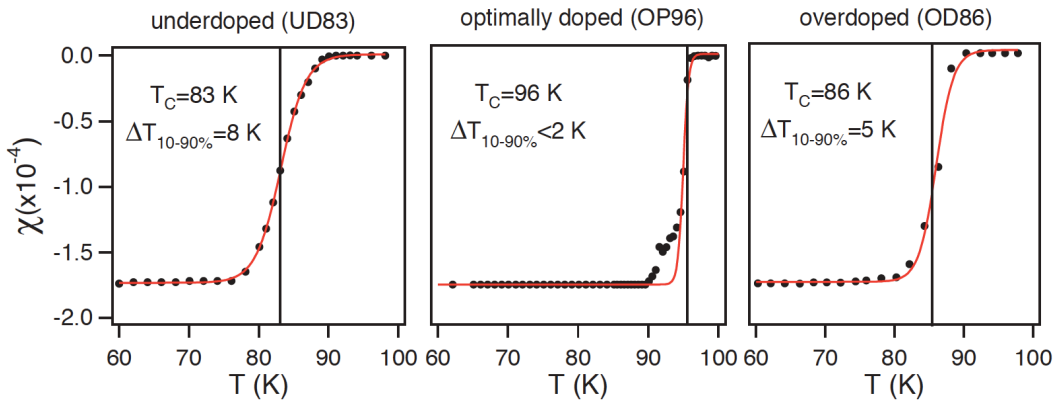


**Figure 3.6: Samples characterization** - Susceptibility measurements on the sample used in this work. The strong diamagnetic signal is associated with the superconducting state below $T_C$. The midpoint of the onset of superconductivity is chosen as the nominal $T_C$ value, while the transition amplitude is calculated as the temperature interval between the 10% the 90% and drop of the susceptibility signal

assigned to the midpoint of the superconducting transition amplitude. The same characterization has been done also on the OD78 sample (not shown), giving a transition amplitude of $\Delta T \sim 10$ K.

## 3.4 Data analysis and Singular Value Decomposition

In the spectroscopic time-resolved experiments performed in this thesis the outcome is a time-energy matrix $\Delta R/R(\omega, t)$. There are several approaches to the data analysis of this matrix. One can consider for example the spectral traces $\Delta R/R(\omega)$ obtained at fixed $t$, analyze them separately and then later reconstruct a time-dependence of each particular parameter used to analyze the spectral data. This approach is particularly time-consuming since a differential model with many free parameters is used to compute the $\Delta R/R(\omega)$ (see section 4.3) at each time instant $t$. Moreover, while this method provides very interesting

information on the dynamical interplay between microscopic parameters when few of them are used to model the data (93), it become less transparent when the free parameters are many and several kind of excitations are photoinjected, like in the case of the superconducting state of Bi2212 samples.

A alternate approach would start instead from the dynamical trace $\Delta R/R(t)$ integrated on a narrow frequency range $\Delta\omega$. By fitting the time trace with multiple exponentials one can distinguish different components by their different relaxation rates. However this is particularly dangerous when a component exhibit a slow rise time (and this is the case of the superconducting state as it will be shown in section 4.2.3) since it is not possible, by analyzing single traces independently, to disentangle a positive $\Delta R/R$ signal raising in time from a negative $\Delta R/R$ signal decaying in time.

These problems can be solved by adopting a numerical decomposition method for the $\Delta R/R(\omega, t)$ matrix where both the spectral ($\Delta R/R(\omega)$) and temporal ($\Delta R/R(t)$) information are used to properly decompose the data. In the following I explain the numerical method used to decompose the $M$x$N$ data matrix, called $X$, and at the end of this section I will come back on the meaning of this decomposition.

The Singular Value Decomposition (SVD) procedure decomposes the data matrix $X$ into a product of three matrices,

$$X = USV^T \tag{3.1}$$

where $U$ is an $M$x$N$ matrix whose columns are called the *left singular vectors*, $\mathbf{u}_k$, and form an orthonormal basis for the spectral traces $\Delta R/R(\omega)$, $S$ is a diagonal matrix whose elements are called *singular values* and $V^T$ is an $N$x$N$ matrix containing the elements of the *right singular vectors*, $\mathbf{v}_k$, and form an orthonormal basis for the dynamical traces $\Delta R/R(t)$. By convention, the ordering of the singular vectors is determined by high-to-low sorting of *singular values*, with the highest singular value in the upper left index of the $S$ matrix. For

a square, symmetric matrix $X$, singular value decomposition is equivalent to diagonalization, or solution of the eigenvalue problem. Moreover the SVD method gives the same result of the Principal Component Analysis (PCA) when the principal components are extracted from the *covariance matrix* (94).

SVD method can be applied to find a lower-rank matrix which reproduces $X$,

$$X^{(l)} = \sum_{k=1}^{l} \mathbf{u}_k s_k \mathbf{v}_k \tag{3.2}$$

where $X^{(l)}$ is the closest rank-l matrix to $X$. The term closest means that $X^{(l)}$ minimizes the sum of the squares of the difference of the elements of $X$ and $X^{(l)}$, $\sum_{ij} |x_{ij} - x_{ij}^{(l)}|^2$.

SVD has been successfully used in a number of areas such as the analysis of spectroscopic data (95), of molecular dynamics simulations (96), of the temporal variation of genome-wide expression (97) and of time-resolved macromolecular x-ray experiments (98).

In this thesis the SVD has been applied, using LAPACK routines, to analyze the low-fluence time-energy matrices $\Delta R/R(\omega, t)$. The matrices are generally well reproduced by the first three components. The first one, called the *first principal component*, generally contains about the 80 % of the signal of the original matrix.

In conclusion the SVD is a powerful tool to recognize in the experimental data the fundamental spectral responses, $\mathbf{u}_k$ or equivalently $\Delta R_k/R(\omega)$, and the corresponding temporal evolution, $\Delta R_k/R(t)$. Each spectral response $\Delta R_k/R(\omega)$ and temporal trace $\Delta R_k/R(t)$ are associated with a particular kind of quasi-particle $k$ which produces a particular kind of perturbation of the dielectric function on a certain timescale.

# Chapter 4

# Low-excitation regime

## 4.1 Introduction

In this chapter I report the low-fluence time-resolved optical spectra obtained on overdoped samples by joining the pump-probe experiments performed with the optical parametric amplifier (OPA) and the supercontinuum source (See Chap. 3). By exploiting both these techniques it is possible, for the first time, to measure the dynamical optical response of a cuprate in the entire range from 0.5 eV to 2.2 eV under photoexcitation at 1.5 eV (pump photon energy). The probe spectral range involves both intraband and interband optical transitions. This experiment allows to distinguish different low-lying quasi-particles (QPs) by their different perturbation of the dielectric function and, in turn, it is sensitive to the macroscopic phase of the material as I will show in this chapter.

The low-fluence regime is here regarded as the regime where the density of photo-excitations is small enough to produce variations in the low-energy excitation spectrum which are much smaller than their typical energy scales. For example in the superconducting state the

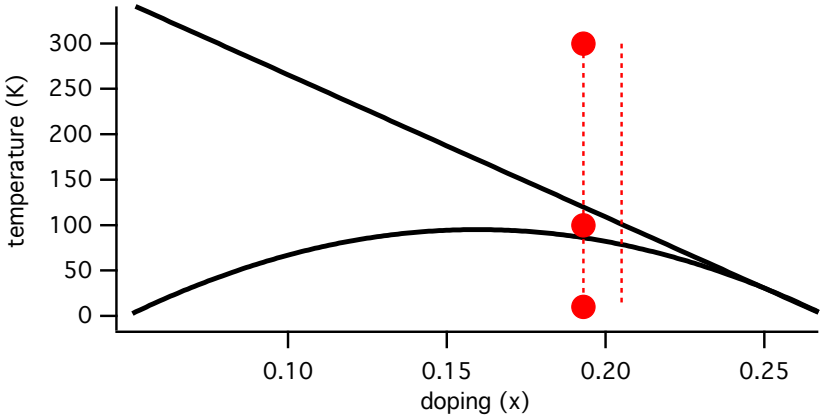


**Figure 4.1: Data set reported in chapter 4** - Phase diagram of Bi2212. Solid circles represent the three complete (OPA + supercontinuum) optical spectral responses reported in Sec. 4.2 on sample OD86. The dashed lines represent the data set reported in sections. 4.4 and 4.5, where a single color pump-probe technique is exploited to have a continuos temperature-dependent series of data on the OD78 and OD86 samples respectively.

condition is $\delta\Delta_{SC}(n) << \Delta_{SC}(0)$, where $n$ is the density of photoexcited quasi-particles. As it will be show in the following chapter, the pump fluence required to guarantee this condition in the superconducting state of overdoped samples is $\phi < 20\ \mu J/cm^2$. In pseudogap and normal phases this condition is less strict and non-linear effects are appearing at higher fluences ($\sim 200\ \mu J/cm^2$, see Sec. 6.2.1).

In section 4.2 I report the experimental results obtained at 300 K (normal state, Sec. 4.2.1), 100 K (pseudogap, Sec. 4.2.2) and 10 K (superconducting phase, Sec. 4.2.3) on the OD86 sample (see Chap. 3 for the details on sample preparation and properties). In Fig. 4.1 I show the position of these points in the temperature-doping phase diagram. In section 4.3 I develop a differential model for the time-resolved dielectric function which describes the main features of the experimental optical spectra.

In section 4.4 I report a detailed temperature dependence study of the interband spectral weight transfer on a more strongly overdoped sample (OD78). The sample choice here gives a solid argument for

the applicability of the BCS-like RT model (64) to interpret the QP dynamics in the superconducting state. The decay rate of the signal appearing at $T_C$ is found to be proportional to a power law of the superconducting order parameter $\Delta$. In section 4.5 I report a similar temperature-dependent study on the photoinduced intraband spectral weight transfer. The signal here has a much higher onset temperature and it smoothly evolves into the superconducting optical response at $T_C$.

## 4.2 Optical response of quasi-particles

The time-resolved optical spectra ($\Delta R/R(\omega, t)$ time-energy matrices) shown in this section are obtained by joining experiments performed with a supercontinuum pulse to a series of more than ten measurements performed with the tunable OPA pulse in the 0.5-1.18 eV spectral range with the fundamental frequency and in the 1.8-2.2 eV range with the second harmonic. The supercontinuum pulse is sampled with a diode array (128 pixels), giving a continuos spectral information between 1.2 and 1.9 eV. The spectral resolution in this case is $\sim$ 8 meV. The OPA pulse have energy resolution limited by the spectral width (FWHM) of the gaussian profile of the beam, with an average value of $\sim$ 30 meV. To obtain a continuos time-energy matrix the OPA data have been weighted with their own gaussian spectral profiles. Time-resolution of the OPA data set is very narrow (50-80 fs resolution), while it is almost doubled in the case of the supercontinuum pulse (between 100 fs at high energies and 200 fs at low energies). See Chap. 3 for a full description of the experimental apparatus and for more details on the pulse characteristics.

The time-energy matrices have been analyzed adopting the Singular-Value Decomposition (SVD) method (see Chap. 3). This approach allows to recognize the first principal component of each experimental matrix and to evaluate the importance and shape of residual components. The first principal component is interpreted as the signal of the fundamental quasi-particle of that particular phase, i.e., as the main

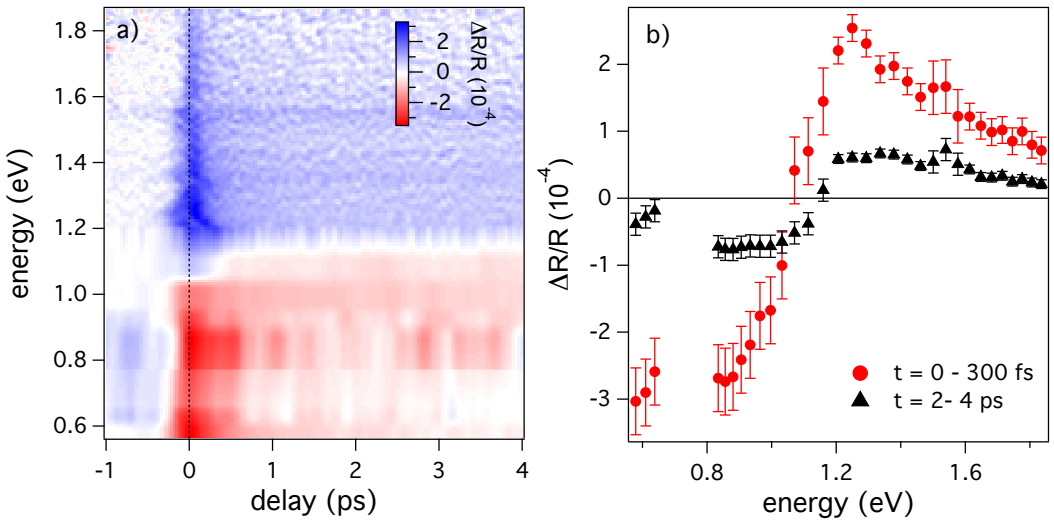


**Figure 4.2: Normal state optical response (OD86)** - a) Time-energy matrix of reflectivity variations at 300 K on the OD86 sample at a pump fluence of 10 $\mu J/cm^2$. b) Spectral trace at two different time delays. The $\Delta R/R(\omega, t)$ is integrated in time between 0 and 300 fs to obtain the impulsive response and between 2 and 4 ps for the quasi-equilibrium one. Each point of the spectral trace is an average of 5 pixels of the $\Delta R/R(\omega, t)$ matrix. The error bars take into account the noise level of the $\Delta R/R$ signal and possible fluctuations of experimental parameters such as pump fluence fluctuations and spatial pump-probe beams misalignments.

contribution in the $\Delta R/R(\omega, t)$ time-energy matrix coming from a particular kind of perturbation of the dielectric function $\Delta R/R(\omega)$ with its associated dynamics $\Delta R/R(t)$.

### 4.2.1 Normal state

At room temperature the sample under investigation (OD86) is in the normal state. The time-resolved optical spectrum obtained at a pump fluence of 10 $\mu J/cm^2$ is reported in panel a) of Fig. 4.2. The optical response appearing after photoexcitation (t > 0) has a positive $\Delta R/R$ signal (in blue) above 1.0 eV, with maximum around 1.3 eV, and it changes sign below 1.1 eV. The relaxation dynamics of the positive and the negative signal are very similar. The zero-crossing energy position

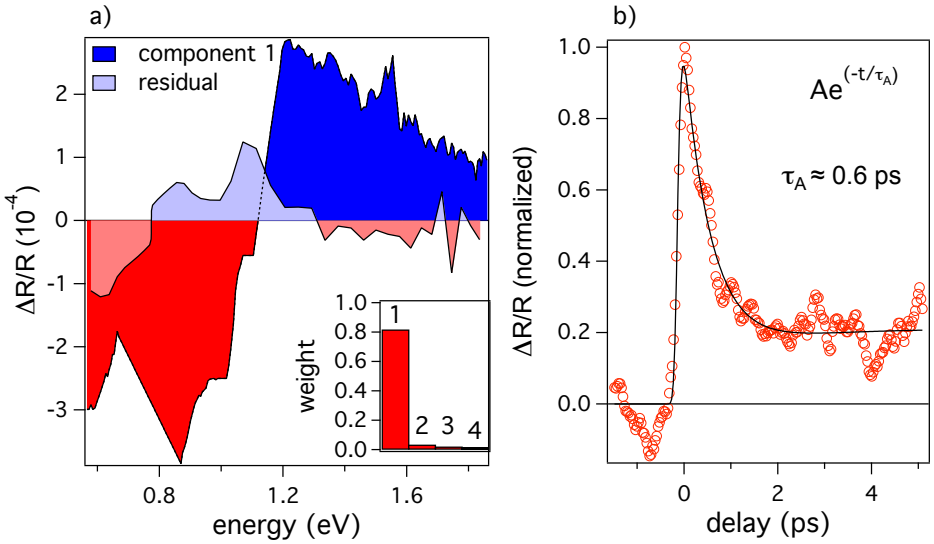


**Figure 4.3: Normal state signal, SVD decomposition** - a) Principal and residual components obtained after SVD analysis. In the inset the weight, i.e., the singular value, of the first four components is reported. b) Time-trace of the principal component.

(narrow white band) has little variations in time and mostly on the fast timescales. In Fig. 4.2b I report the averaged spectral responses on the short and long timescales. The small difference observed in the spectral shape here suggests that the effect of the pump laser pulse on the dielectric function of the normal state is very similar to an impulsive heating effect. In section 4.3.2 I will discuss in more detail this aspect.

The SVD analysis (Fig. 4.3a) shows that about 80 % of the $\Delta R/R(\omega, t)$ signal reported in Fig. 4.2a can be represented with a principal component characterized by a sign change at 1.1 eV and very similar positive and negative signal intensities ($|\Delta R/R_{max}| \sim 3\text{x}10^{-4}$). The sum of the residual components have a spectral positive feature between 0.8 and 1.3 eV, while it is negative outside this range. The time-evolution of the principal component obtained by the SVD analysis is reported in panel b of the same figure. Here the dynamics is fitted with a single exponential decay with decay time 0.6 ps, convoluted to an average time shape of the pulses ($\sim$ 120 fs). A fit with a double exponential

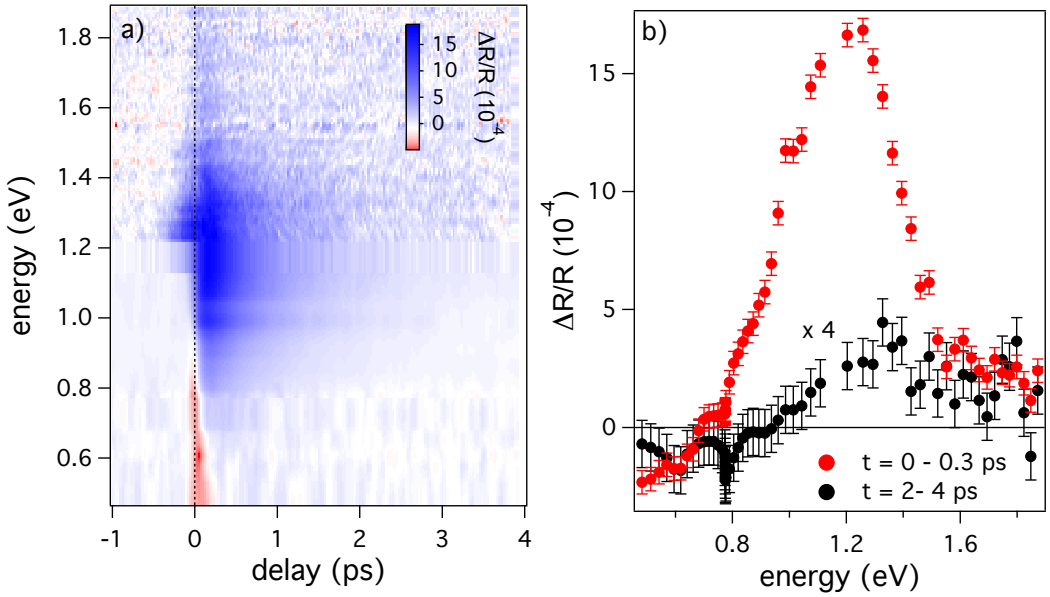


**Figure 4.4: Pseudogap phase dynamical spectrum** - a) Time-energy matrix of reflectivity variations at 100 K on the OD86 sample at a pump fluence of 40 $\mu J/cm^2$. b) Spectral trace at two different time delays. The $\Delta R/R(\omega, t)$ is integrated in time between 0 and 300 fs to obtain the impulsive response and between 3 and 4 ps for the quasi-equilibrium one. Each point of the spectral trace is an average of 4 pixels of the $\Delta R/R(\omega, t)$ matrix.

decay does not decrease significantly the $\chi^2$. The temporal trace of the residual component (not shown) is more noisy and has a fast decay time.

### 4.2.2 Pseudogap phase

The time-resolved spectrum obtained on sample OD86 at 100 K at a pump fluence of 40 $\mu J/cm^2$ is presented in panel a) of Fig. 4.4. In respect to the section 4.2.1 a higher pump fluence is used to increase the $\Delta R/R(\omega, t)$ signal in those spectral regions (below 0.8 eV and above 1.5 eV) where, at 10 $\mu J/cm^2$, it would have been less then the noise level. The measurement is still in the low-fluence regime because non-

linear effects related to strong pseudogap perturbation are observed on this sample above 200 $\mu J/cm^2$ as it will be discussed later on.

The $\Delta R/R$ signal observed in the first hundred of femtoseconds is positive above 1.0 eV, while it is negative below this energy. The decay of the negative response in the infrared region is very fast, while the positive signal centered at 1.2 eV has a slower decay time. This finding demonstrate that photoexcitation produces two different kinds of perturbations of the dielectric function which can be distinguished here by their different timescales.

In Fig. 4.4b the average spectral traces in temporal coincidence ($0 < t < 0.3$ ps) and at quasi-equilibrium ($3 < t < 4$ ps) are compared. While the quasi-equilibrium response is substantially the same to the normal state response (Fig. 4.2), the impulsive response has a completely different nature. I remark here that a thermal-difference reflectance study (99) of the same sample would have measure only the quasi-thermal spectral response, thus evidencing almost no difference between normal and pseudogap states. The fast spectral response is thus a peculiar feature of photoexcited quasi-particles in the pseudogap phase.

The SVD analysis it is a powerful tool here to disentangle the two different responses. Fig. 4.5 shows that more than 80 % of the $\Delta R/R(\omega, t)$ signal reported in Fig. 4.4 can be represented by a principal component which is positive above 0.7 eV, with a broad peak around 1.2 eV ($|\Delta R/R_{max}| \sim 2\text{x}10^{-3}$). The sum of the residual components is instead negative below 1.1 eV and it resembles the normal state principal component. The time-evolution of the principal component obtained by the SVD analysis is reported in panel b. The experimental dynamics can be fitted within the experimental uncertainty with a single exponential function with decay time 0.6 ps. A fit with a double exponential dynamics would decrease slightly the $\chi^2$, however this improvement remains within the experimental uncertainty, not allowing a real distinction between a single rather that a double decay dynamics of the principal component. Moreover in the case of a double exponential fit the use of four free parameters ($A$, $B$, $\tau_A$, $\tau_B$) seriously increases the

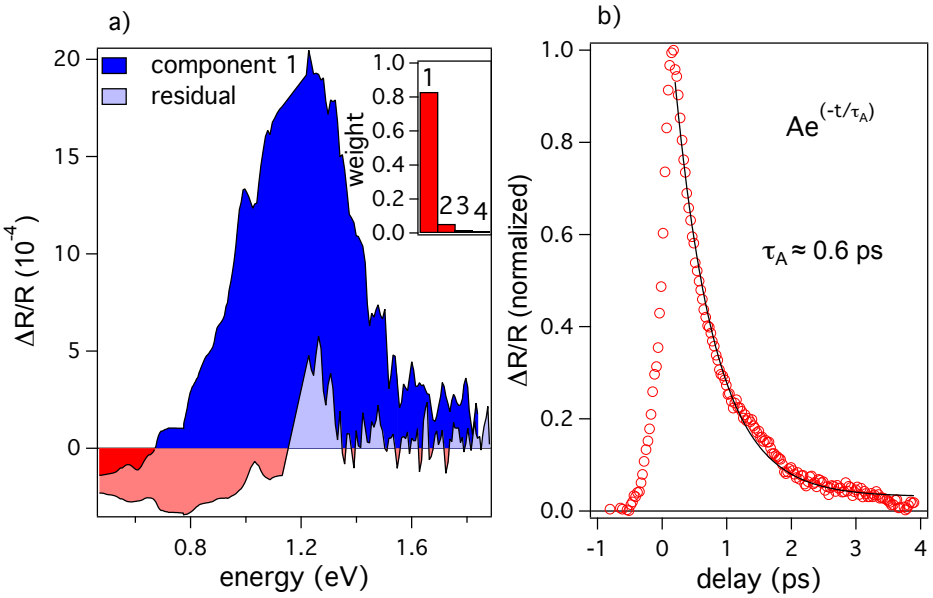


**Figure 4.5: Pseudogap signal, SVD decomposition** - a) Principal and residual components obtained after SVD analysis. In the inset the weight, i.e., the singular value, of the first four components is reported. b) Time-trace of the principal component.

uncertainty on their value because of their mutual correlation. Thus a single exponential fit is here preferable.

Nonetheless this is not in contradiction with the double exponential dynamics generally observed in $\Delta R/R(\omega, t)$ traces at a given $\omega$ (as in the case of a single-color pump-probe experiment). The total $\Delta R/R(\omega, t)$ signal is in facts a sum of principal and residual SVD components. The temporal trace of the residual component (not shown) contains a fast decay time ($\tau < 0.6$ ps) and an offset on the slow timescale, in analogy to the dynamics of the normal state principal component (4.3b). All these findings confirm that the SVD method efficiently decompose the experimental matrix in meaningful and more fundamental optical dynamical responses.

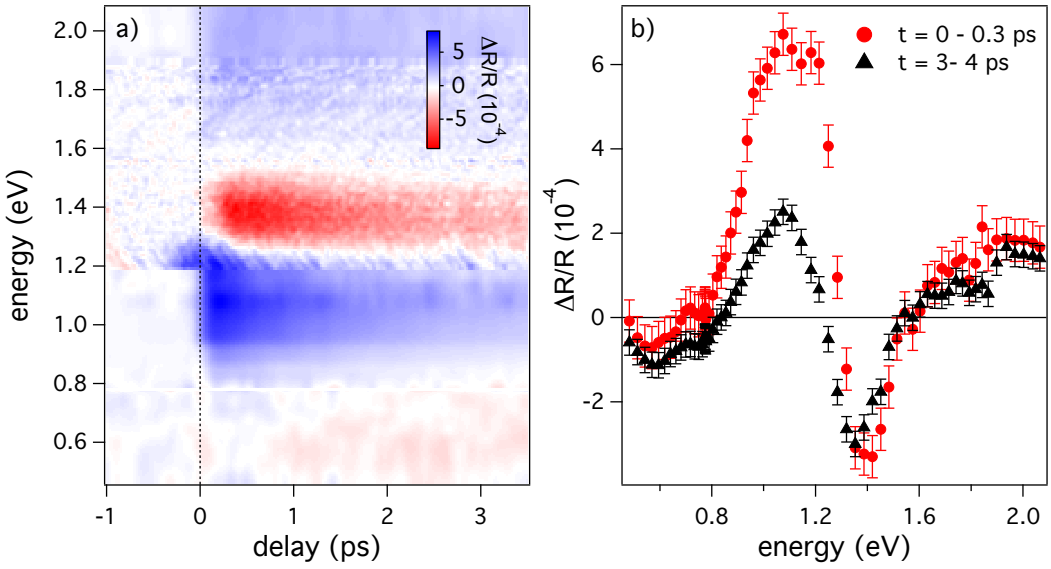


**Figure 4.6: Superconducting phase dynamical spectrum** - a) Time-energy matrix of reflectivity variations at 10 K on the OD86 sample at a pump fluence of 20 $\mu J/cm^2$. b) Spectral trace at two different time delays. The $\Delta R/R(\omega, t)$ is integrated in time between 0 and 300 fs to obtain the impulsive response and between 3 and 4 ps for the quasi-equilibrium one. Each point of the spectral trace is an average of 4 pixels of the $\Delta R/R(\omega, t)$ matrix.

### 4.2.3 Superconducting state

In the superconducting state, as expected from the literature (27, 28, 29, 30, 65, 71, 72, 73, 74, 75, 76, 77, 78), a new $\Delta R/R$ signal with slow decay time ($\tau > 1$ ps) appears in the time-resolved optical spectrum. This signal has been studied so far mainly at 800 nm wavelength (1.55 eV). The spectral shape of this signal in the 0.5 - 2.2 eV spectral region is here reported for the first time.

The dynamical spectrum measured at 10 K is shown in Fig. 4.6a. The pump fluence is kept here at 20 $\mu J/cm^2$, because saturation effects related to strong perturbation of the superconducting condensate are observed at fluences as slow as 50 $\mu J/cm^2$, as it will be discussed in detail in the next chapter. Two sharp spectral features are observed in the $\Delta R/R(\omega, t)$ signal, suggesting the involvement of particular inter-

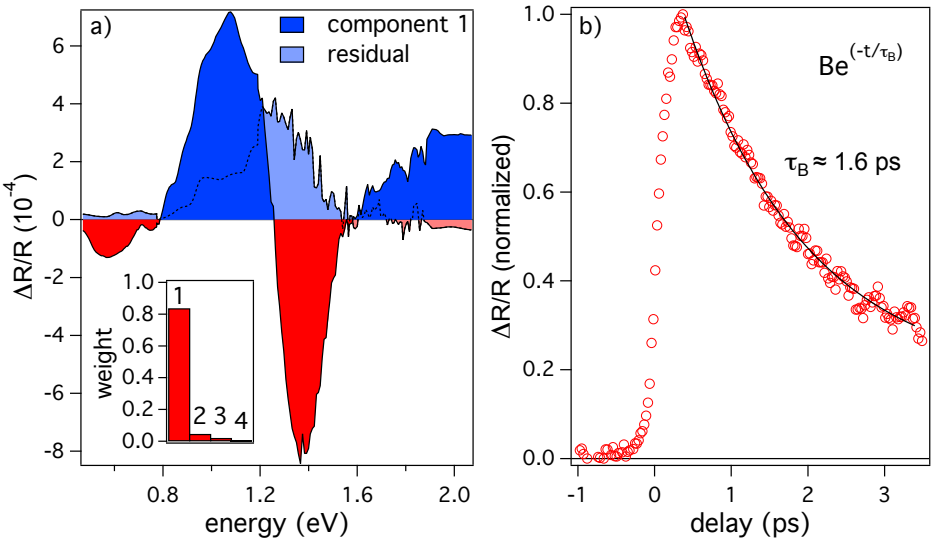


**Figure 4.7: Superconducting phase signal, SVD decomposition** - a) Principal and residual components obtained after SVD analysis. In the inset the weight, i.e., the singular value, of the first four components is reported. b) Time-trace of the principal component.

band oscillators. One feature is positive and centered at 1.1 eV, while the other is negative and centered at 1.4 eV (see Fig. 4.6b). Both these features have a common slow decay time, while they have a different dynamics on the fast timescale. In facts, their intensity ratio appears different on if integrated close to temporal coincidence or at long delays (Fig. 4.6b). At lower energies the $\Delta R/R(\omega, t)$ measured close to temporal coincidence (t $\sim$ 0) is extremely low, while a negative plateau resembling the normal state heating is reached on the long timescales.

SVD analysis of the $\Delta R/R(\omega, t)$ matrix includes both peaks in the principal component (Fig. 4.7), accounting for more than 80 % of the signal of the time-energy matrix. This component has a slow decay dynamics (see Fig. 4.7b) and it is best fitted with a single exponential function with decay time 1.6 ps. The sum of the residual spectral components is mainly positive with a broad peak around 1.2 eV (Fig. 4.7a) and a very fast temporal decay (not shown).

The SVD decomposition substantiate the common origin of the two

sharp spectral features at 1.1 and 1.4 eV in the superconducting state. In this view their different intensity ratio on the short timescales in interpreted as an effect related to a fast residual component (Fig. 4.7a). This residual component resembles the pseudogap principal component and suggest a coexistence in real-time of the two signals. This aspect will be discussed in more detail in chapter 6.

## 4.3 Differential model

In a first approximation one might expect that the signals observed in time-resolved reflectivity experiments are originated by variations of the electron distribution function affecting the optical transitions probability for a given set of allowed transitions between unperturbed initial and final states. This situation is well described by writing the absorption coefficient in terms of the *Fermi-Golden rule*

$$\alpha \propto \int d\epsilon N(\epsilon)N(\epsilon+\omega)|\mathbf{M}(\epsilon,\omega)|^2 f(\epsilon)\left(1-f\left(\epsilon+\omega\right)\right) \tag{4.1}$$

where $N(\epsilon)$ is the density of states at an energy $\epsilon$, $f(\epsilon)$ is the electron distribution function and $\mathbf{M}(\epsilon,\omega)$ is the matrix element for the optical transition considering a probe energy of $\hbar\omega$. For a small perturbation of the electron distribution function ($f'(\epsilon)$ being the perturbed one), $\Delta R$ is proportional to $\Delta\alpha$ and reads

$$\Delta R \propto \Delta\alpha \propto \int d\epsilon N(\epsilon)N(\epsilon+\omega)|\mathbf{M}(\epsilon,\omega)|^2\left(f'(\epsilon)-f(\epsilon)\right) \tag{4.2}$$

with the integral now taken in the vicinity of the Fermi energy over the width of the optical resonance considered, while the variations of $f(\epsilon)$ at higher energies can be neglected due to fast e-e thermalization (75, 100). This picture of an *excited state absorption* mechanism has been used successfully to explain time-resolved reflectivity signals measured in the visible regions on gold (101, 102) and has been proposed as

a tentative explanation for the angular dependence of the $\Delta R$ signal on YBCO (75). However spectroscopic information was lacking in earlier experiments on HTSC and we can conclude here that this picture is not sufficient to explain the time-resolved spectroscopic data presented in this chapter. The reason being evident from the large discrepancies between the spectroscopic signals in different phases (Figs. 4.2, 4.4, 4.6) and from the absence of distinct features related to interband transitions in the normal state (Fig. 4.2). Thus the experiments suggest that the presence of photoexcitations causes strong modifications of the electronic structure of the material beyond this simple "independent particle" picture and a detailed differential model is needed in which the microscopic, yet phenomenological, parameters of the dielectric function are perturbed.

### 4.3.1 Formulation

In order to interpret the spectral responses reported in the previous section (4.2) it is necessary to formulate a differential model for the dielectric function starting from the well-known static optical properties of cuprates (2.2) and the Extended Drude model (EDM). A $\Delta R/R(\omega, t)$ variation can be defined as

$$\frac{\Delta R}{R}(\omega, t) = \frac{R_{ex}(\omega, t) - R_{eq}(\omega)}{R_{eq}(\omega)} \tag{4.3}$$

with $R_{eq}(\omega)$ being the equilibrium reflectivity and $R_{ex}(\omega, t)$ the time-dependent excited one. According to formula 2.10 the reflectivity is univocally determined by the dielectric function, thus, to calculate $\Delta R(\omega, t)$, a variation of the dielectric function have to be applied and compared to the experimental data.

As a starting point one should look for the temperature dependence of the static dielectric function. It is likely that a similar variation will take place under photo-excitation as well. The temperature dependence of the intraband part is determined implicitly in the conductivity $\sigma(\omega)$ (Eq. 2.6) through the Fermi-Dirac distribution function $f(\omega, T)$ and the single-particle self energy $\Sigma(\omega, T)$. If the boson function $\Pi(\Omega)$ this

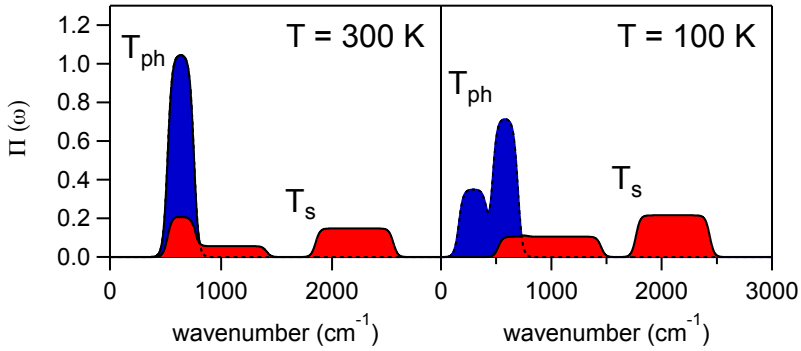


**Figure 4.8: Glue function, temperature dependence** - Glue function calculated from the static optical data reported in section 2.2.2 on the OP96 sample (see Chapter 3) at 100 K and 300 K. Blue and red regions distinguish the part of the memory function assigned to phonons and electronic excitations respectively within the Three-Temperature model (see text).

temperature dependence can be calculated analytically. The boson function is determined by fitting the static optical properties with a simplified histogram model (59). Considering the case of sample OP96, where the temperature dependence of the static optical constants is available, some other parameters produce important variations of $R$ with temperature, namely $\omega_p$, $\Gamma_{imp}$, $\omega_{p0}^2$ and the boson function itself, as shown in Fig. 4.8.

In the energy region from 0.5 eV up to 1.2 eV the reflectivity is dominated by intraband transitions (Drude peak). Thus a differential model for this spectral region should model the photoexcitation of the Drude peak within the EDM. In particular considering that on the timescales shorter than some picoseconds electrons and phonons are decoupled (as suggested by the Two-Temperature model, (81) and the Three-temperature model (83, 84)), we can rewrite the conductivity

(2.6) separating the two temperatures,

$$\sigma(\omega,t) = \frac{\omega_p^2(t)}{i4\pi\omega}\int_{-\infty}^{+\infty} \frac{f(\omega+\epsilon,T_e(t)) - f(\omega,T_e(t))}{\omega - \Sigma(\omega+\epsilon,T_e(t),T_b(t)) + \Sigma^*(\omega,T_e(t),T_b(t)) + i\Gamma_{imp}(t)}d\epsilon \quad (4.4)$$

where $T_e(t)$ and $T_b(t)$ are respectively the electronic and bosonic time-dependent temperatures, $f$ is the Fermi-Dirac distribution function, $\Sigma$ and $\Sigma^*$ are the electrons and holes single-particle self-energies respectively, $\omega_p(t)$ the time-dependent plasma frequency and $\Gamma_{imp}(t)$ the time-dependent impurity scattering. The time-dependent single-particle self-energy can be defined starting from Eq. 2.7, by introducing a time-dependent kernel function,

$$L(\omega,\Omega,T_e(t),T_b(t)) = \\ -2\pi i\left[n(\Omega,T_b(t)) + \frac{1}{2}\right] + \Psi\left(\frac{1}{2} + i\frac{\Omega-\Omega'}{2\pi T_e(t)}\right) - \Psi\left(\frac{1}{2} - i\frac{\Omega+\Omega'}{2\pi T_e(t)}\right) \quad (4.5)$$

where the $T_e$ appears in the Digamma function following the derivation of the equilibrium expression 2.8, where $T$ is referred to the Fermi-Dirac electronic distribution (103).

Within this assumption I can obtain the intraband term of the optical conductivity within a time-dependent EDM. Concerning interband Lorentz oscillators the generalization to time-dependent parameters is straightforward. The model satisfy Kramers-Kronig (KK) relations, since it is calculated as a difference between KK-constrained Lorentz oscillators and the relative variation of the optical conductivity is computed. Thus with this model it is possible to calculate the $\Delta R/R(\omega,t)$ assuming the time-dependence of some microscopic parameters.

In Fig.4.9 I report some results of the differential model applied to the static optical reflectivity data at 300 K on the sample OD86 (see section 2.2.2). Here a modification of the only intraband term is

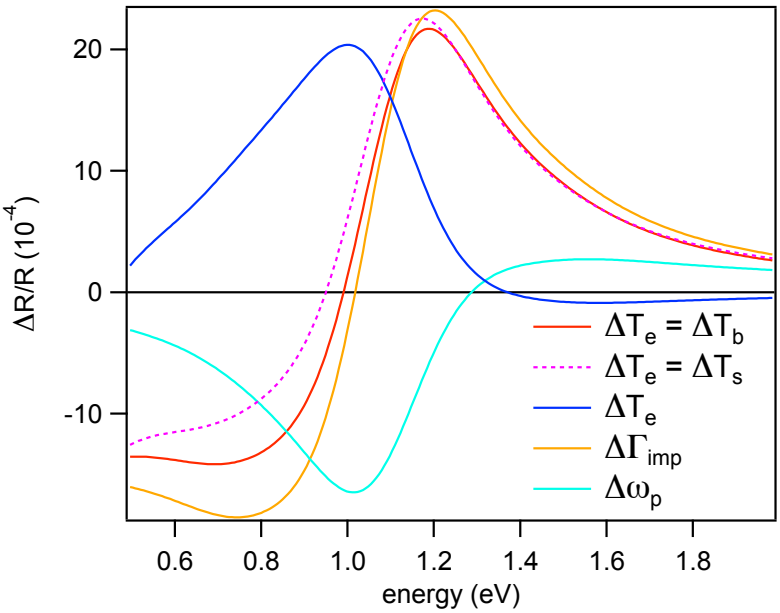


**Figure 4.9: Differential model results** - Simulations of the optical response according to the differential EDM formulated in the text. The variations of each parameter have been made considering a few degrees increase in the temperature dependence obtained from the static reflectivity data of OP96. While $\Delta T$ and $\Delta\Gamma_{imp}$ are positive quantities, $\Delta\omega_p$ is negative. A parameter $\alpha \sim 0.2$ is considered for the Three-Temperature model (see text).

considered. In particular I start with a simple heating model, where $T_e$ and $T_b$ are increased of few degrees above the equilibrium value, but remains in quasi-equilibrium with each other. The change of the explicit $T_e$ and $T_b$ terms in the self energy produces a $\Delta R/R(\omega, t)$ signal which is negative below 1 eV and positive above, with a broad peak around 1.2 eV. The temperature change cause also a change an increase of the impurity scattering and a decrease of the electronic plasma frequency.

If I consider instead a dynamical experiment where the electronic temperature $T_e$ is completely decoupled on the short timescales, as postulated in the Two-Temperature model (81), the transient spectral response would rather be positive in the infrared region, with an intense peak around 1 eV, and negative above 1.4 eV, with a much smaller $\Delta R/R$ signal. This optical response is completely different to what it is

observed experimentally on the short timescales during the pump-probe experiment at room temperature (Fig. 4.2). This is strong evidence of the inadequacy of the Two-Temperature model on the timescale of hundreds of femtoseconds and it means that the bare optical response of electrons is never measured in the time-resolved experiment reported at 300 K.

Following the Three-Temperature model (83, 84) one have to consider the bosonic spectrum as made up of two different subsystems. One of them is composed by spin and high-frequency phonons which are strongly coupled to the electronic system and the other is composed by low-frequency phonons which weakly interact with it. The temperatures of these subsystems can be denoted as $T_s$ and $T_{ph}$ respectively. Within this picture I separate the glue function so that the high-energy plateau is completely included in the $T_s$ part, while the peak at 40 meV is shared between the two subsystems with a coefficient $\alpha$ setting the amount of the peak ascribed to the $T_s$ subsystem (see Fig. 4.8). The $\Delta R/R(\omega, t)$ spectral shape obtained by assuming $T_e$ and $T_s$ in quasi-equilibrium, but at a different temperature from $T_{ph}$ is shown in (Fig. 4.9). Interestingly the curve is very similar to a simple heating model, except for a small redshift of the zero-crossing energy.

In the following I will present the results of fitting the experimental data with the differential model formulated above. Those results are very stable on the choice of the equilibrium dielectric function and depend mainly on the kind of perturbation $\Delta\epsilon(\omega, t)$. The same results are obtained assuming different $\epsilon_{eq}(\omega, t)$ (for example with a different number of interband oscillators, or for example considering a sample with slightly different doping). For this reason, even if the equilibrium dielectric function of sample OD86 is not known precisely and it is extrapolated from the parameters obtained on the OP96 sample (following the procedure outlined in section 2.2.2), this does not constitute a problem for the interpretation of the data and do not alter the conclusion. However, for this reason, I will only discuss the most evident features arising from the optical response data and not the details of the spectral response.

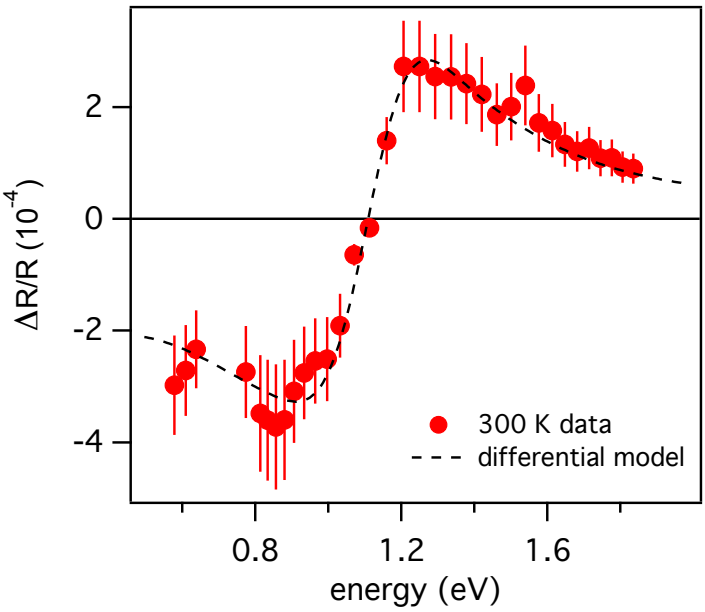


**Figure 4.10: Fit of the 300 K data with the differential model** - Principal component of the optical response at 300 K and the corresponding fit obtained with the differential EDM (see text). In the model, $T_e$ and $T_s$ are in quasi-equilibrium and the plasma frequency is slightly decreased according to its temperature dependence.

### 4.3.2 Normal state

The experimental principal component measured at 300 K in sample OD86 can be easily reproduced by an increase of $T_e$ and $T_s$ of few degrees (see Fig. 4.10 and the corresponding fit parameters in Table 4.1) The fact that the shape of the optical response is better reproduced by a variation of both $T_e(t)$ and $T_s(t)$ rather than a variation of the only $T_e(t)$ suggests that some part of the bosonic spectrum is at equilibrium with electrons already within the first hundred of femtoseconds. This can be the case for example of electronic spin excitations, constituting the broad high-energy plateau in the "glue function" (Fig. 4.8). The subsequent exponential relaxation would then represent the fastest between the boson-phonon relaxation process and the direct electron-phonon coupling.

**Table 4.1: Parameters of the differential model at 300 K-** Dielectric function parameters at equilibrium and out-of-equilibrium used in the fit of Fig. 4.10.

| parameters | equilibrium | non-equilibrium |
|---|---|---|
| $\omega_p\,(cm^{-1})$ | 17389 | 17389 |
| $\Gamma_{imp}\,(cm^{-1})$ | 625 | 625 |
| $T_e\,(K)$ | 300 | 306 |
| $T_b\,(K)$ | 300 | 306 |
| $T_{ph}\,(K)$ | 300 | 300 |

It is important to notice that the variation of the plasma frequency $\omega_p$ here follows the temperature dependence observed in the static data, i.e., a decrease with increasing temperature (23).

### 4.3.3 Pseudogap phase

While the quasi-equilibrium response (after 3-4 ps) in the pseudo-gap phase exhibits the same characteristic of the normal state, the fast $\Delta R/R(\omega, t)$ signal has completely different shape and as I will show a completely different nature. In facts, to reproduce the positive signal around 1-1.2 eV it is necessary to include a photoinduced increase of the Drude plasma frequency $\omega_p$.

The experimental spectral response could be possibly reproduced also by an increase of the electronic temperature $T_e$ completely decoupled by both spin and phonons excitations (see Fig. 4.9). However this hypothesis can be excluded by considering the dynamics of the zero crossing energy, i.e., the energy at which the $\Delta R/R$ is zero, in the infrared spectral region. This dynamics is shown in Fig. 4.11 and has a slow dynamics ($\sim$ 2.3 ps) toward the quasi-equilibrium spectral response. This means that the spectral response changes shape on this timescale. On the contrary the $\Delta R/R$ has a faster relaxation time ($\sim$ 0.6 ps) as shown in Fig. 4.5. This means that the system relaxes on a timescale faster than the evolution of the spectral response toward

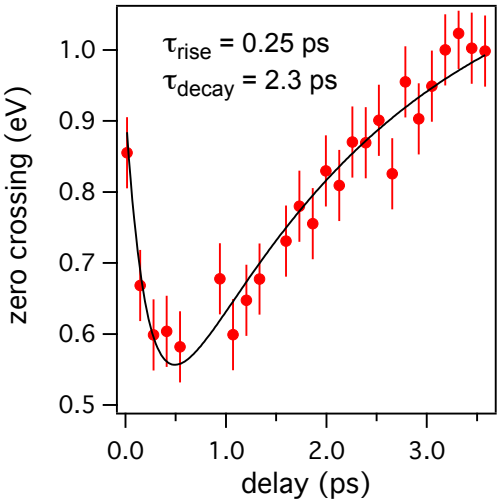


**Figure 4.11: Zero crossing energy as a function of time, 100 K** - Energies at which the $\Delta R/R$ signal at 100 K (Fig. 4.4) in the infrared spectral region is zero. This energy has been calculated with a polynomial fit of the $\Delta R/R(\omega)$ traces between 0.5 and 1.3 eV at each instant of time. The dynamics of the zero crossing energy can be fitted with an exponential function with a rise time, $\tau_{rise}$, and a decay time $\tau_{decay}$, with the values shown in the graph.

quasi-equilibrium. Therefore the spectral response cannot be a signal originated by decoupled electrons. The case is probably the same to the normal state 4.3.2, where the Drude electronic response can be approximated with a simple heating, with a small redshift. Thus in the following I will consider the electrons, $T_e$, and strongly coupled bosons, $T_s$, always in quasi-equilibrium.

In Fig. 4.12 I report two different approaches to reproduce the experimental data. The corresponding fit parameters are reported in Table 4.2. In both models $\omega_p$ is set as free parameter, together with the spectral weight of mid-infrared oscillators in the case of fit A, and with the low-energy peak of the boson function (Fig. 4.8) for fit B. Both fits are not perfectly reproducing the experimental data, but they are following the correct trend. In both cases $\omega_p$ is increasing, and this effect is found even when other parameters are considered for the differential fit here. Thus I can conclude here that, even if a precise differential

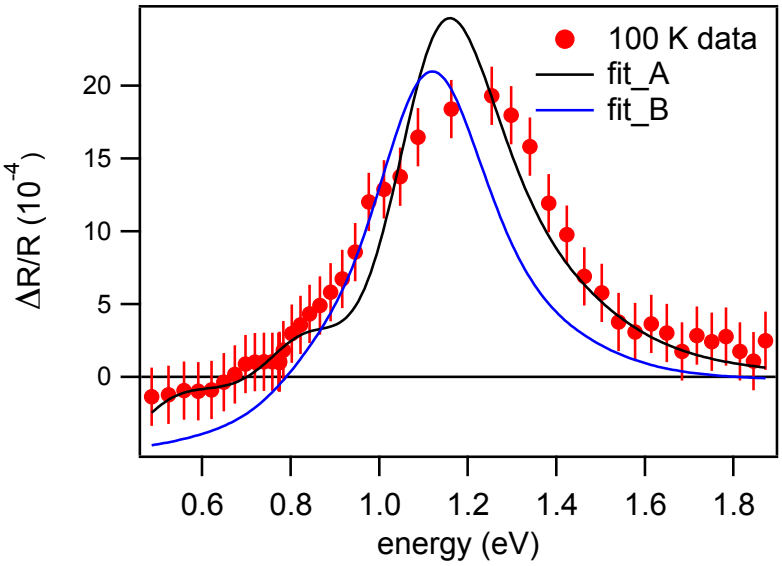


**Figure 4.12: Fit of the 100 K data with the differential model** - Principal component of the optical response at 100 K and the corresponding fit obtained with the differential EDM (see text). In fit A the spectral weight of the Drude term and of mid-infrared peaks are used as free parameters. In fit B the spectral weight of the Drude term and the low-energy peak of the glue function are used as free parameters.

model of the pseudogap response is not obtained, the spectral feature centered at 1.1 eV has his main origin in a Drude spectral weight increase.

Such spectral weight increase can be related to a photoinduced charge carriers kinetic energy decrease through the formula

$$SW_{intra} = -\frac{\pi e^2 a^2}{2\hbar^2 V} E_{kin} \tag{4.6}$$

which can be derived in the special case of a single conduction band within the nearest-neighbor tight-binding model (104, 105). This trend is exactly opposite to the temperature dependence of equilibrium optical properties (see Section 2.2.2), where instead the $\omega_p \propto -T^2$ dependence due to thermal excitations of the free carriers (23) is dominating.

**Table 4.2: Parameters of the differential models at 100 K-** Dielectric function parameters at equilibrium and out-of-equilibrium used in fit A and fit B of Fig. 4.12.

| parameters | equilibrium | non-equilibrium(A) | non-equilibrium(B) |
|---|---|---|---|
| $\omega_p\,(cm^{-1})$ | 17392.2 | 17406.6 | 17395.6 |
| $\Gamma_{imp}\,(cm^{-1})$ | 155.142 | 155.142 | 155.142 |
| $T_e\,(K)$ | 100 | 114 | 110 |
| $T_b\,(K)$ | 100 | 114 | 110 |
| $T_{ph}\,(K)$ | 100 | 100 | 100 |
| $\omega_0\,(cm^{-1})$ | 4929 | 4929 | 4929 |
| $\omega_{p0}^2\,(cm^{-2})$ | 1.387x$10^7$ | 1.361x$10^7$ | 1.387x$10^7$ |
| $\omega_1\,(cm^{-1})$ | 6959 | 6959 | 6959 |
| $\omega_{p1}^2\,(cm^{-2})$ | 6.489x$10^6$ | 6.449x$10^6$ | 6.489x$10^6$ |

This photoinduced effect can be interpreted as the impulsive closing of the pseudogap, causing the decrease of the electronic kinetic energy before any thermal effect takes place. This result is also in agreement with the general statement that the pseudogap consists of an effective spectral weight suppression of the density of states near the Fermi level $E_F$.

I remark that the effect reported in this section cannot be observed in quasi-equilibrium conditions because the thermal broadening of the Drude peak is more intense than the corresponding thermally induced closing of the pseudogap. In facts, thermal-difference reflectance studies in the pseudogap state did not show any evidence of spectral weight transfer (99).

### 4.3.4 Superconducting state

As discussed in chapter 2.1.1, in cuprates the interplay between the Cu-3$d$ and the O-2$p$ states determines both the electronic structure close to the Fermi level as well as the high-energy properties related to the formation of the Zhang-Rice singlet (43) (hole shared among the four

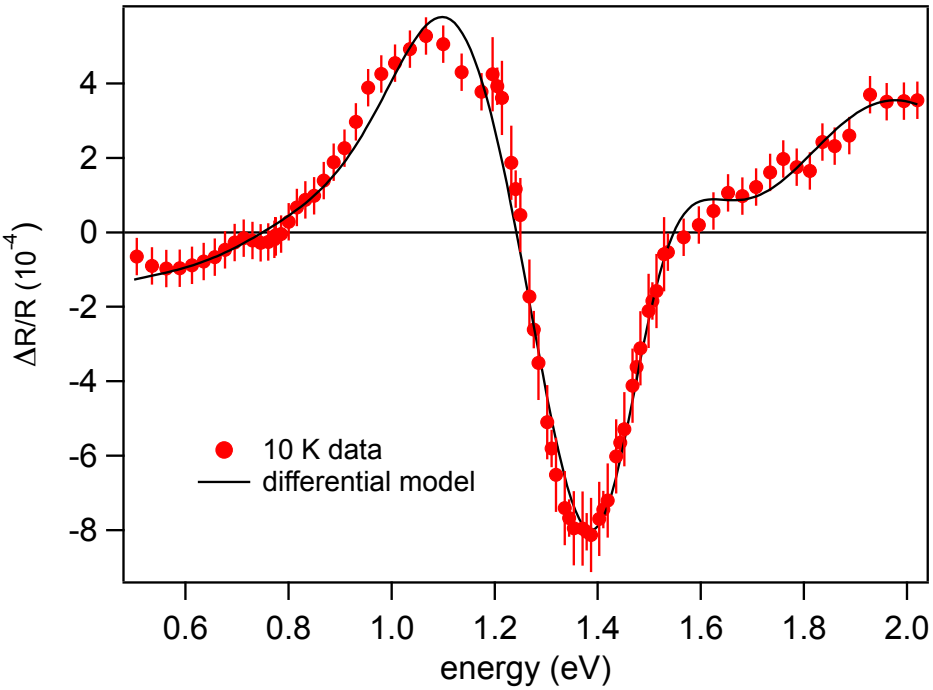


**Figure 4.13: Fit of the 10 K data with the differential model** - Principal component of the optical response at 10 K and the corresponding fit obtained with the differential EDM (see text).The black curves represent the best fit lines to the data assuming a transient modification of the 1.5 eV and 2 eV interband oscillators.

oxygen sites surrounding a Cu and antiferromagnetically coupled to the Cu spin; energy $E_{ZR} \sim 0.5$ eV) and to the charge-transfer processes (42) ($\Delta_{CT}$ ~2 eV). An important and unsolved issue in the physics of HTSC is the role of these electronic many-body excitations in the superconducting condensate formation. Solving this problem would set the benchmark for unconventional models of HTSC, at variance with the BCS theory for conventional superconductivity, where the opening of the superconducting gap induces a significant rearrangement of the quasiparticle excitation spectrum over an energy range of few time $2\Delta_{SC}$ (22).

With the time-resolved spectroscopic technique developed in this

**Table 4.3: Parameters of the differential models at 10 K-** Dielectric function parameters at equilibrium and out-of-equilibrium used in Fig. 4.13.

| parameters | equilibrium | non-equilibrium |
|---|---|---|
| $\omega_p\,(cm^{-1})$ | 17920 | 17921 |
| $\Gamma_{imp}\,(cm^{-1})$ | 53 | 53 |
| $T_e\,(K)$ | 10 | 36 |
| $T_b\,(K)$ | 10 | 36 |
| $T_{ph}\,(K)$ | 10 | 10 |
| $\omega_2\,(cm^{-1})$ | 11800 | 11800 |
| $\omega_{p2}^2\,(cm^{-2})$ | 5.72x$10^6$ | 5.81x$10^6$ |
| $\omega_3\,(cm^{-1})$ | 16163 | 16163 |
| $\omega_{p3}^2\,(cm^{-2})$ | 4.194x$10^7$ | 4.177x$10^7$ |

thesis it is finally possible to address this problem by measuring the non-equilibrium optical properties with high resolution ($\Delta R/R \sim 10^{-4}$) when the system become superconducting. In facts, in the superconducting state (Fig. 4.6) the optical response in the 1.2-2 eV spectral region changes drastically if compared to any measurement done above $T_C$ and the signal cannot be reproduced by variations of the only intraband conductivity term. In particular a perturbation of the interband oscillators at 1.5 and 2.0 eV is the only way to reproduce the sharp dip in the spectral response centered at 1.4 eV (Fig. 4.13, see Table 4.3 for the fit parameters of the model). The fit reveals that the interband spectral weight variation ($\Delta SW_{tot} = \Delta\omega_{p2}^2/8 + \Delta\omega_{p3}^2/8$, with $\Delta\omega_{p2}^2/8$ and $\Delta\omega_{p3}^2/8$ being the plasma frequencies of the 1.5 eV and 2.0 eV oscillators respectively) is negative. Thus the total spectral weight of these oscillator decreases under photoexcitation and this variation accounts for most of the spectral weight increase in the intraband part on the same timescale, demonstrating the dynamical transfer of spectral weight between these two energy ranges.

Such a spectral weight transfer can be related to a photoinduced charge carriers kinetic energy decrease through the formula 4.6 dis-

cussed in the previous section. A kinetic energy lowering is compatible with a photoinduced superconducting gap closing in the BCS model, where the energy gain is driven by potential energy and the kinetic energy is effectively higher in the superconducting state (22). The situation is similar to the one described in the pseudogap state 4.3.3 with the main difference that below $T_C$ the spectral weight removed from the condensate and transferred at high energy is detectable and localized mainly on two interband oscillators (1.5 eV and 2.0 eV).

An interesting aspect is that the sign of the spectral weight transferred to these oscillators changes abruptly in the underdoped side of the phase diagram, where instead a positive variation of the interband spectral weight is measured with this technique. This would mean that superconductivity is accompanied by a gain in kinetic energy (rather than a potential energy gain) on that side of the phase diagram, with a sign change in the kinetic energy gain at optimal doping (106). However I will not discuss this point in detail since in this thesis I focus only on the experimental data obtained on overdoped samples.

The most important finding here is that at variance with the simple energy-gap model of conventional superconductors, where small changes of the interband transitions, over a narrow frequency range ($\frac{\Delta}{\hbar}$) can arise from the opening of the superconducting gap at the Fermi level, these measurements clearly shows a photoinduced change of $R(\omega, t)$ over a spectral range ($\sim$ 1 eV), significantly broader than the superconducting energy scale ($\sim$ 40 meV) (21). This result reveals a dramatic superconductivity-induced rearrangement of the mixed Cu-O electronic states at 1.5 eV and 2 eV binding energy (see section 2.2.2), suggesting the important role superconductivity of those electronic many-body excitations in the unconventional high-temperature superconductivity.

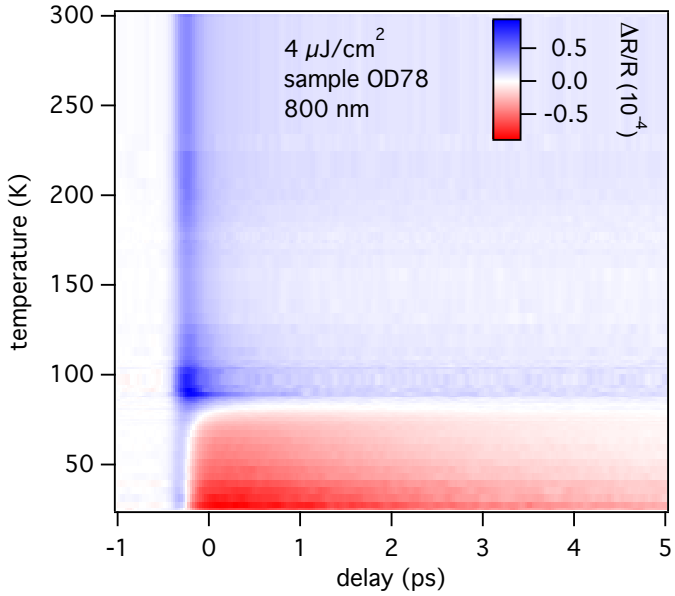


**Figure 4.14: Temperature dependence of the interband spectral weight** - Temperature-time matrix of the $\Delta R/R$ signal on the OD78 sample at 1.55 eV at a pump fluence of 4 $\mu J/cm^2$

## 4.4 Quasi-particles dynamics across the thermally driven superconducting phase transition

In this section I focus on the dynamics of the spectral weight transfer in the interband spectral region of an overdoped sample (OD78) as a function of temperature. The sample considered here is more overdoped than in previous sections in order to have a minor role of the pseudogap. Moreover, this choice gives a more solid foundation to the applicability of conventional non-equilibrium models, such as the Rothwarf-Taylor (RT) model (64), to interpret the QPs dynamics. In the previous section I showed that the negative signal around 1.5 eV can be interpreted as a kinetic energy lowering due to superconducting gap suppression. This is confirmed by the close relationship of the peak with the superconducting condensate observed from a study of the temperature

dependence of this signal, as shown in Fig. 4.14. This finding suggest that the dynamics of the $\Delta R/R$ at 1.5 eV coincide with the condensate reformation dynamics and it is connected to the photoexcited QPs relaxation process via CPs reformation.

The positive signal above $T_C$ can be reproduced by a single exponential decay function, $Ae^{-t/\tau_A}$, convoluted with the time shape of the laser pulse, describing the relaxation of hot electrons via electron-phonon interaction (80, 81, 82) with a relaxation time $\tau_A$ of about 440 fs. In agreement with the literature (100), no $\Delta$R/R sign change associated with the pseudogap phase is observed when probing at 800 nm wavelength on the overdoped sample, at variance with optimally and underdoped samples (79).

In figure 4.15 I plot the raw ($\Delta$R/R) data of consecutive series of scans taken at 1.5 eV from 95 K down to 38 K at low pump fluence ($\sim$4 $\mu$J/cm$^2$). The positive and fast signal survives also below $T_C$, superimposed to a negative signal, which I will denote as the superconducting signal (SCS), assumed to be proportional to the photoexcited QP density and that we capture with a single exponential function. The sum of these two functions, $Ae^{-t/\tau_A} + Be^{-t/\tau_B}$, is sufficient to reproduce all the experimental curves as shown in figure 4.15. The relevant fit parameters of the SCS, i.e., the amplitude $B$ and the decay time $\tau_B$, are plotted in the inset.

The decay time of the SCS, $\tau_B$, is shown, as a function of temperature, in the inset of figure4.15 (red circles). Starting from 38 K the decay time decreases with temperature, reaching a minimum at 62 K of 3.3 ps. Above this temperature it rapidly increases reaching the value of 4.7 ps at $T_C$. At this temperature the order parameter vanishes ($\Delta \to 0$), the SCS amplitude, $B$, is much smaller than $A$ (the normal-state signal), and the uncertainty on the determination of its decay time strongly increases.

The increase in the decay time in the vicinity of $T_C$ is in agreement with previous observations for other HTSC in the low-fluence regime (65, 72, 75, 78) and it has been interpreted as the manifestation of a $\propto 1/\Delta$ divergence predicted by several theoretical calculations for BCS superconductors (72, 107, 108). Experimentally, this divergence is

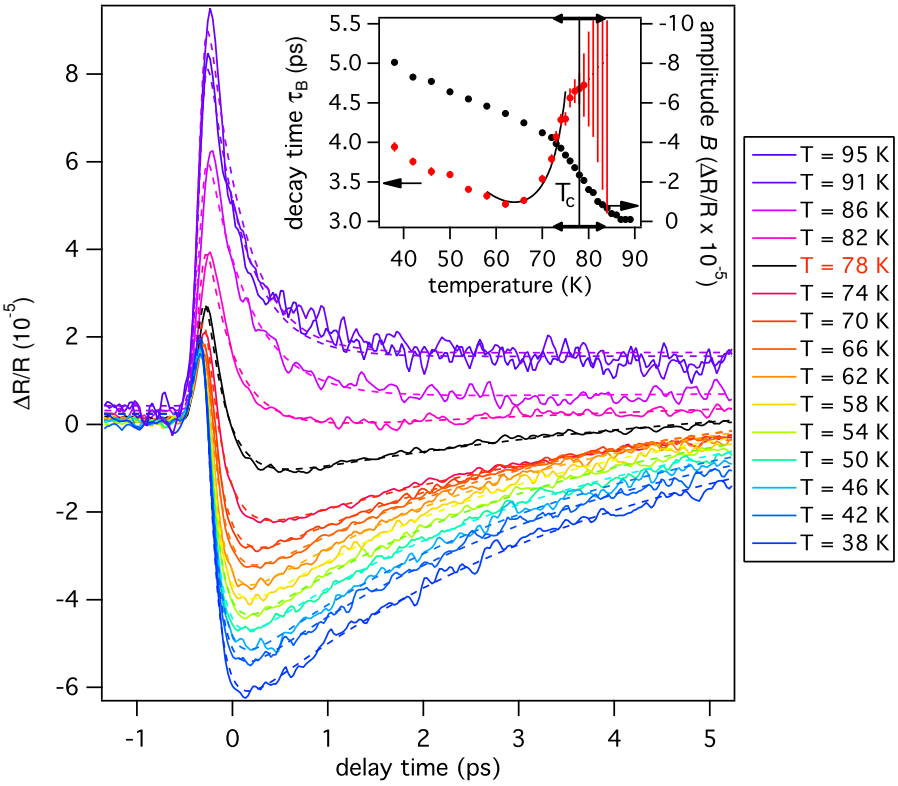


**Figure 4.15: Superconducting-to-normal thermally-driven phase transition in overdoped Bi2212** - $\Delta R/R$ signal (solid lines) as a function of delay time at different temperatures (from 95 K to 38 K) on Y-Bi2212 overdoped single crystal. The dashed lines are the fits to the experimental curves (see the fitting function in the text). The black line represents the $\Delta R/R$ trace at $T_C$. In the inset we report the fit parameters of the SCS, i.e., decay time, $\tau_B$ (red circles), and amplitude, $B$ (black circles). The error bars obtained from the fit procedure are displayed for all the data. The high uncertainty on the decay time above $T_C$ led us to plot just the error bar and not the data point. The black arrow on the temperature axis of the inset shows the superconducting transition amplitude of the sample.

smeared out because of the finite superconducting transition amplitude. However, from the analysis of the SCS decay time increase just below $T_C$, I can extract quantitative information about the superconducting gap.

A very useful model to interpret the non-equilibrium dynamics of su-

perconductors in the low-intensity regime is the Rothwarf-Taylor (RT) model (64, 65, 70) (See Appendix). In this model, two QPs recombine to form a Cooper pair emitting a boson with energy larger then $2\Delta$. As the reverse process is also allowed, the QP and the boson populations are in quasi-equilibrium and the actual relaxation is determined by inelastic processes. Within this model, one can write down a set of coupled rate equations, which have analytic solutions in two very important limiting cases, the weak and the strong bottleneck regimes (64, 65). In the first case, the boson inelastic decay rate is fast and the relaxation dynamics is equivalent to simple bi-molecular dynamics (71, 77). In the second regime, namely the strong bottleneck one, the inelastic decay of the boson population strongly slows down the relaxation process. For a given superconductor, the dynamical regime is determined by the particular type of bosons considered in this dynamics. However, in both regimes and far enough from the critical temperature (109), a very simple formula for the QP decay rate $\gamma$ is valid

$$\gamma(T, \Delta(n_{ph}), n_{ph}) = (n_{ph} + n_T)\Gamma(T, \Delta(n_{ph})) \tag{4.7}$$

where $n_T$ are the thermal QPs, $n_{ph}$ are the photo-injected ones and $\Gamma(T, \Delta)$ is a function of the microscopic probabilities for the scattering events involving QPs and bosons (65). Given the QP population densities, $n_{ph}$ and $n_T$, one can extract from the experimental QP decay rate $\gamma$ the $\Gamma(T, \Delta)$ function in the low-excitation limit. We stress that the use of this formula does not imply any assumption on the particular boson involved in the non-equilibrium dynamics.

Here I use the well-known result obtained by Kabanov et al. (72) that, for a d-wave superconductor with a 2D Fermi surface with nodes and for temperatures $k_B T << \Delta \sim 5 k_B T_C$ ((21)), the QP population at thermal equilibrium, $n_T$, has the form

$$n_T = 1.64 N(0)(k_B T)^2/\Delta \tag{4.8}$$

where N(0) is the density of states at the Fermi level and $\Delta$ is the gap value at equilibrium. The temperature dependence of $n_T$ obtained

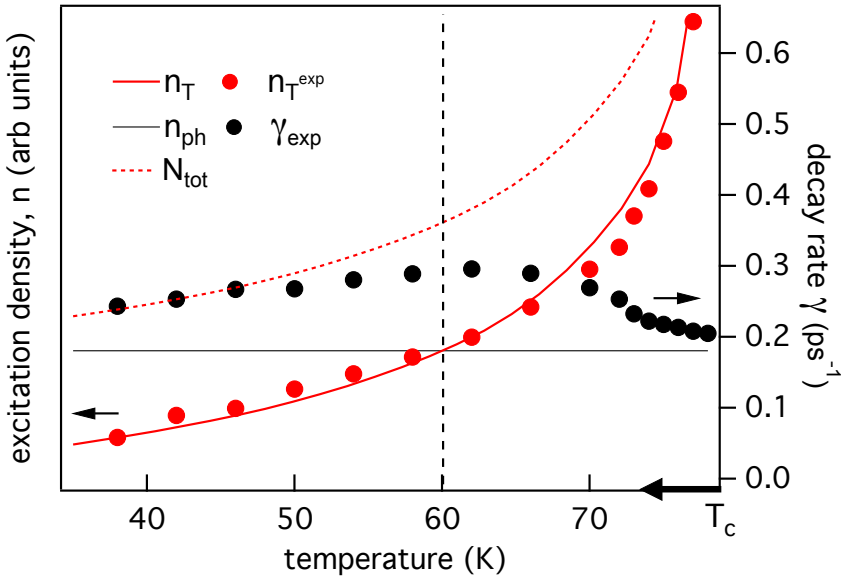


**Figure 4.16: Temperature dependence of thermal quasi-particles** - Excitation density of both thermal and photoinduced QP, respectively $n_T$ and $n_{ph}$ (solid lines), and their sum $N_{tot}$ (dashed line) as a function of temperature. For the thermal QP we assumed (4.8) and a d-wave like $\Delta(T)$ dependence and we compared the predicted value with the one obtained through (4.9) from the experimental $B(T)$ amplitude (inset of figure 4.15). On the right axis we report the experimental decay rate obtained from the fit in figure 4.15.

from (4.8) is plotted in figure 4.17a. To validate (4.8), I estimate $n_T$ from the temperature dependence of the $B$ amplitude (inset of figure 4.15) through the formula (65)

$$B(T) \propto \frac{2N_{ph} + n_{ph}}{\sqrt{1 + 16n_T^2 + 8n_T}} \tag{4.9}$$

where $N_{ph}$ is the photoexcited boson population density and we assume, similarly to (65, 78), the total population density $(n_{ph} + 2N_{ph})$ to be constant in temperature since the pump fluence is constant. The $B(T)$ amplitude in the low-temperature limit is measured at T = 10 K. Good agreement is found between $n_T$ predicted by (4.8) and the value

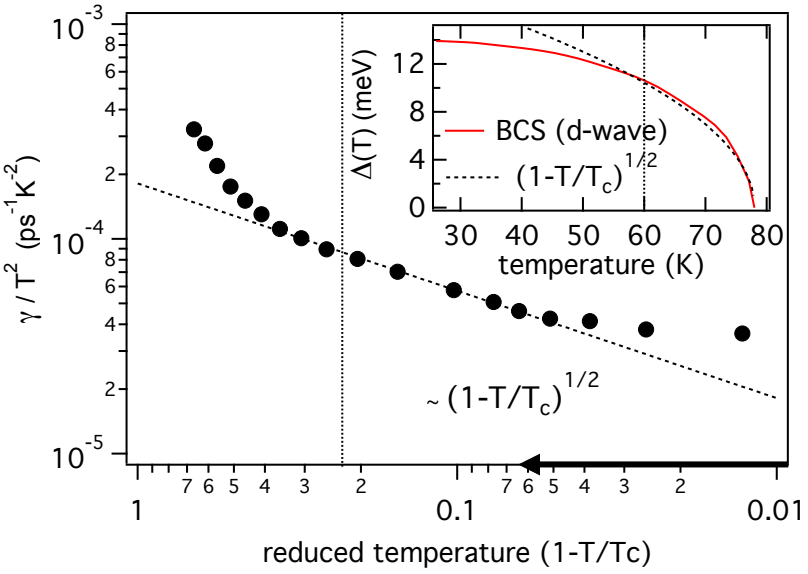


**Figure 4.17: Power-law divergence of QP decay rate** - $\gamma/T^2$ as a function of the reduced temperature in a double-logarithmic plot. The long-dashed line represents the $(1-T/T_C)^{1/2}$ power-law dependence. In the inset we show the result of the numerical integration of the d-wave BCS gap equation as a function of temperature compared to the $(1-T/T_C)^{1/2}$ dependence (22). In all the panels the vertical short-dashed divide the low from the high temperature regime (see text). The error bars are within the black circles size.

obtained from the experimental data through (4.9) (figure 4.17a). Thus in the following we will use the value of $n_T$ calculated through (4.8).

In figure 4.17a the experimental SCS decay rate $\gamma$ and the total QP density, $N_{tot}$=$n_{ph}$+$n_T$, are compared. The contribution due to $n_{ph}$ is estimated in the low-temperature limit (110).

In the high-temperature limit I observe that: i) the thermal population $n_T$ is dominating on $n_{ph}$; ii) $\gamma_{exp}$ is not following the $N_{tot}$ temperature dependence. This finding suggests that the decay time increase observed close to $T_C$ is related to a decrease of $\Gamma(T,\Delta)$. Here I set the separation between the high- and low-temperature regimes at 60 K, i.e, when $n_T > n_{ph}$. The conclusions are independent of the particular choice of this temperature.

I can now verify that the increase in decay time when approaching

$T_C$ is related to a real divergence arising from the fact that $\Gamma(T, \Delta) \to 0$ when $\Delta \to 0$ and we find the power-law that controls this divergence. In figure 4.17b, we plot the quantity $\gamma_{exp}/T^2$ as a function of the reduced temperature (distance from the critical temperature) on a double-logarithmic scale. Using Eqs. (4.7) and (4.8), I find that this quantity is proportional to

$$\frac{\gamma}{T^2} \propto \frac{\Gamma(T, \Delta)}{\Delta} \tag{4.10}$$

in the temperature region where $n_T$ is the dominant term in the QP density, i.e., above 60 K.

In this region, I notice a power-law dependence,

$$\frac{\Gamma(T, \Delta)}{\Delta} \propto (1 - T/T_C)^{\tilde{\beta}} \tag{4.11}$$

with an exponent $\tilde{\beta} \sim 1/2$ (solid line in figure 4.17b), which is the same mean-field critical exponent expected for the order parameter $\Delta$ in a BCS superconductor. In a d-wave superconductor with $T_C$ of 78 K, the superconducting gap dependence is well approximated by $\Delta \propto (1 - T/T_C)^{1/2}$, in the temperature range from 60 to 78 K (see the inset in figure 4.17b). This assumption is still a good approximation in the case of overdoped HTSC (49, 111, 112) as long as the critical region (reduced temperature $\ll 0.1$) is not entered (113, 114, 115). In facts, a deviation from this exponent is found 3-4 K below $T_C$ (Fig. 4.17). Here the transition width (see Chap. 3) as well as the effect of critical fluctuations (113, 114, 115) may play a role. I also remark that Eq. 4.7 is not applicable in the close vicinity of $T_C$ (109).

Neglecting the deviation in this small temperature region and within the approximate analytic solution (4.7) (109), we can easily derive the power-law dependence of the $\Gamma(T, \Delta)$ function in the RT approach :

$$\Gamma(T, \Delta) \propto (1 - T/T_C)^{\alpha} \propto \Delta^{2\alpha} \tag{4.12}$$

with $\alpha \sim 1$. This power-law dependence can hardly be derived by first-principles, particularly if the nature of boson involved in the pairing mechanism is unknown.

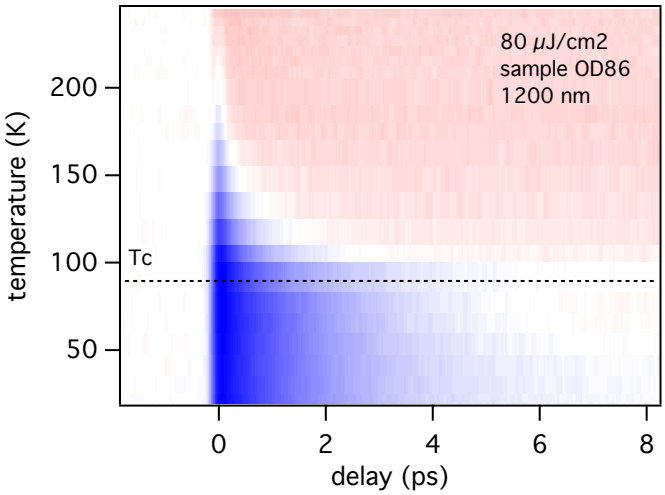


**Figure 4.18: Temperature dependence of the intraband spectral weight** - Temperature-time matrix of the $\Delta R/R$ signal on the OD86 sample at 1.0 eV at a pump fluence of 80 $\mu J/cm^2$

## 4.5 Temperature dependence of intraband spectral weight transfer

While in the previous section I have demonstrated i) the connection between the interband spectral weight and the superconducting condensate and ii) the relationship between the slow decay relaxation and the superconducting gap vanishing at $T_C$, here I focus on the origin of the intraband spectral weight transfer observed as a positive peak in the 1-1.2 eV spectral region. This spectral feature is interpreted as a photoinduced increase of the Drude spectral weight. This phenomenon is observed at temperatures as high as 100 K in the OD86 sample and it is probably accompanied by other spectral modifications (section 4.3.3).

In Fig. 4.18 I report the temperature dependence of the $\Delta R/R(t)$ signal at 1200 nm ($\sim$ 1 eV) and at a pump fluence of 80 $\mu J/cm^2$. The positive intraband spectral weight transfer appears above $T_C$, at temperatures of the order of 200 K and reaches a maximum value at T* ($\sim$ 130 K on this sample). Surprisingly this spectral feature merges

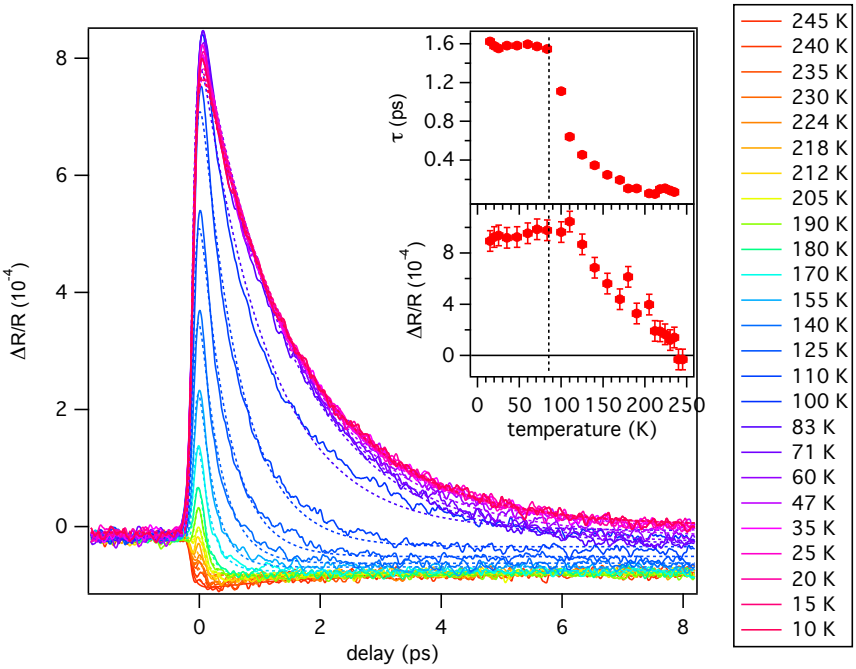


**Figure 4.19: Dynamics of the intraband spectral weight versus temperature** - Temperature dependent measurements at 1.0 eV on the OD86 sample at a pump fluence of 80 $\mu J/cm^2$. The insets shows the intensity and decay time obtained with a fit with a single exponential decay.

smoothly into the superconducting spectral response, with a drastic increase in the decay time in the vicinity of $T_C$, while below $T_C$ no substantial temperature dependence is observed.

The $\Delta R/R(t)$ traces at all the temperatures are reported in Fig. 4.19 together with the corresponding fit to a single exponential function. The decay time increase is gradual when approaching $T_C$ from above and become very steep around 100 K. The spectral weight transferred is constant below $T_C$, while it decrease above $T_C$ with a linear dependence. The result of a constant spectral weight transferred in the superconducting state is not caused by saturation effects. In facts, as it will be shown later on the saturation of this signal at 1200 nm is observed at fluences $> 200\ \mu J/cm^2$ and with typical $\Delta R/R \sim$ 2-3 $\times\ 10^{-3}$. The temperature dependence of the spectral weight removed from the

condensate is connected to the results shown in the inset of Fig.4.15. Thus the intensity of the spectral weight transferred in the intraband region is insensitive to the condensate formation and it rather reaches a plateau at T* ($\sim$ 130 K in this sample). Below this temperature the dynamics exhibit a drastic slowing down, which become at $T_C$ the same QPs dynamics involved in CPs recombination.

This would be in agreement with a picture of preformed pairs in a narrow ($\sim$ 20 K) temperature region above $T_C$. Moreover, starting from the interpretation of this spectral feature given in section 4.3.3, an increase of the Drude spectral weight can be connected to a photoinduced decrease of electron kinetic energy and thus to a pairing gap closing.

However more detailed temperature dependent measurements on this feature have to be done, especially at lower fluence, to clarify the origin of the change of behavior of the intraband spectral weight at $T_C$ and at T*.

## 4.6 Conclusion

In this chapter I reported a series of experiments on overdoped HTSC samples in the low-excitation regime at several temperatures. The optical response in the normal state is interpreted within a Three-Temperature model. In pseudogap and superconducting state the spectral weight exhibits anomalous rearrangement at energy scales ($\sim$ 1 eV) much higher than the superconducting gap ($\sim$ 40 meV). The analysis of the interband spectral weight transfer gives an intensity proportional to the superconducting condensate photoinduced depletion, suggesting a crucial role of Cu-O mixed many body excitations at 1.5 eV and 2.0 eV.

QPs dynamics in the superconducting state is found to obey the RT model as in conventional BCS superconductors, with a decay rate proportional to a power-law of the superconducting gap. The pseudogap QPs relaxation dynamics is faster, but shows a gradual slowing down while approaching $T_C$ from above.

# Chapter 5

# Evidence of a non-thermal superconducting-to-normal-state photoinduced phase transition

## 5.1 Introduction

The possibility of inducing an electronic non-thermal phase transition in high-temperature superconductors (HTSC), by means of ultra-short laser pulses, will set a new path for studying the origin of the superconductivity in these materials. In facts, under such non-equilibrium conditions, the homogeneous superconducting phase becomes unstable as its free energy increases during the pulse duration (29, 34, 35), while the superconducting order parameter can coexist with the pseudogap or the normal-state.

For many years the exploration of the physics of this process has been a difficult task because of experimental limitations, mainly arising

from laser induced heating of the samples (27, 73, 74, 76). Only recent all-optical pump-probe experiments on underdoped and optimally doped HTSC (28, 29, 30) have achieved control of the impulsive vaporization of the superconducting condensate in the high-intensity regime. This phenomenon has been observed as the saturation of the transient reflectivity variation ($\Delta$R/R) signal associated with the superconducting phase (28, 29), in contrast to its linear fluence dependence in the low intensity regime (65, 71, 72, 75, 76, 77).

A similar photoinduced phase transition (PIPT) to the metallic phase has been recently reported on charge-density-wave (31, 32) (CDW) and spin-density wave (33) (SDW) compounds. While in such systems the PIPT exhibits quasi-thermal character, as it is accompanied by the same critical slowing down observed in quasi-equilibrium conditions at $T_C$ (31, 32, 33), the origin of the PIPT in HTSC remains unclear. A picture of the photoinduced non-equilibrium state is still lacking due to intrinsic difficulties to disentangle pseudogap and normal-phase signals in optimally and underdoped samples (29, 30), the fingerprint of the pseudogap phase being the $\Delta$R/R sign change observed above $T_C$ in pump-probe experiments when probing at 800 nm wavelength (79).

In this chapter I report pump-probe optical reflectivity measurements at 800 nm in the high-excitation regime on an overdoped $Bi_2Sr_2Ca_{0.92}Y_{0.08}Cu_2O_{8+\delta}$ (Y-Bi2212) single crystal ($T_C$=78 K, OD78 sample). At this doping regime the underlying normal phase is Fermi-liquid-like (9) and no $\Delta$R/R sign change above $T_C$ is measured, at variance with optimally and underdoped samples (100). These characteristics are fundamental to quantitatively interpret the data within a Rothwarf-Taylor (RT) model with time-dependent parameters.

Here I show the lack of the quasiparticles decay time increase at the fluence required to photoinduce the transition, at variance with previously reported PIPTs on CDW (31, 32) and SDW (33) systems and in contrast to the decay time divergence observed at $T_C$ on cuprates (65, 72, 75). This finding demonstrates the non-thermal character of the superconducting-to-normal-state PIPT, opening the question on the nature of this phase transition. To address this question I develop a time-dependent RT model. On the base of this model the hypothesis of

a first-order phase transition, previously predicted by non-equilibrium superconductivity models (29, 34, 35) seems to be favored. However, this interpretation is based on the fundamental assumption that the time-dependent RT model does not abruptly break down in the high-excitation regime on the short timescales (t $<$ 1 ps), therefore leaving open the possibility of a non-thermal second-order phase transition where the quasi-equilibrium bottleneck effect is avoided.

The results presented in this chapter represent a landmark for the growing field of pump-probe techniques, which have been recently extended to the use of several probes, such as Raman scattering (116), electron-diffraction (84), angle-resolved photo emission (83) and broad-band optical spectroscopy (117). All these techniques require an intense ultrashort pump laser pulse, ranging from 0.5 to several mJ/cm$^2$ ((83) and (84) respectively), to obtain reliable results. This chapter tackle the long-standing question on the effect of a pump laser pulse at high fluence on the superconducting condensate of HTSC.

In section 5.2 I discuss the dynamics as a function of fluence at a fixed temperature (10 K) well below T$_C$. Above a threshold pump fluence, the reflectivity variation deviates from the linear dependence and exhibits a saturation in agreement with previous experiments (28, 29, 30). This discontinuity is identified with the condensate vaporization in the whole probed volume (28). I observe the absence of a decay time divergence above this threshold point at variance with the quasi-thermal case (section 4.4) and with experimental observations of PIPT on CDW (31, 32) and SDW (33) compounds.

To interpret the data in the high-fluence regime I take into account dynamical variations of the non-equilibrium superconducting gap, thus extending the RT model to the time-dependent case (section 5.3). In section 5.4 I present the experimental data within the analytical results of the RT model. A linear decrease of the non-equilibrium gap with pump fluence is obtained and a finite non-equilibrium superconducting gap after about 1 ps after the pump pulse that causes the PIPT is measured.

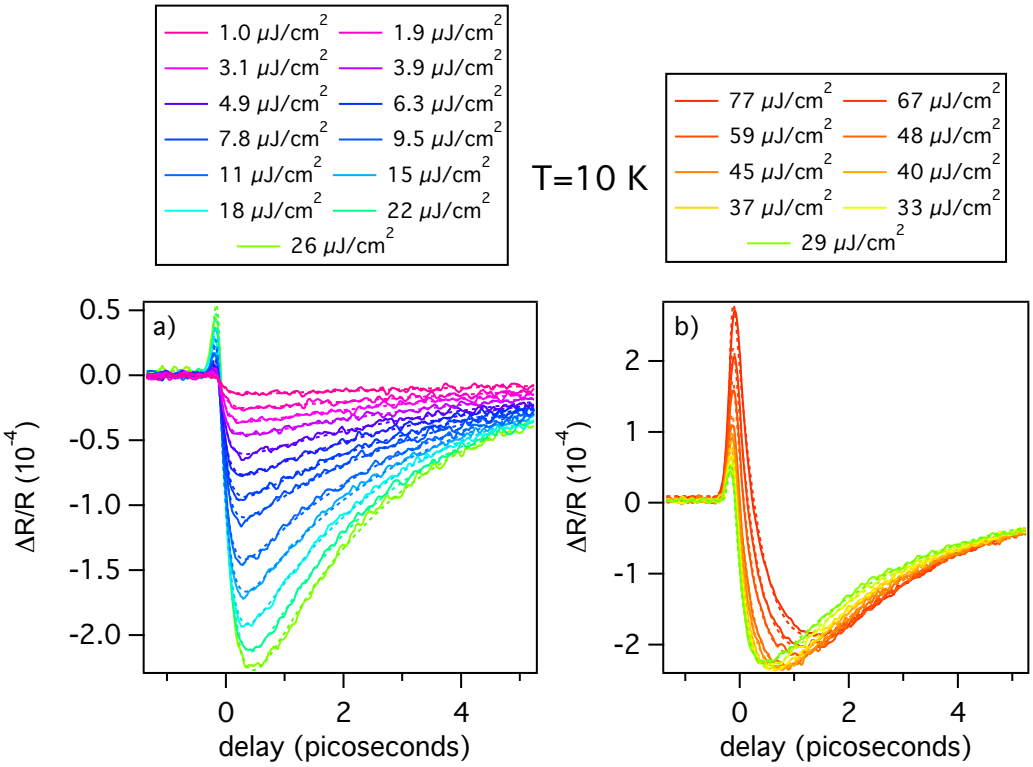


**Figure 5.1: Photoinduced phase transition in overdoped Bi2212** - $\Delta R/R$ signal, solid lines in panel a) and b), at 10 K at different pump fluences. The fit to the experimental curves are shown with dashed lines. In panel a) the low-intensity regime is shown. The panel b) correspond to the high-excitation regime.

## 5.2 Discontinuity in the fluence dependence

In figure 5.1a and 5.1b, I report the ΔR/R traces at 10 K obtained at increasing pump intensity. Similarly to section 4.4, all the curves were fitted using two exponential functions convoluted with the time shape of the laser pulse. The results of the fit are superimposed to the experimental curves. Figure 5.2 shows the SCS amplitude and decay time for each fit as a function of pump fluence.

The low-excitation regime, i.e., the regime where the SCS is proportional to the pump fluence is reported in figure 5.1a and in fig-

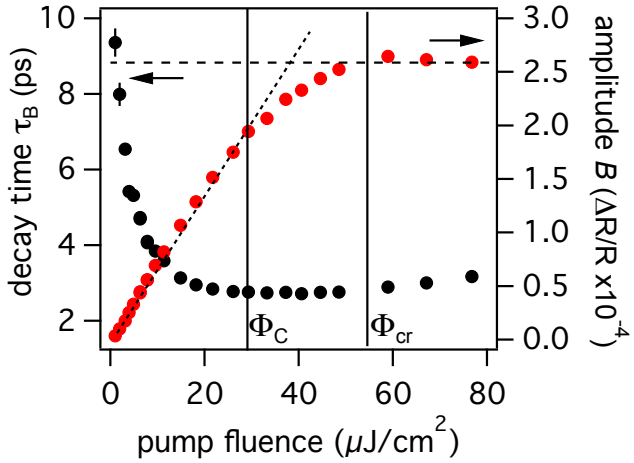


**Figure 5.2: Photoinduced phase transition in overdoped Bi2212** - The fit parameters (decay time $\tau_B$ and amplitude $B$) obtained from the data of Fig. 5.1 are reported here as a function of pump fluence. The short-dashed line is the linear fit in the low-fluence regime. The long-dashed line represents the saturation value. The error bars are within the circles size.

ure 5.2 below 26 $\mu$J/cm$^2$ $\equiv \Phi_C$. In agreement with previous works (27, 28, 29, 30, 65, 71, 72, 73, 74, 75, 76, 77, 78), I assume here that the SCS is proportional to the photoinduced QP density, $n_{ph}$. Thus I conclude that $n_{ph}$ increases linearly with the pump fluence in this regime. In the zero-fluence limit, where $n_{ph} \to 0$, I observe a divergence of the decay time (figure 5.2). This is related to (4.7), as the total QP density, ($n_{ph}$+$n_T$), becomes extremely small at low fluence and at low temperature (10 K).

Above $\Phi_C$ the SCS has a sub-linear dependence and I identify this regime as the high-excitation regime (28, 29) (figure 5.1b and figure 5.2 for $\Phi > \Phi_C$). In this regime, the SCS exhibits a saturation at a critical fluence, $\Phi_{cr}$, of $\sim$55 $\mu$J/cm$^2$. This saturation means that no more Cooper pairs can be destroyed above $\Phi_{cr}$ and it is considered as the evidence of the superconducting condensate vaporization during the laser pump pulse (28, 29). The fact that the crossover between the linear and the saturated regime does not show an abrupt discontinuity here can be justified by the spatial profiles of the pump and probe light

pulses (28). The occurrence of a real PIPT in this regime has been proved by measuring the emergence of a fast component above $\Phi_{cr}$ in underdoped Bi2212 single crystals (29). Similarly I observe in figure 5.1b an enhancement of the positive signal $A$ associated with the fast e-ph free carriers relaxation.

I can compare the SCS in the case of the photoinduced (figure 5.2) and the thermally induced phase transition (inset of figure 4.15). In the former case, the parameter setting the level of perturbation of the system is the pump fluence, while in the latter case this role is played by the sample temperature. Within this analogy, the critical fluence $\Phi_{cr}$, at which the SCS exhibits the saturation, is the counterpart of critical temperature, $T_C$.

According to non-equilibrium superconductivity models (34, 35, 68) a superconducting-to-normal-state PIPT can be either a first-order non-thermal phase transition ($\mu^*$ model) (34, 35) or a quasi-thermal second order phase transition (T* model) (35, 68). In the T* model the quasi-thermal condition is applied to electrons and high-frequency bosons, both being distributed with statistics at an effective temperature T*. In both cases the saturation of the SCS reflects the impossibility of exceeding a critical QP density in the stable superconducting phase (29, 34, 35, 68).

In analogy to the thermal case (studied in section 4.4), the quasi-thermal photoinduced vaporization would cause the superconducting order parameter to vanish at $\Phi_{cr}$. Thus a diverging decay time should be measured, according to (4.12) and (4.10), and in analogy to experimental results about the PIPT in CDW (31, 32) and SDW (33) compounds. On the contrary, the experimental results here reported show a decay time that remains finite and below 3.2 ps, thus excluding the quasi-thermal origin of the PIPT and suggesting a finite gap at the threshold fluence.

However, the connection between the decay time of the SCS and the superconducting gap is firmly established only in the low-fluence regime within the analytical results of the the RT model (65) (section 4.4, (4.12)). To extend this concept to the high-fluence regime, when

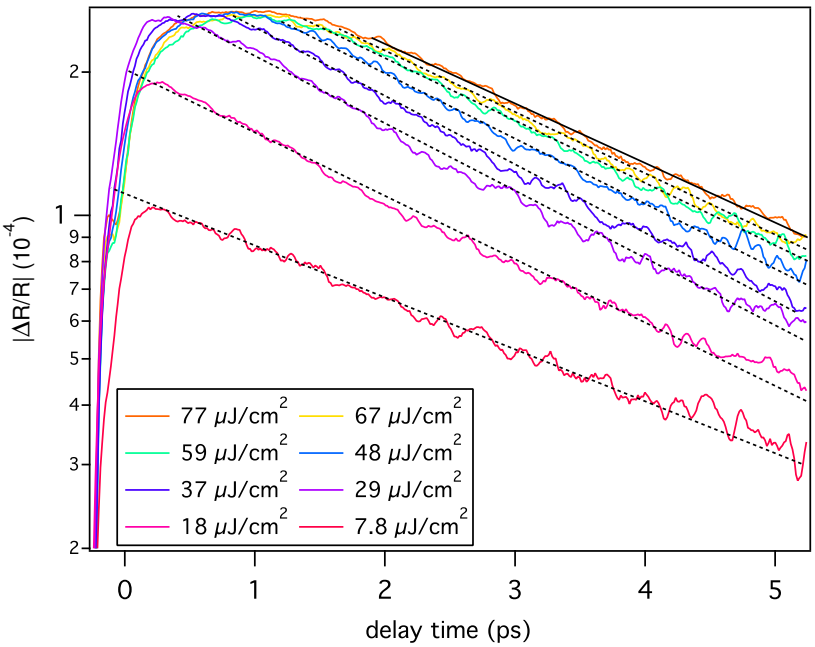


**Figure 5.3: Relaxation of superconducting signal at high fluence** - We report the $|\Delta R/R|$ traces in logarithmic scale at several pump fluences at T = 10 K, where the exponential $A$ component has been subtracted. The dashed lines represent the exponential fit of the decay. The solid line refers to the curve at $\Phi = 77\mu\text{J/cm}^2$.

the non-equilibrium superconducting gap $\Delta(t)$ could strongly vary in time, a validation of the RT model is necessary.

Before I start to discuss this point in section 5.3, I report two important experimental facts about the dynamics of the SCS (See figure 5.3),

a) the relaxation dynamics is well reproduced by exponential decays (dashed lines) in the high-fluence regime, as in the low-fluence one. This decay is compatible with the RT model, where the gap is assumed to be constant in time, thus suggesting that the variations of $\Delta(t)$ are small

b) for $\Phi > \Phi_{cr}$, the decay dynamics collapse into a single curve, indicating that the non-equilibrium gap $\Delta(t)$ reaches its minimum value at $\Phi_{cr}$, remaining the same at higher fluences.

## 5.3 Rothwarf-Taylor model in the high fluence regime: a time-dependent approach

When a superconducting system is strongly perturbed through an ultrashort laser pulse, I expect the superconducting order parameter $\Delta$ to have strong variations in time. The parameters $\beta$, $\eta$ and $\gamma_{esc}$ of the RT model (see Sec. 2.3.1 for definitions) are affected by these variations (references (72) and (118)) and can vary in time. Therefore the high-perturbation limit requires a new time-dependent Rothwarf-Taylor model. Herewith below I use the following assumptions,

i) the time-dependent non-equilibrium superconducting gap $\Delta(n(t))$ can be expressed as a function of $n(t)$ considering the T* and $\mu$* models (34, 35, 68). In both cases the normalized $\Delta(n(t))$ depends on (1-$an(t)$) (being $n(t)$ the QP density and $a$ a conversion factor) for an s-wave gap symmetry and (1-$an(t)^{3/2}$) for a d-wave gap symmetry.

ii) $\beta(\Delta(n(t)))$ is constant, being its temperature dependence very weak, as reported on YBCO (71)

iii) $\eta(\Delta(n(t)))$ is determined with a fit of the rise time at low fluence (See Sec. 2.3.1) and is set to a constant. This is a justified by the weak temperature dependence of the pair-breaking time (28, 65) observed in pump-probe experiments at low fluence (71, 79) (see section 4.4)

iv) $\gamma_{esc}(\Delta(n(t))$ is the only time-dependent parameter and is responsible for the gap-dependence of $\Gamma(T, \Delta)$, evidenced in section 4.4 (4.12). The value corresponding to the unperturbed gap, $\gamma_{esc}(0)$, can be determined by a fit of the experimental decay at low fluence using the time-independent RT model. (See Sec. 2.3.1)

v) following a well-established trend in the literature (27, 28, 65, 119) I assume that the cuprates are in the strong-bottleneck regime. I can thus conclude that $\Gamma \propto \gamma_{esc}$ (65).

Under these approximations, the time-dependent RT equations are:

$$\dot{n} = I_{QP}(t) + 2\eta p - \beta n^2 \tag{5.1}$$

$$\dot{p} = I_{ph}(t) - \eta p + \beta n^2/2 - \gamma_{esc}(t) \cdot (p - p_T) \tag{5.2}$$

with

$$\gamma_{esc}(t) = \gamma_{esc}(0) \cdot (\Delta(n(t))/\Delta(0))^{2\alpha} \tag{5.3}$$

where for an s-wave gap symmetry we have:

$$\gamma_{esc}(t) = \gamma_{esc}(0) \cdot (1 - an(t))^{2\alpha} \tag{5.4}$$

and for a d-wave gap symmetry:

$$\gamma_{esc}(t) = \gamma_{esc}(0) \cdot (1 - an(t)^{3/2})^{2\alpha} \tag{5.5}$$

with $a$ being a conversion factor which set the perturbation of the non-equilibrium gap by QPs and $\alpha$ the exponent appearing in (4.12) determined in section 4.4 ($\alpha \sim 1$). The time-dependent RT equations, (5.1) and (5.2), are then integrated numerically and used to fit the experimental curves of the SCS.

In figure 5.4 I report the results relevant to a single experimental curve at $\Phi = \Phi_C$ and T = 10 K, where I assume a d-wave gap symmetry (5.5). The determined $a$ parameter is $(1.0\pm0.2)\times10^{-20}$ cm$^3$. The agreement with the experimental data is very good. The predicted normalized non-equilibrium gap, $\Delta(t) \propto (\gamma_{esc}(t))^{\frac{1}{2\alpha}}$, shows a minimum of 60% at the maximum SCS and an almost complete gap relaxation (85%) after a time delay of 5 ps. Similar results are obtained considering an s-wave gap symmetry (5.4).

For comparison, I report also two fits where $a$ is held constant with values $a = 0$, equivalent to the time-independent RT model, and $a = 2.45\times10^{-20}$ cm$^3$, where the gap is suppressed by $\approx 95\%$. In the latter case the predicted relaxation dynamics is extremely slow (of the order of several tens of picoseconds) and strongly non-exponential. Both these characteristics are not compatible with any of the experimental curve reported in figure 5.3, thus excluding, within the time-dependent RT model, that at any pump fluence $\Phi$ reported in this work the non-equilibrium gap can be close to zero.

In turn, this result excludes the complete closing of the superconducting gap expected in the case of a second-order quasi-thermal

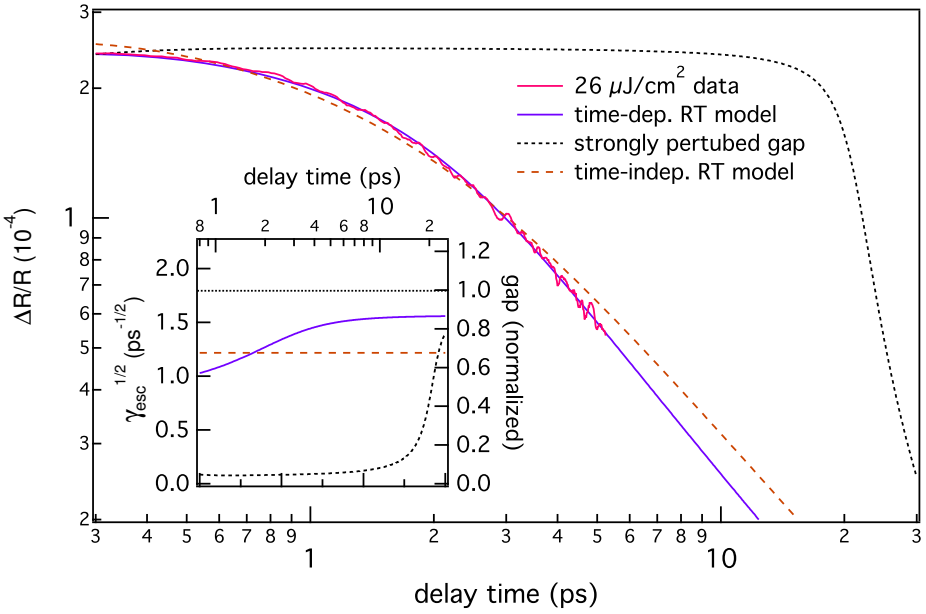


**Figure 5.4: Application of time-dependent Rothwarf-Taylor model** - $|\Delta R/R|$ of the SCS at $\Phi = 26\ \mu$ J/cm$^2$ and the corresponding fit (solid line) obtained with the numerical solutions of the time-dependent Rothwarf-Taylor equations, (5.1) and (5.2), considering a d-wave gap symmetry. The $a$ optimal value is $(1.0\pm0.2)\times10^{-20}$ cm$^3$. For comparison we also show the fits when the parameter $a$ is fixed to the values $a = 2.45\times10^{-20}$ cm$^3$ (short-dashed) and $a = 0$ (long-dashed), which is equivalent to the time-independent RT model. In the inset we show the corresponding function $(\gamma_{esc}(t))^{\frac{1}{2\alpha}}$, which is proportional to the non-equilibrium superconducting gap $\Delta(t)$ (5.3). We normalized the gap to the low-fluence value (See Sec. 2.3.1).

phase transition and strongly indicates a finite superconducting non-equilibrium gap. It is possible to estimate a lower bound for this finite non-equilibrium gap, considering the optimal $a$ parameter and extracting $\Delta(n(t))_{min}$ from the maximum SCS for each curve in figure 5.3. The result is that, at any time instant $t$ where the RT model is applicable, the condition $\Delta(t) > \frac{1}{2}\Delta(0)$ is realized.

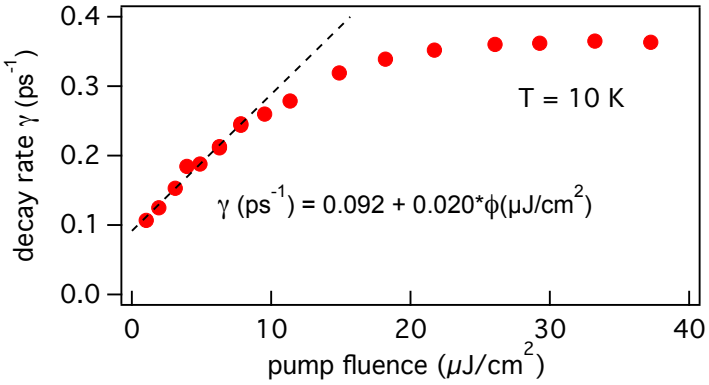


**Figure 5.5: Decay rate as a function of pump fluence** - Experimental decay rate extracted by the fit of the ΔR/R traces at different pump fluences (see figure 5.1). The dashed line is the linear fit obtained in the low-intensity limit. The error bars are within the circles size.

## 5.4 Scenarios for a superconducting-to-normal-state dynamical phase transition

Although the time-dependent RT model discussed in the previous section provides a remarkably good description of the experimental data, I observe that the time-independent RT model is also a valid approximation, provided an average gap value (corresponding to the value predicted by the time-dependent approach at 1-2 ps delay) is assumed. In particular I demonstrated that in the experimental conditions reported in this chapter the condition $\Delta(n_{ph}, 10K) > \frac{1}{2}\Delta(0, 10K)$ is verified. Thus I can estimate the maximum density of photoexcited QP, $n_{ph} < n_{T=70K} << \eta/\beta$ (according to the inset of figure 4.17 and (35)). This condition insures the validity of the analytical formulas obtained in section 4.4.

I recall (4.7) and, plotting the decay rate as a function of pump fluence (figure 5.5), I observe the expected linear dependence at low fluence. The intercept of 0.092 ps$^{-1}$ is related to the finite value of $n_T$ at

T = 10 K. This linear dependence on the pump fluence follows the trend observed on underdoped HTSC (71, 76), but was not observed clearly on overdoped samples (76, 120). I define an effective photoinduced decay rate, $\gamma_{ph}$,

$$\gamma_{ph}(T, \Delta(n_{ph}), n_{ph}) \equiv \gamma(T, \Delta(n_{ph}), n_{ph}) - \gamma_T(T, \Delta(0), n_{ph} = 0) \quad (5.6)$$

that represents the decay rate exclusively due to the photoinjected QPs, where the thermal contribution to the decay rate, $\gamma_T$, (intercept in figure 5.5) has been subtracted. Here I neglect the sample temperature dependence since in our pump-probe experiment this parameter remains constant. Thus I obtain the formula

$$\begin{aligned}&\gamma_{ph}(\Delta(n_{ph}), n_{ph}) = \\ &\quad n_{ph}\Gamma(\Delta(n_{ph})) + n_T[\Gamma(\Delta(n_{ph})) - \Gamma(\Delta(0))] \approx n_{ph}\Gamma(\Delta(n_{ph}))\end{aligned} \quad (5.7)$$

In the right-hand side of (5.7) I neglected the second term of the sum. This approximation is valid in the high-excitation regime when $n_{ph}$ is much larger than $n_T$, as long as $\Gamma$ is not going to zero, which is suggested by the absence of a decay time divergence.

Using (4.12) and the proportionality between $n_{ph}$ and $\Delta R/R$ I can rewrite (5.7) as

$$\gamma_{ph} = \frac{\Delta R}{R}\Delta^{2\alpha} \quad (5.8)$$

from which I obtain:

$$\left(\frac{\gamma_{ph}}{\Delta R/R}\right)^{\frac{1}{2\alpha}} \propto \Delta \quad (5.9)$$

I thus define the quantity $\delta \equiv \left(\frac{\gamma_{ph}}{\Delta R/R}\right)^{\frac{1}{2\alpha}}$, proportional to the non-equilibrium superconducting gap, $\Delta$, and we assume $\alpha \sim 1$ (section 4.4).

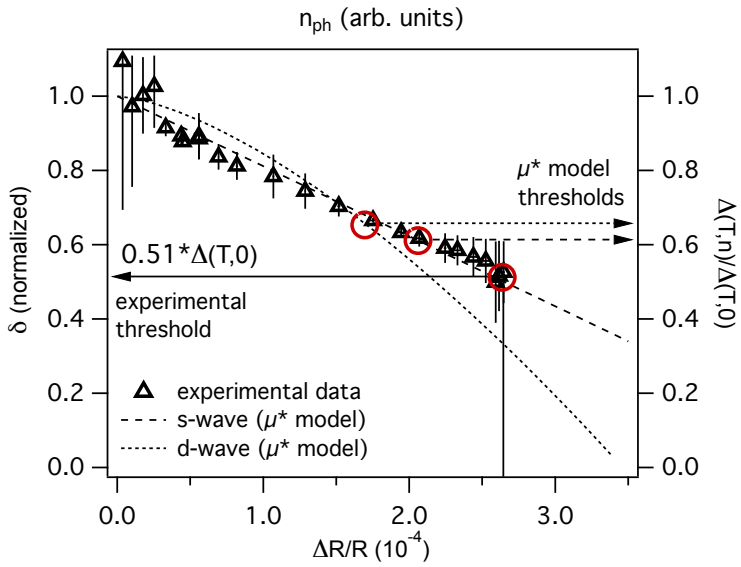


**Figure 5.6: Photoinduced superconducting gap suppression** - $\delta$ as a function of $\Delta R/R$. I normalize the value to the zero fluence limit, which correspond to the equilibrium gap $\Delta(T,0)$. The error bars indicate the difference between the results obtained starting from the analytic solution of the RT equations (4.7) and the numerical one (see text). On the same graph (right and upper axis) I show the analytical results of the $\mu^*$ model for the superconducting gap, $\Delta$, as a function of QP density $n$ as reported in (35) for both s-wave and d-wave cases. The threshold values are calculated numerically within the $\mu^*$ model (35) at a finite temperature corresponding to 10 K in our experiment.

In figure 5.6 I report the value of this quantity, normalized to the zero fluence limit value, obtained from the experimental curves of figure 5.1 as a function of the SCS amplitude. The gap value decreases with $\Delta R/R$, hence it decreases with increasing $n_{ph}$, as expected (34, 35, 68). On the other side, above the experimental threshold, where $n_{ph}$ is constant, the non-equilibrium gap remains constant, reflecting the correctness of neglecting the T dependence in $\Delta(n_{ph}, T)$ and $\gamma_{ph}(T, \Delta, n_{ph})$.

The experimental data are here compared to the predictions of the $\mu^*$ model, where a first-order phase transition is expected (29, 34, 35). Within this model the non-equilibrium QP population is described by a

Fermi-Dirac distribution with an effective chemical potential $\mu^*$, while its temperature remains at the equilibrium value T. In figure 5.6 I plot the analytical results for $\Delta(n, T = 0)/\Delta(n = 0, T = 0)$ in the low-excitation limit as a function of the QP density $n$ for both s-wave and d-wave gap symmetry (35). The dependence in the d-wave case is $\propto n^{3/2}$, while it is linear in the s-wave case, as reported in the previous section.

The $\mu^*$ model predicts a superconducting-to-normal-state phase transition at a finite gap value, when the superconducting-state free energy increases above the normal-state value. At 10 K this phase transition should take place at a relative gap value of ≈60% and ≈65% in the s-wave and d-wave case, respectively (35) (figure5.6b)

The main features evidenced by the experimental data reported in figure 5.6 are: i) a finite value of $\Delta(n_{max}, T = 10\,K)$ of about 1/2 of the equilibrium value at the fluence threshold, ii) the linear dependence of $\Delta(n_{ph}, T = 10\,K)$ with $\Delta R/R$ and thus with $n_{ph}$.

The result i) self-consistently confirms the initial assumption of a non-vanishing $\Gamma$ function and of $\Delta(n_{ph}, 10K) > \frac{1}{2}\Delta(0, 10K)$. The experimental value obtained in this work is remarkably close to the $\mu^*$ model predictions, even if a quantitative comparison would require a detailed analysis of the photoinduced QP distribution and accurate numerical calculations in the high-fluence regime (29, 35).

The result ii) suggests an s-wave like dependence of the non-equilibrium gap. Even if this finding seems in contradiction with the equilibrium gap d-wave symmetry reported for HTSC (51), one should bear in mind that the non-equilibrium population photoinduced by a 100 fs laser pulse in a d-wave superconductor is mostly peaked in the anti-nodal region (121) because of energy-momentum conservation constraints (71, 122). This leads to a non-thermal effective distribution that can be reproduced by a Fermi-Dirac statistic with anisotropic effective chemical potential.

The results of such anisotropic model are equivalent to those obtained for an s-wave superconductor. An s-wave like gap symmetry was previously used to explain the temperature dependence of $n_{ph}$ in

the low-excitation regime of HTSC (72) and led to a strong controversy in the pump-probe experiments interpretation (35, 72). I remark that this result does not imply an s-wave gap symmetry in HTSC at equilibrium and it is rather related to the excitation process.

Both these results suggest a strongly non-thermal QP population distribution, thus opening two possible physical scenarios behind the superconducting-to-normal PIPT: i) the first-order dynamical phase transition predicted by the $\mu^*$ model (29, 34, 35) and supported by the time-dependent RT model (section 5.3), ii) a second-order transition with a quick ($< 1$ ps) gap recovery, where the fundamental assumptions of the RT model break down on the short timescales in the high-excitation regime.

The second scenario goes beyond the treatment proposed in section 5.3 as the phonon bottleneck would be avoided on the short timescales due to the highly non-thermal QP distribution. The break down of the RT equations implies the decoupling of the relaxation dynamics of QP and high-frequency bosons, assessing the non-thermal character of the PIPT, in contrast with the quasi-thermal PIPT predicted by the T* model (35, 68). Within the first picosecond the superconducting state is recovered with a finite non-equilibrium gap, as demonstrated in this section.

However the time-dependent RT model reproduces very precisely the experimental dynamics at $\Phi_C$ (figure 5.4, section 5.3), thus suggesting the validity of this model at excitation levels quite close to the PIPT. Thus, while the non-thermal second-order phase transition implies an abrupt break down of this model between $\Phi_C$ and $\Phi_{cr}$, the non-thermal first-order transition is compatible with the time-dependent RT model also above $\Phi_{cr}$.

The dynamics of such first-order phase transition as discussed in (29), in analogy to the coalescence dynamics of a supersaturated solution (123), might reflect a dynamical inhomogeneity in the probed area, where normal-state metastable domains compete with the surrounding superconducting state.

The results reported in this chapter are obtained assuming the validity of (4.7), which is an approximated analytic solution of the time-independent RT equations (109). I repeated the same procedure starting from the numerical solution of the time-independent RT equations, which is valid in the whole temperature and fluence range. However the final results of our work are unaffected. The error bars in figure 5.6b account for the deviation of the analytic results from the numerical one.

Both the hypothesis proposed in this section have a non-thermal character, at variance with the quasi-thermal PIPT reported on other systems, such as CDW (31, 32) and SDW (33). Since the photoexcitation process is the same, this remarkable difference calls for a deeper understanding of the non-equilibrium QP and bosons thermalization processes in HTSC in respect to CDW and SDW compounds.

## 5.5 Conclusion

In this chapter I reported pump-probe experiments on an overdoped Y-Bi2212 sample at 800 nm. I explored both the low- and the high-excitation regimes to study the origin of the recently discovered photoinduced vaporization of the superconducting condensate (28, 29). I start here from the results obtained in the previous chapter regarding the power-law divergence at low-excitation in the vicinity of $T_C$.

In the high-excitation regime, I show the lack of the quasiparticles decay time increase at the fluence required to photoinduce the transition, in contrast to previously reported PIPTs on CDW (31, 32) and SDW (33) systems. At that fluence ($\Phi_{cr} \approx 55$ $\mu$J/cm$^2$) I estimate a finite non-equilibrium gap value (1 ps after the interaction with the pump pulse) of about 1/2 of the equilibrium gap.

This finding proves the non-thermal character of the superconducting-to-normal-state PIPT, leading to two possible phase transition mechanisms: i) a first-order dynamical phase transition predicted by the $\mu^*$ non-equilibrium superconductivity model (29, 34, 35), and supported by numerical solutions of an extended time-dependent RT model, ii)

a second-order transition with a quick gap recovery, where the fundamental assumptions of the RT model abruptly break down in the high-excitation regime on the short timescales (t $<$ 1 ps).

These findings tackle the fundamental question on the interaction of an infrared coherent pulse with the superconducting condensate in HTSC at high excitation pump intensity. This is a landmark for the growing field of pump-probe techniques on HTSC (28, 29, 30, 78, 83, 84, 91, 116, 117). Our experiment defines the maximum pump fluence ($\Phi_{cr}$ $\approx$ 55 $\mu$J/cm$^2$) which still allows to probe the superconducting state of Y-Bi2212; it also demonstrates that recent pump-probe experiments performed on Bi2212 at higher pump fluences (83, 84, 116) are dealing with a dynamical competing admixture of superconducting, normal and possibly pseudogap phases.

The striking difference here reported for the PIPT in HTSC as compared to CDW (31, 32) and SDW (33) opens an interesting perspective for a deeper understanding of the fundamental differences in the non-equilibrium properties of these compounds.

# 5. EVIDENCE OF A NON-THERMAL SC-NS PIPT

# Chapter 6

# Real-time Dynamics of Competing Phases

## 6.1 Introduction

In this chapter I exploit the novel time-resolved spectroscopic technique developed in this Ph.D. thesis to show for the real-time competition of different quasi-particles (QPs) in the superconducting state of an overdoped cuprate single crystal (OD86). The signal associated to each kind of QP, namely the excitations of superconducting, pseudogap and normal states, is recognized by its low-fluence optical response, which has been thoroughly studied in chapter 4. Of particular interest is the study of this dynamics at those fluences where the photoinduced phase transition studied in chapter 5 takes place. The reconstruction dynamics of the superconducting state after this transition and its dynamical competition with the underlying pseudogap state can be obtained with this approach. Clear evidences of both coexistence and competition between the superconducting condensate and pseudogap QPs are here reported.

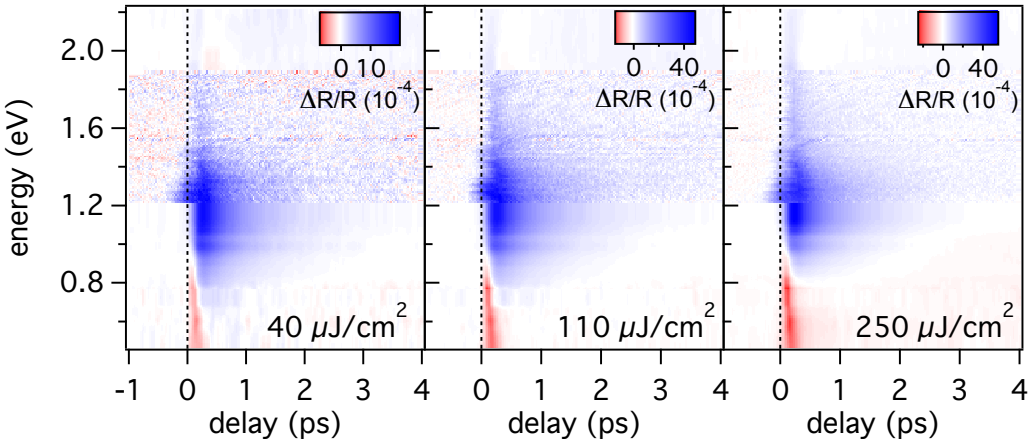


**Figure 6.1: Spectral response at different fluences, 100K** - Time-energy $\Delta R/R(\omega, t)$ matrices at increasing pump fluence (from left to right) and at 100 K. A gamma correction has been applied to each color scale.

## 6.2 Photoinduced modifications of spectral response

The experimental results reported here come from two distinct series of data acquisitions, one with the Near-Infrared pump-tunable wavelength probe set-up (T-ReX Lab, Fermi@Elettra, Trieste) and one with the Near-Infrared pump-Supercontinuum probe set-up (Elphos Lab, Universitá Cattolica del Sacro Cuore, Brescia)(see Chap. 3 for details on the experimental set-ups). To let the joint spectral response to be meaningful those measurements were performed in the two labs with the most similar experimental conditions, i.e., same doping and sample composition, same temperature, pump fluence, pump/probe absorbed power ratio ($\sim$ 20), pump/probe beam diameter ratio ($\sim$ 1.5 - 2) and laser repetition rate (250 - 125 kHz).

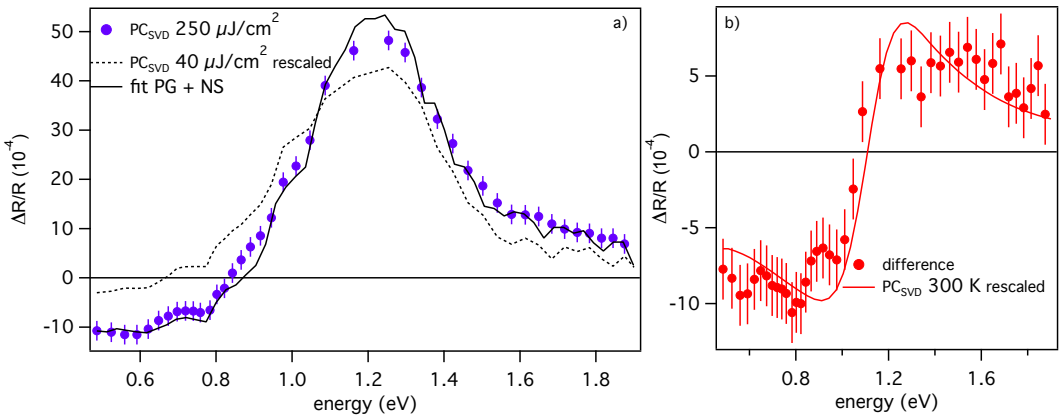


**Figure 6.2: SVD decomposition at high fluence, 100 K** - a) Principal component spectral response at 250 $\mu J/cm^2$ compared to the rescaled 40 $\mu J/cm^2$ principal component. The difference is shown in panel b and compared to the principal component at 300 K. The weights of the fit in panel a are 2.2 and 3.8 respectively for the PG (40 $\mu J/cm^2$) and NS (10 $\mu J/cm^2$) components.

### 6.2.1 Pseudogap phase

In Fig. 6.1 I report the $\Delta R/R(\omega, t)$ signal at three different fluences in pseudogap state (100 K). Here I observe that the spectral shape of the response does not change dramatically at high fluence: the broad positive response (blue) centered at 1.2 eV is the dominant feature with maximum reflectivity variations of 1.9, 4.7 and $5.3\times10^{-3}$ respectively at 40, 110 and 250 $\mu J/cm^2$. While between 0 and 110 $\mu J/cm^2$ the signal scales linearly, between 110 and 250 $\mu J/cm^2$ a sub-linear dependence sets in. On the opposite, the magnitude of the low energy (below 1.0 eV) negative signal increases linearly with fluence. The different fluence dependence causes the small variation in the ratio between positive and negative $\Delta R/R(\omega, t)$ signal observed in Fig. 6.1, suggesting a different origin of the two signals.

An analysis through the Singular Value Decomposition method (see Chap. 3) supports this hypothesis and allow to recognize their origin. In Fig. 4.4 I compare the spectral traces of the principal component at high fluence with that of the low-fluence limit (Fig. 4.4). Here I show

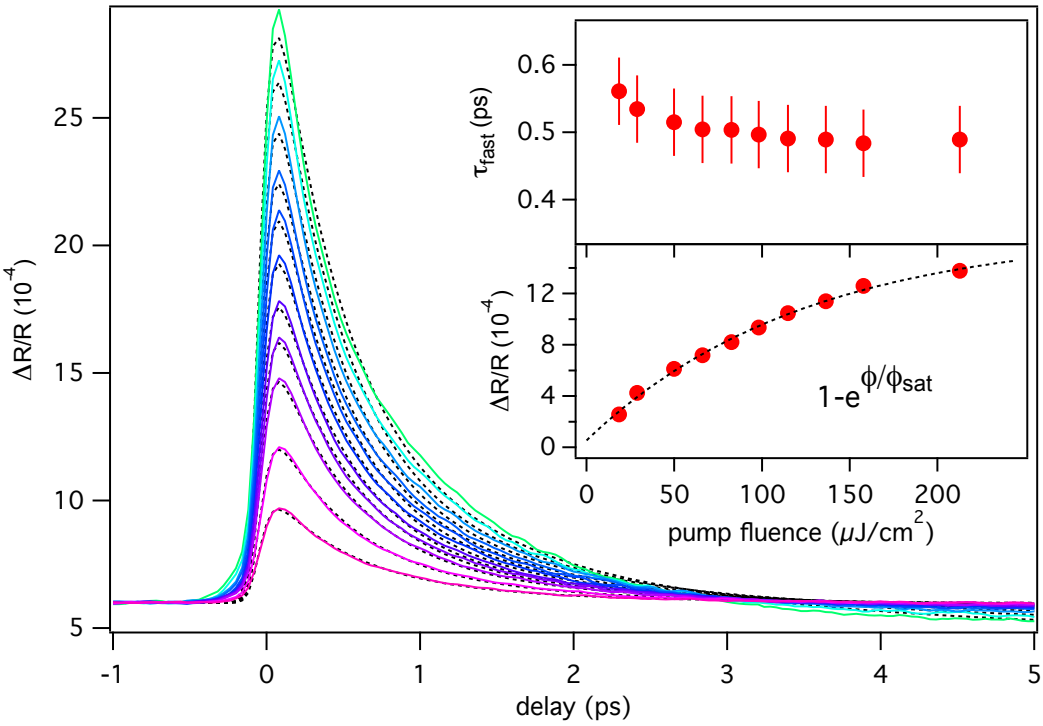


**Figure 6.3: Dynamics at 1.0 eV, 100K** - $\Delta R/R(t)$ at 1.0 eV at different pump fluences and at 100 K.). In the inset the parameters of the fast component are shown. The $\Delta R/R$ peak saturates with a $\phi_{sat}$ value of 130 $\pm$ 20 $\mu J/cm^2$. The intensity of the slow component ($\tau$ = 1.8 ps) is one order of magnitude smaller than the fast one and exhibit the same behavior.

that the difference between a rescaled low-fluence component and the high-fluence data is positive above 1.1 eV and negative below, as the normal state principal component (Fig. 4.2). The actual spectral shape is eventually fitted with a composition of the algebraic superposition of two components, both with weights much lower than an extrapolated linear dependence.

Thus there are two main findings: i) the spectral feature of the pseudogap phase, where an impulsive variation of the plasma frequency in the intraband transitions is observed (Sec. 4.3.3), have a sub-linear dependence at high-fluence and ii) the signal at high-fluence can be reproduced by a sum of two spectral responses, the corresponding low-

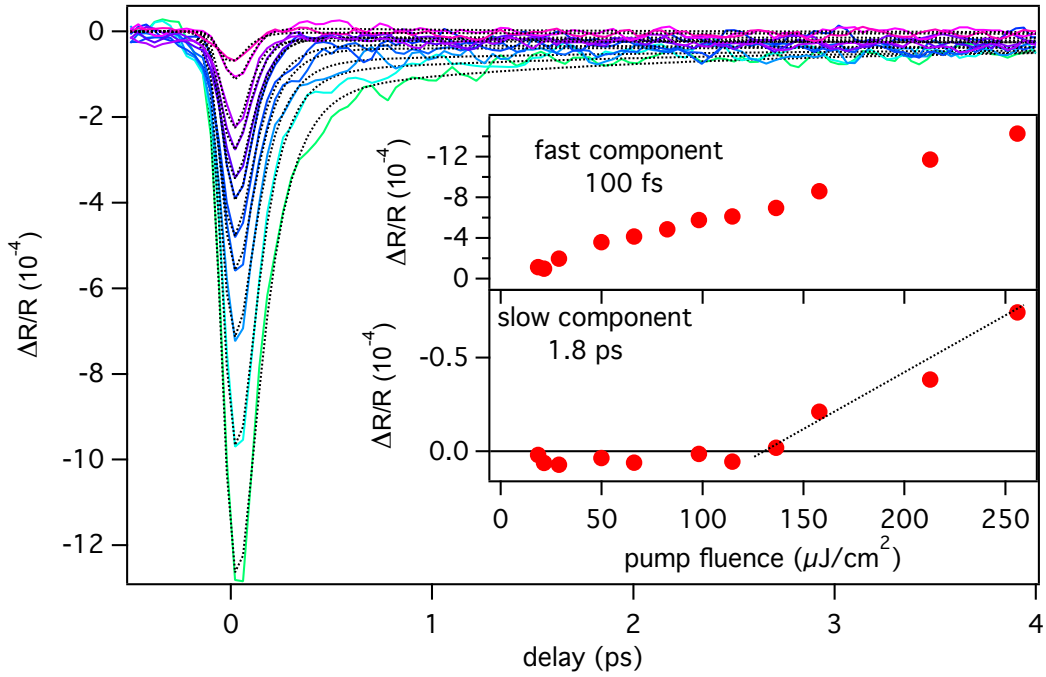


**Figure 6.4: Dynamics at 0.5 eV, 100K** - $\Delta R/R(t)$ at 0.5 eV at different pump fluences and at 100 K.). In the inset the parameters of the exponential fit are shown. The $\Delta R/R$ of the slow component appears above $\phi_{thr}$ value of 130 $\pm$ 30 $\mu J/cm^2$

fluence response at the same temperature and the normal state signal, i.e., quasi-equilibrium heating of the electron and boson gas, with no spectral weight transfer.

In Fig. 6.3 I shown that the detail of the sub-linear dependence as a function of fluence. Here I consider the $\Delta R/R(t)$ signal integrated around 1.0 eV. The $\Delta R/R(t)$ traces have been fitted with two exponential functions, in analogy with previous chapters. The fast component is the dominant one and exhibit a exponential saturation, as shown in the inset, with a value of $\phi_{sat}$ of 130 $\pm$ 20 $\mu J/cm^2$. The relaxation dynamics does not show any substantial variation in this fluence range, with a slight tendency to increase from the average value of 0.5 ps to the low fluence value of 0.55 ps.

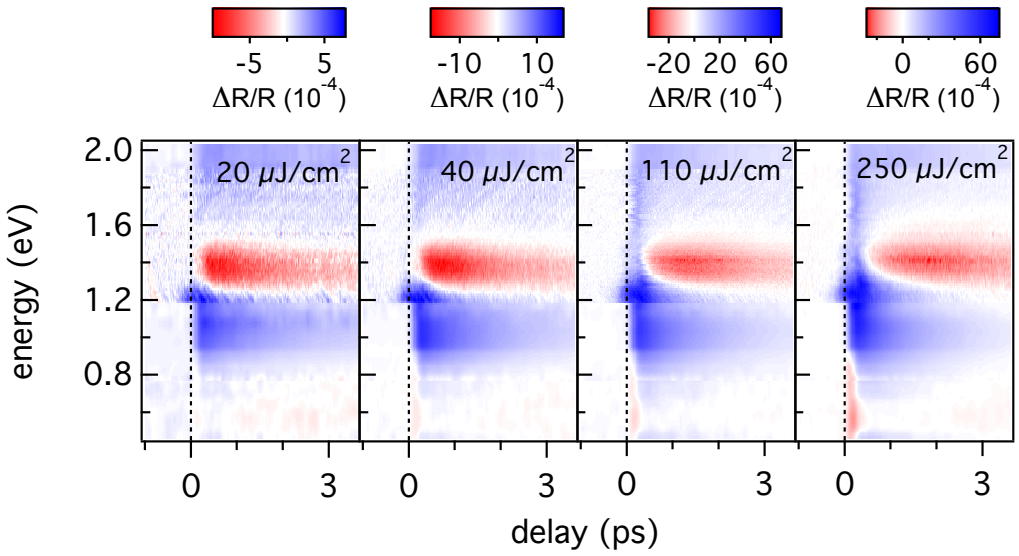


**Figure 6.5: Spectral response evolution at high-fluence, 10K** - Time-energy $\Delta R/R(\omega, t)$ matrices at increasing pump fluence (from left to right) and at 10 K.

At low energies the normal state signal is the dominant spectral feature, as shown in Fig. 6.2. Thus to clarify its origin I performed a fluence dependent $\Delta R/R(t)$ experiment at 0.5 eV. The results are shown in Fig. 6.4 together with the double exponential fit and the corresponding parameters. This series of experimental data shows that the decay time at this energy is very fast and the estimated value of $\sim$ 100 fs reaches the lower bound set by the cross-correlation of pump and probe pulses at 0.5 eV (see Chap. 3). While this fast component scales linearly, a slow ($\tau \sim 1.8$ ps) component appears in the relaxation dynamics only above a threshold pump fluence. The threshold value ($\phi_{thr} \sim 130 \pm 30\ \mu J/cm^2$) is similar to the estimated $\phi_{sat}$ value of the dominant pseudogap component observed at 1.0 eV.

### 6.2.2 Superconducting state

In the superconducting state the spectral response at high fluence changes substantially in respect to the the low-fluence regime (see Fig. 6.5). At 20 and 40 $\mu J/cm^2$ the $\Delta R/R(\omega, t)$ signal is characterized mainly by two features (one positive at an energy of about 1.0 eV and one negative at 1.4 eV) with slow decay time (2-3 ps). At higher fluences (110 and 250 $\mu J/cm^2$) those features are saturated while new spectral features with a fast decay time appear in the spectrum, namely, a negative one in the low energy range ($< 1.0$ eV) and a positive one centered at 1.1 eV. On qualitative grounds and in analogy to the discussion of the previous section, the former resembles the normal state response and the latter the pseudogap one. At high energy (above 1.5 eV) a fast and positive feature is also present.

In particular the principal spectral component obtained by SVD analysis changes dramatically above 40 $\mu J/cm^2$ fluence (see Fig. 6.6). This means that above this pump intensity the main relaxation dynamics includes different kind of optical responses and thus different kind of QPs. To disentangle these components I try reproducing the signal with a superposition of low-fluence superconducting, pseudogap and normal state signals, in analogy to the method developed in the previous section. In Fig. 6.6 I report the results of this procedure and I observe that at about 110 $\mu J/cm^2$ the pseudogap optical response is accounting for the missing area in the spectral response.

Thus the response can be reproduced by a superposition of those fundamental signals and to obtain a dynamical information I adopted the following approach: in analogy to the fit done for the principal component I use a least mean-square fitting procedure to find out, for each time instant $t'$, the amount of each spectral component in the experimental spectrum $\Delta R/R(\omega, t')$. The weight (a real and positive value) of each components $w_{SC}(t)$, $w_{PG}(t)$, $w_{NS}(t)$ at each instant $t$ are the results of this procedure. I remark that the fundamental low-fluence responses come from experimental data, whereas no particular differential model is assumed here.

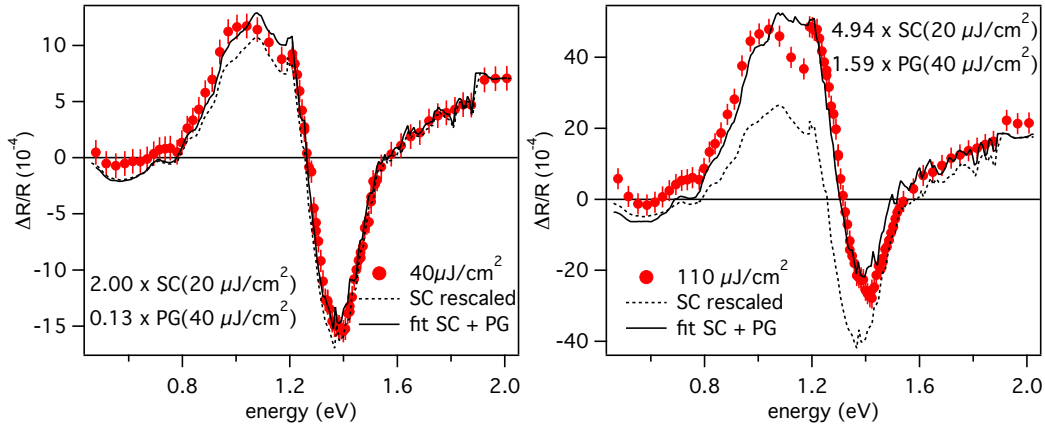


**Figure 6.6: SVD decomposition at high fluence, 10 K** - Principal components of the 40 $\mu J/cm^2$ and 110 $\mu J/cm^2$ data. The fit is done with a superposition of SC and PG low-fluence components.

At this point this is simply a convenient way to decompose the matrix of our experimental data with a rank 3 matrix (following the SVD approach, see Chap. 3). This is an approximation, but reproduces pretty well the data. The implications of this approach will be discussed extensively in the next section. However I mention here that for a system where a spatially inhomogenous admixture of macroscopic phases is present the main assumption that the $\Delta R/R(\omega, t)$ is separable and results from the sum of a set of fundamental components is correct (124, 125, 126). Therefore in this case the weights would have the meaning of the volume fraction of each phase. In these conditions the real-time phase competition dynamics can be extracted from these coefficients. Instead in the case of an homogeneous phase this method is an approximation and the meaning of the weights as volume fractions is no longer valid.

The results obtained with this method are summarized in the Figs. 6.7, 6.8 and 6.10. In Fig. 6.7 I report the superconducting component as a function of time. The dynamics well below saturation ($\phi_{cr} \sim 100$ $\mu J/cm^2$) have the same properties evidenced in chapter 5 and well described by the time-dependent Rothwarf-Taylor model. Instead at high

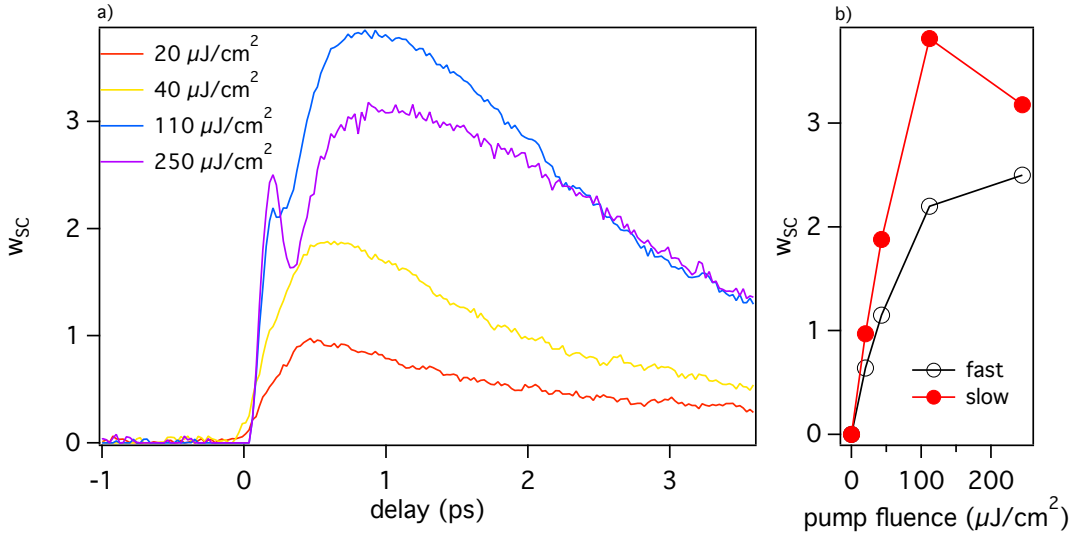


**Figure 6.7: Superconducting state reconstruction dynamics** - a) Dynamics of the weight of the superconducting component $w_{SC}$(t) at different fluences. b) Peak intensity as a function of fluence.

pump fluence, above saturation, new important features arise. On the fast timescales (0-0.3 ps) a saturation is present at an intensity about two times the low-fluence (20 $\mu J/cm^2$) signal. This fast saturation was not visible with single color techniques where the disentanglement of the different signals is more difficult. After this first saturation the signal have a strongly non-exponential dynamics and can also increase above the saturation level suggesting that the condition for the saturation of the superconducting signal depends on the timescale.

In the 250 $\mu J/cm^2$ trace a three steps dynamics is clearly observed. In the first one a very fast ($\sim$ 0.1-0.2 ps) decay is present. At about 0.35 ps the dynamics changes abruptly into an increasing function of time, with a typical rise time of about 0.6 ps. After about 1 ps the dynamics converts again into a decaying function, with a relaxation dynamics compatible with a time-dependent Rothwarf-Taylor model where a finite non-equilibrium gap is considered, in agreement with the results of the previous chapter. It should be noted that the typical critical fluence obtained in this chapter is higher of a factor 2 than

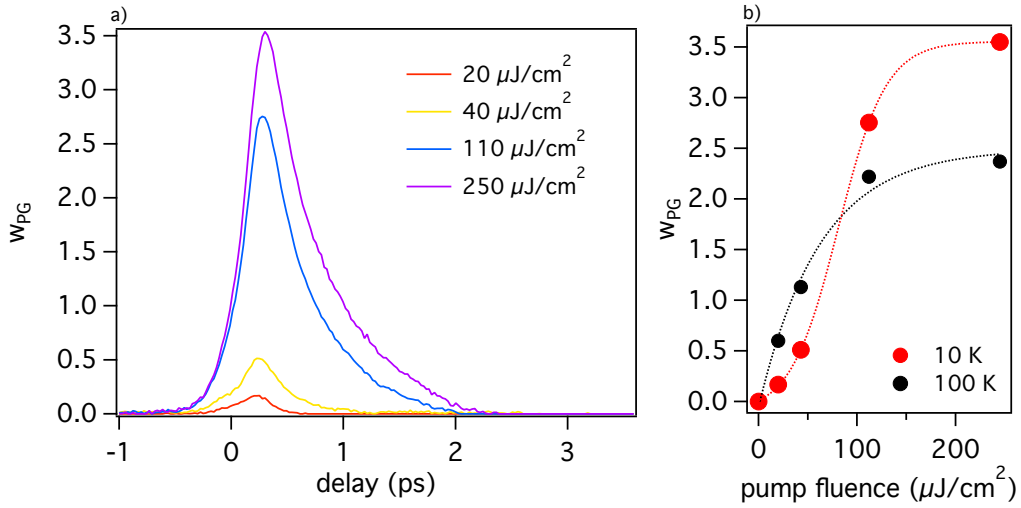


**Figure 6.8: Pseudogap component dyanmics** - a) Dynamics of the weight of the pseudogap component $w_{PG}$(t) at different fluences. b) Peak intensity as a function of fluence.

the one obtained in the previous chapter. This difference is partially due to the more overdoped sample (with higher $T_C$) and partially to the different experimental set-up (in particular because of the different pump-probe interaction volumes (28)).

At fluences below the critical value $\phi_{cr}$, the pseudogap weight has a non-zero component, as shown in Fig.6.8. This component is strongly suppressed when compared to the 100 K data. Moreover its relaxation dynamics is very fast ($\sim$ 0.1-0.2 ps), whereas the low-fluence dynamics of the PG excitations at 100 K at low-fluence has a timescale of 0.6 ps (Fig.6.3).

On the contrary, above the critical fluence $\phi_{cr}$, the signal of pseudogap-like QPs at 10 K is more intense than the signal at 100 K. In facts, a jump of the quantity $w_{PG}$ is observed across $\phi_{cr}$ Fig. 6.8. Above $\phi_{cr}$ the decay relaxation dynamics of $w_{PG}$ is similar to the 100 K data.

In Fig. 6.9 I compare the fast decay times of the exponential decay of the PG component at 10 K and 100 K. The result is that while at 100 K the fast decay time is substantially independent to fluence with a value around 0.5-0.6 ps, in the superconducting state the decay time

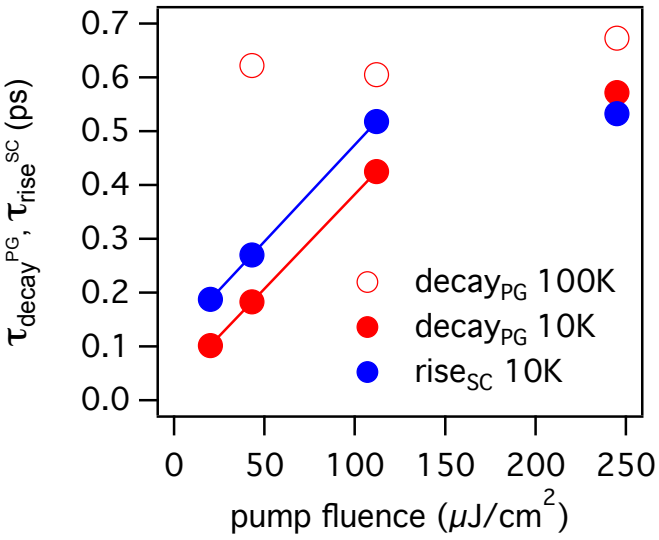


**Figure 6.9: Decay times of different components at high fluence** - Decay times of the weight of the pseudogap component at 10 K and 100 K. Rise time of the weight of the superconducting component at 10K.

is faster ($\tau \sim 0.1$ ps at 20 $\mu J/cm^2$) and strongly depends on the pump fluence. Eventually it reaches the 100 K value of 0.5 ps at the highest fluence (250 $\mu J/cm^2$).

The weight of the normal state component is shown in Fig. 6.10. This component has a minor role in the dynamics and is present only on the short timescales. This means that normal-state-like excitations, i.e., thermal excitations not accompanied with a spectral weight shift are suppressed in the SC phase. An evaluation of the weight $w_{NS}$ in terms of instantaneously photoinduced ungapped volume fraction would gives less than 10% of the interaction volume. The very short lifetime of this component suggest that this signal is more likely originated by the thermalization of high-energy QPs, rather than a real NS phase competition. These results suggest a phase competition involving the pseudogap and the superconducting states.

To highlight the dynamical competition between PG and SC, I show in Figs. 6.11 and 6.12 $w_{SC}$ and $w_{PG}$ on the same intensity scale. In the low-fluence limit the PG optical response temporally anticipate the SC

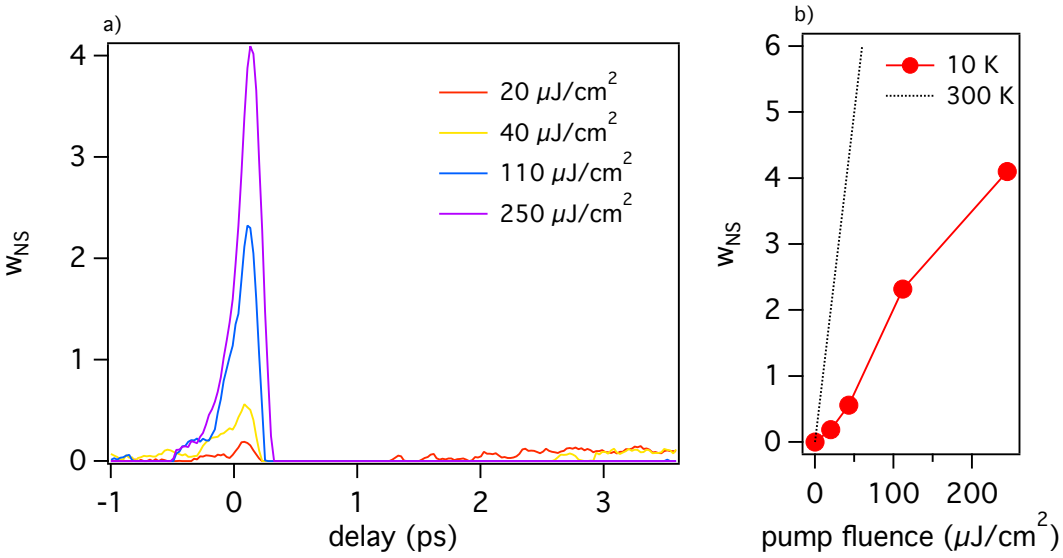


**Figure 6.10: Normal state component dynamics** - a) Dynamics of the weight of the normal state component $w_{NS}$(t) at different fluences. b) Peak intensity as a function of fluence.

optical response. A fit with exponential functions reproduces very well the dynamics. The fit parameters show that the relaxation time of PG excitations ($\sim$ 0.1 ps) is 100 fs faster than the SC rise time ($\sim$ 0.2 ps). However the two timescales have a very close relationship, as demonstrated by their fluence dependence (Fig. 6.9), where they increases linearly with fluence following the same dependence, with a roughly constant difference 0.1 ps. The linear increase ceases when above $\phi_{cr}$ the 100 K decay time of PG QPs is reached by both timescales, suggesting it as the ultimate limiting factors for the slowing down of the superconducting state reconstruction dynamics.

A close look to the dynamics at the highest fluence (250 $\mu J/cm^2$) shows that the rise time here is considered as the rise time of the slow peak. The fast superconducting peak has a rise time that initially follows the one of PG excitations, but its abrupt saturation after less than 0.2 ps make it a clear signature of the photoinduced phase transition on the fast timescales. After this saturation the PG excitations starts to dominate the volume fraction and the maximum $w_{PG}$ coincides with

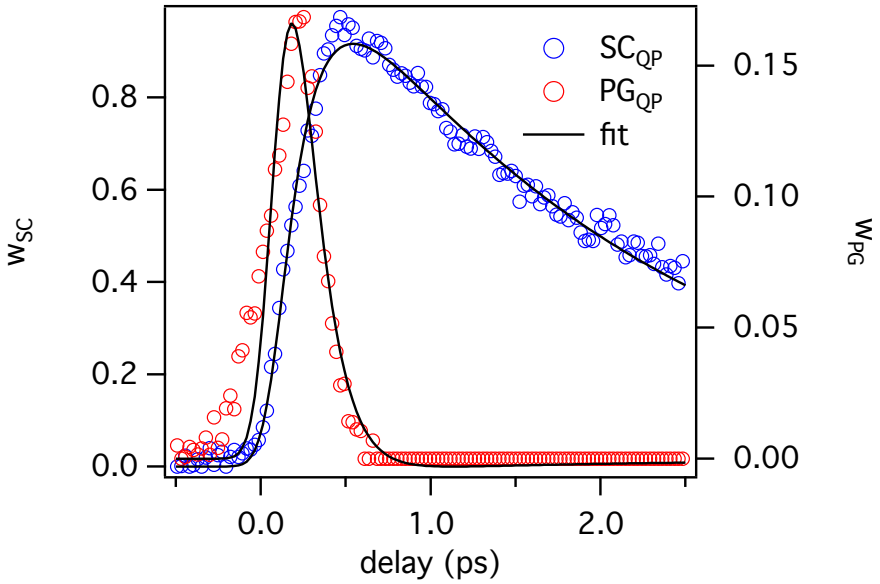


**Figure 6.11: Phase competition in the superconducting state at 20 $\mu J/cm^2$** - Dynamics of the normalized weights of the superconducting and pseudogap components at 20 $\mu J/cm^2$.

the minimum $w_{SC}$. This finding support the hypothesis of a spatially inhomogenous admixture of PG and SC phases.

## 6.3 Discussion: ultrafast dynamical phase competition

In this chapter I have reported novel experimental results on the photoinduced modifications of the spectral $\Delta R/R(\omega, t)$ response at high-fluence on an overdoped cuprate. The experiments have been done at 100 K and 10 K, both below and above the critical pump fluence, $\phi_{cr}$. The broad spectral range provided by the joint use of a supercontinuum pulse and a tunable OPA pulse represents an important upgrade to address the problem of the dynamical competition between pseudogap and superconducting states in HTSC. So far the problem has been studied through "single-color" optical pump-probe experiments

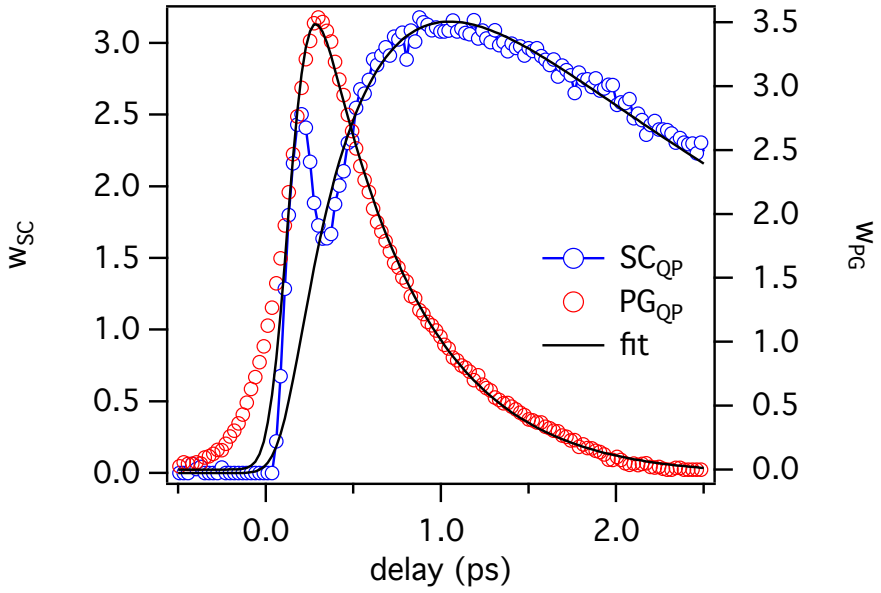


**Figure 6.12: Phase competition in the superconducting state at 250 $\mu J/cm^2$** - Dynamics of the normalized weights of the superconducting and pseudogap components at 250 $\mu J/cm^2$.

(30, 79, 127). With the "single-color" experimental approach is not possible to disentangle the $\Delta R/R(t)$ signal originated by PG and SC QPs when both are present (79), i.e., in the superconducting state. The spectral information on the reflectivity variation between 0.5 and 2.2 eV reported in this chapter provides a comprehensive picture of the dielectric function perturbation in both the intraband and the interband optical transitions region, allowing to distinguish several spectral components and to interpret them as a competition between SC and PG QPs.

Since the data reported in this chapter are considerably new, only a simple analysis of the data is presented. In particular a simple decomposition of the signal matrix into three fundamental signals (SC, PG and NS) have been done,

$$\frac{\Delta R}{R}(\omega, t) = \sum_i w_i(t) \frac{\Delta R_i}{R_i}(\omega) \tag{6.1}$$

where the $i$ components are the low-fluence responses in the SC, PG and NS phases. This decomposition is consistent with the SVD method adopted in section 4.4, with the difference of considering only three non-zero components and optimizing their singular value with least-mean squares fitting (see Chap. 3).

Strictly speaking the weights $w_i(t)$ obtained with this procedure are meaningful values only if the system under study is an inhomogeneous admixture of one or more macroscopic phases. To be more precise the inhomogeneity should have a length scale $d \gg \lambda/10$ (125, 126). This condition translates to $d \gg$200 nm for the broadband probe pulse used here. In this case the total reflectivity (and consequently its variations) will be the sum of the reflectivity of each phase.

For a homogeneous system where different excitations coexist producing distinct perturbations of the dielectric function the reflectivity is not separable into independent optical signals. The reason is that the perturbations act on different microscopic parameters of the dielectric function. Therefore the resulting reflectivity

$$R_{ex}(\omega) = \left| \frac{1 - \sqrt{\epsilon_{ex}(\omega)}}{1 + \sqrt{\epsilon_{ex}(\omega)}} \right|^2 \tag{6.2}$$

will not produce a $(\Delta R_{ex} - \Delta R_{eq})/R_{eq}$ separable into independent components.

Considering for example the case of k-space competition of PG and SC excitations, as recently suggested by Kondo et al. (17), the dielectric function would be perturbed by both QPs. Following the differential model proposed in sections 4.3.3 and 4.3.4, and considering both acting on the same system the optical response in this case can be obtained. In the following I will refer to this situation as *coexistence*, in the sense that PG and SC excitations are present on the same spatial region. The result is shown in Fig. 6.13 and compared to a simple algebraic sum of the two independent signals, $\Delta R/R_{PG}$ and $\Delta R/R_{SC}$.

The signal when SC and PG QPs coexist is significantly different from the algebraic sum of the two components. In particular it has two peculiar features, an intense negative $\Delta R/R$ at low energies (with a

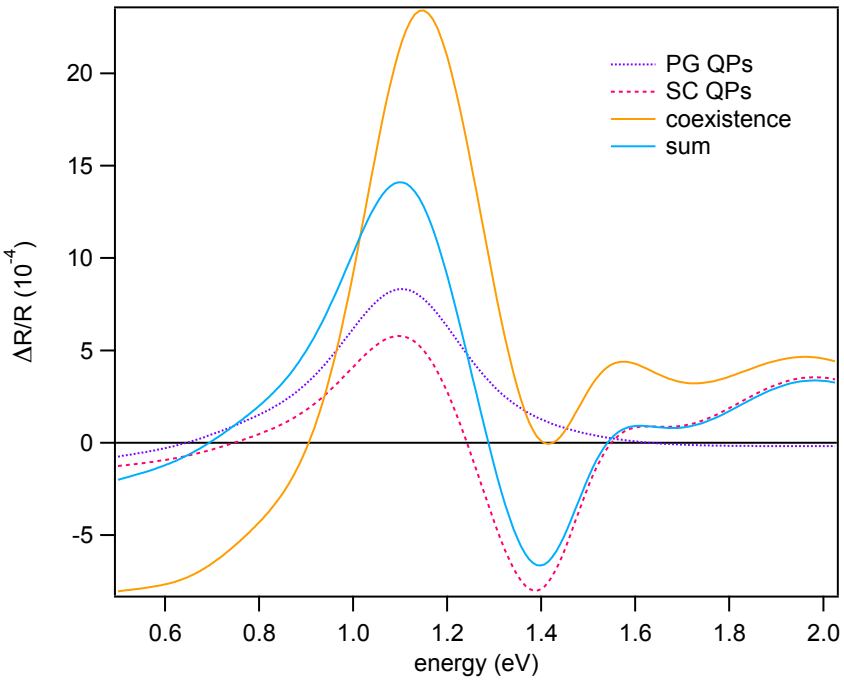


**Figure 6.13: Differential model for SC and PG coexistence** - Reflectivity variations obtained from the differential model for pseudogap quasi-particles 4.3.3, superconducting quasi-particles 4.3.4 (dashed lines) and a combination of the two perturbations (solid line) calculated including both effects for a differential model at 10 K. An algebraic sum of the two $\Delta R/R$ signals of the two kinds of QPs is also shown.

plateau at 0.6 eV) of the same magnitude of the dip at 1.4 eV typical of the SC response and a narrow peak (FWHM $\sim$ 0.2 eV) centered a 1.1 eV. This suggest that when $w_{SC}(t)$ and $w_{PG}(t)$ have a similar intensity these new spectral features should appear in the optical response. This is not observed in the experimental data reported in Fig. 6.5 and Fig. 6.6.

This suggests that above $\phi_{cr}$, where $w_{SC}(t)$ and $w_{PG}(t)$ are comparable, no coexistence of SC and PG QPs on the same microscopic area is observed. Therefore the dynamics reflects the signal coming from spatially separated phases. This is confirmed by the fact that the spectral features are successfully reproduced by a simple algebraic

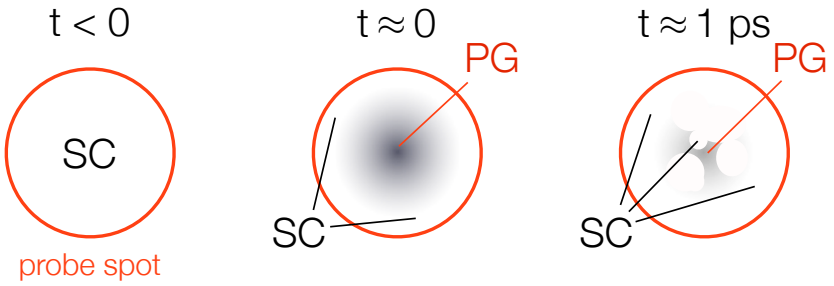


**Figure 6.14: SC and PG regions dynamics at high fluence** - Proposed model for the dynamical competition at high fluence. The probe laser spot have a diameter of 50-80 $\mu m$. The homogenous superconducting phase is probed at t $<$ 0. At t $=$ 0 the high fluence pump induces the phase transition to the pseudogap phase in a surrounding superconducting phase. At longer delay time the reconstruction dynamics of the superconducting phase is probed.

sum of $\Delta R/R$ components as expected for an inhomogeneous admixture of more phases with inhomogeneity length scale $d \gg$200 nm. This phase separation have been photoinduced by the pump light pulse as demonstrated by the discontinuity of $w_{PG}$ in the fluence dependence (Fig. 6.8). This result further confirms the picture of a PIPT happening at $\phi_{cr}$, while suggesting that the underlying ground state of the superconducting phase is the pseudogap rather than the normal state. This is evidenced by the fact that QPs with the same spectral response and the same relaxation time of the PG are appearing in the optical signal when the condensate vaporization has been photoinduced by the light pulse. The situation at different time delays is summarized in Fig. 6.14.

While the interpretation of the weights $w_i$ as meaningful volume fractions of the SC, PG and NS phases, is valid at high fluence where a signal originated by the coexistence of different kind of QPs should be clearly distinguished, this is not the case of the low fluence data, where the $w_{PG}$ is so low in respect to $w_{SC}$, that it is not possible to exclude the coexistence of these different kind of QPs. Here more refined models are needed to draw a conclusive interpretation.

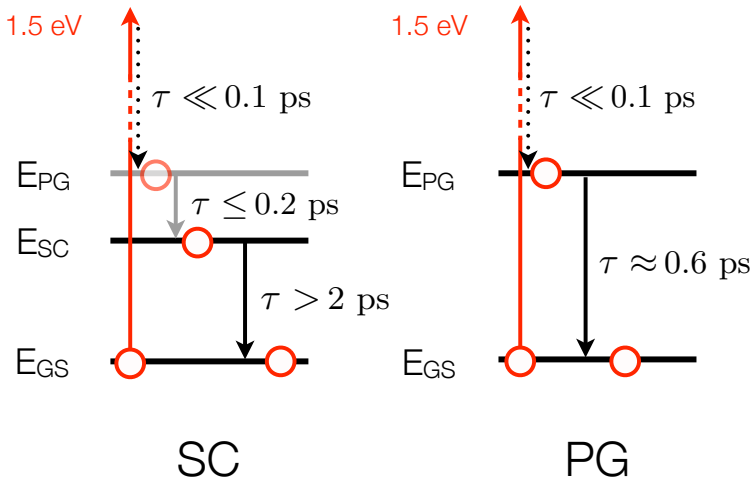


**Figure 6.15: QPs relaxation dynamics at low-fluence within the cascade model** - Quasiparticles relaxation dynamics at low-fluence in the superconducting and pseudogap phase interpreted within the cascade model proposed in (30, 127). Different excitations are here distinguished by their different energy scales. $E_{GS}$ is the ground state energy, $E_{SC}$ is the energy of superconducting quasiparticles, $E_{PG}$ is the one of pseudogap excitations, 1.5 eV is the pump photon energy. The lifetime of 1.5 eV excitation is extremely fast and bosons of energy $> 40$ meV are excited within $< 0.1$ ps as suggested in section 4.3.2. The relaxation times for excitations at $E_{SC}$ and at $E_{PG}$ are obtained from the experiments reported in this chapter. $E_{PG}$ is drawn in light grey to indicate the short lifetime and suppressed signal of PG excitations in the superconducting state at low-fluence.

However, independently to the fluence regime, the experiments highlight the competition of QPs in the *time-domain*. The relaxation dynamics of PG and SC QPs at 10 K are found to be consequential, with the decay time of the former coinciding (within 100 fs) with the rise time of the latter (Fig. 6.9). While at high-fluence this dynamics seems to be connected to a real-space macroscopic phase separation between PG and SC phases, with the SC phase reforming on the timescale of PG QP relaxation, in the low-fluence regime this consequential dynamics can also be explained by a cascade model (30, 127), where the initially photoinjected high-energy (1.5 eV) quasiparticles decay first into PG excitations, because of their higher energy scale, and subsequently

lower energy excitations, such as SC quasiparticles, are excited. This model is described in Fig. 6.15 for both superconducting and pseudogap phases at low-fluence, together with the experimentally measured decay times. The experiments reported in this chapter represent a benchmark for this model.

This model provide a possible phenomenological description of the dynamics at low-fluence. However an important question remains: what is the origin of the very fast decay time of PG excitations ($E_PG$) and the suppression of their signal observed in the superconducting state? This instability can be either related to very rapid conversion of PG excitations into SC excitations, or to highly unstable inhomogenous PG regions photoinduced at low-fluence as predicted by the $\mu^*$ model non-equilibrium phase diagram 2.9. More detailed analysis needs to be done to discriminate the two scenario.

In the following I summarize the most evident experimental results obtained in this chapter: i) at 10 K and at high fluence I observe a dynamical competition between PG and SC phases, ii) at the lowest fluence (20 $\mu J/cm^2$) the PG phase is suppressed (with the PG volume $< 1/5$ of the interaction volume in temporal coincidence, t = 0, while the PG phase would be completely absent after 0.2 ps), iii) the volume fraction occupied by PG phase strongly depends on fluence and it have a discontinuity at the critical fluence $\phi_{cr}$ when it starts dominating over the SC fraction, iv) the rise time of the SC fraction coincide with decay time of the PG fraction within 0.1 ps, v) above $\phi_{cr}$ the PG QPs relaxation dynamics is the limiting factor for the SC reformation.

These findings gives a consistent picture of the data in terms of a photoinduced spatial admixture of competing phases at high fluence. Strong dynamical competition between PG and SC phases is realized and measured in the *time-domain*. This competition will have to be compared to non-equilibrium models recently reported in the literature (30, 127, 128, 129) and to the predictions of theories of high-temperature superconductivity (9).

## 6.4 Conclusion

In this chapter I have exploited a novel time-resolved spectroscopic technique to show the real-time competition of PG and SC states above the critical fluence $\phi_{cr}$ for the PIPT described in chapter 5. Here I demonstrate that the transition is accompanied by the conversion of a large part of the volume fraction to the pseudogap phase. Some pseudogap quasiparticles signal appears also below $\phi_{cr}$ with a strongly fluence-dependent and extremely fast lifetime ($\tau < 0.6$ ps). The superconducting state reconstruction can be measured in real-time with this technique. I observe that the rate of the superconducting phase reformation is limited by the pseudogap QPs lifetime ($\tau \sim 0.6$ ps).

# Chapter 7

# Conclusions

In this Ph.D. thesis work a novel broadband optical spectroscopic time-resolved technique is presented and used for the study of HTSC. This technique allows the exploration of the spectral region from 0.5 eV to 2.2 eV. In this region each phase of the complex phase diagram of cuprates shows a different optical response. The results are discussed within the framework of the extended-Drude analysis, adopting a differential model for the dielectric function able to describe the non-equilibrium response of each phase considered. This novel technique provides compelling evidence of the crucial role of Cu-O mixed many-body excitations at 1.5 eV and 2.0 eV in the superconducting condensate formation.

A detailed analysis, based on the Rothwarf-Taylor equations, of the quasi-particles decay time in low-excitation conditions, allows us to recognize the decay time power-law divergence in the vicinity of the superconducting critical temperature. This finding set the basis for the understanding of the high-fluence regime, where an abrupt saturation of the superconducting time-resolved signal is observed. In facts, in the vicinity of this saturation fluence the decay time remains finite,

suggesting that the non-equilibrium superconducting gap, 1-2 ps after the pump pulse, is also finite and non-zero.

To quantitatively interpret the data, an extension of the Rothwarf-Taylor model in the case of a time-dependent superconducting gap has been proposed and applied. The final result is that within this model one can rule out a second-order quasi-thermal phase transition. The origin of the photoinduced phase transition is non-thermal and of first-order character. This finding set the basis for the study of the real-time dynamics of an admixture of competing phases after an impulsive *quench* of the superconducting phase.

The study of this transition through this novel time-resolved optical spectroscopic technique shows the establishment of an inhomogenous admixture, with a sudden increase of the volume fraction associated with the pseudogap phase. This allows to conclude that the pseudogap phase is the underlying ground state for superconductivity once the free energy is increased enough to cause the instability of the superconducting state. Moreover the fact that the rate for the reconstruction of superconducting phase is limited by the pseudogap QPs relaxation time suggests a competitive relationship pseudogap and superconducting quasi-particles.

# References


[1] Adrain Cho. *Nature*, **314**(5802):1072, 2006. 1

[2] A. Marouchkine. *Room-Temperature Superconductivity*. Cambridge International Science Publishing, Cambridge, 2004. 1

[3] P. J. Ford and G. A. Saunders. *The Rise of the Superconductors*. CRC Press, Boca Raton, London, New York, Washington, D. C., 2005. 1

[4] W.E Pickett. *J. Supercond. Nov. Magn,*, **19**(3-5):291–297, 2006. 1

[5] J. G. Bednorz and K. A. Muller. *Z. Phys. B: Condens. Matter*, **64**:189, 1986. 1

[6] C. C. Tsuei and J. R. Kirtley. *Rev. Mod. Phys.*, **72**:969, 2000. 1

[7] A. Damascelli, Z. Hussain, and Z.X. Shen. *Rev. Mod. Phys.*, **75**:473, 2003. 1, 14

[8] $\phi$. Fischer, M. Kugler, I. Maggio-Aprile, and C. Berthod. *Rev. Mod. Phys.*, **79**:353, 2007. 1

[9] P. A. Lee, N. Nagaosa, and X-G Wen. *Rev. Mod. Phys.*, **78**:17, 2006. and references therein. 1, 2, 4, 10, 11, 14, 80, 115

[10] L. Taillefer. *Ann. Rev. Cond. Matt. Phys.*, **1**:51, 2010. 1, 4, 14, 15

[11] D.N. Basov and T. Timusk. *Rev. Mod. Phys.*, **77**:721, 2005. 1, 11, 21

[12] T Timusk and B Statt. *Rep. Prog. Phys.*, **62**(1):61–122, 1999. 1, 13

## REFERENCES


[13] M.R Norman and C Pépin. *Rep. Prog. Phys.*, **66**(10):1547–1610, 2003. 2

[14] M. Schiró, M. Capone, M. Fabrizio, and C. Castellani. *Phys. Rev. B*, **77**(10):104522, 2008. 2

[15] C. Varma. *Nature*, **468**(7321):184, 2010. 2, 13, 14

[16] D. van der Marel. *Nat. Phys.*, **7**(1):10–11, 2011. 2, 13, 14

[17] T. Kondo, R. Khasanov, T. Takeuchi, J.Schmalian, and A. Kaminski. *Nature*, **457**(7226):296–300, 2009. 2, 15, 111

[18] R. Khasanov, T. Kondo, S. Strässle, D. Heron, A. Kaminski, H. Keller, S. Lee, and T. Takeuchi. *Phys. Rev. Lett.*, **101**(22):227002, 2008. 2, 15

[19] A Kanigel, U Chatterjee, M Randeria, M Norman, G Koren, K Kadowaki, and J Campuzano. *Phys. Rev. Lett.*, **101**(13):137002, 2008. 2, 15

[20] H-B Yang, J D Rameau, P D Johnson, T Valla, A Tsvelik, and G D Gu. *Nature*, **456**(7218):77, 2008. 2, 15

[21] S. Hufner, M. A. Hossain, A. Damascelli, and G. A. Sawatzky. *Rep. Prog. Phys.*, **71**:062501, 2008. 2, 12, 13, 14, 68, 72

[22] Micheal Tinkham. *Introduction to Superconductivity*. McGraw-Hill, Inc., 1996. 2, 66, 68, 74

[23] H.J.A. Molegraaf, C. Presura, D. van der Marel, P.H. Kes, and M.Li. *Science*, **295**:2239, 2002. 2, 62, 64

[24] A.B. Kuzmenko, H.J.A. Molegraaf, F. Carbone, and D. van der Marel. *Phys. Rev. B*, **72**:144503, 2005. 2

[25] L. R. Testardi. *Phys. Rev. B*, **4**:2189, 1971. 3, 23

[26] N Gedik, M Langner, J Orenstein, S Ono, Yasushi Abe, and Yoichi Ando. *Phys. Rev. Lett.*, **95**(11):117005, Sep 2005. 3, 33

[27] G Coslovich, C Giannetti, F Cilento, G Ferrini, and F Parmigiani. *AIP proceedings*, **1162**:177, 2009. 3, 25, 31, 33, 53, 80, 83, 86

[28] P Kusar, V.V Kabanov, J Demsar, T Mertelj, S Sugai, and D Mihailovic. *Phys. Rev. Lett.*, **101**:227001, 2008. 3, 25, 31, 32, 53, 80, 81, 83, 84, 86, 94, 95, 106

[29] C Giannetti, G Coslovich, F Cilento, G Ferrini, H Eisaki, N Kaneko, M Greven, and F Parmigiani. *Phys. Rev. B*, **79**:224502, 2009. 3, 25, 31, 53, 79, 80, 81, 83, 84, 91, 92, 93, 94, 95

[30] T Mertelj, V.V Kabanov, C Gadermaier, N.D Zhigadlo, S Katrych, J Karpinski, and D Mihailovic. *Phys. Rev. Lett.*, **102**:117002, 2009. 3, 25, 31, 53, 80, 81, 83, 95, 110, 114, 115

[31] A. Tomeljak, H. Schäfer, D. Städter, M. Beyer, K. Biljakovic, and J. Demsar. *Phys. Rev. Lett.*, **102**(6):066404, 2009. 3, 80, 81, 84, 94, 95

[32] R. Yusupov, T. Mertelj, V. V. Kabanov, S. Brazovskii, P. Kusar, J-H Chu, I. R. Fisher, and D. Mihailovic. *Nat. Phys.*, **6**(9):681, 2010. 3, 80, 81, 84, 94, 95

[33] S. Watanabe, R. Kondo, S. Kagoshima, and R. Shimano. *Phys. Rev. B*, **80**(22):220408, 2009. 3, 80, 81, 84, 94, 95

[34] C.S. Owen and D.J Scalapino. *Phys. Rev. Lett.*, **28**:1559, 1972. 3, 23, 24, 27, 79, 81, 84, 86, 91, 93, 94

[35] E.J. Nicol and J.P. Carbotte. *Phys. Rev. B*, **67**:214506, 2003. 3, 27, 29, 31, 79, 81, 84, 86, 89, 91, 92, 93, 94

[36] J. Nagamatsu, N. Nakagawa, T. Muranaka, Y. Zenitani, and J. Akimitsu. *Nature*, **410**(6824):63–64, 2001. 7

[37] Y. Kamihara, H. Hiramatsu, M. Hirano, R. Kawamura, H. Yanagi, T. Kamiya, and H. Hosono. *J. Am. Chem. Soc*, **130**:3296, 2008. 7

[38] H. Eisaki, N. Kaneko, D. L. Feng, A. Damascelli, P. K. Mang, K. M. Shen, Z.-X. Shen, and M. Greven. *Phys. Rev. B*, **69**(6):064512, 2004. 8, 41

[39] R.E. Gladyshevskii and R. Flukiger. *Acta Cryst. B*, **52**:38. 8

[40] V.J. Emery. *Phys. Rev. Lett.*, **58**:2794, 1987. 9

[41] C. M. Varma, S. Schmitt-Rink, and E. Abrahams. *Solid State Commun.*, **62**:681, 1987. 9

[42] J Zaanen, G Sawatzky, and J Allen. *Phys. Rev. Lett.*, **55**(4):418–421, 1985. 9, 66

[43] F.C. Zhang and T. Rice. *Phys. Rev. B*, **37**:3759, 1988. 10, 65

[44] N. B. Brookes, G. Ghiringhelli, O. Tjernberg, L. H. Tjeng, T. Mizokawa, T. W. Li, and A. A. Menovsky. *Phys. Rev. Lett.*, **87**:237003, 2001. 11

[45] S. Ishihara and N. Nagaosa. *Phys. Rev. B*, **69**(14):144520, 2004. 11

## REFERENCES


[46] M. R. Norman. *Phys. Rev. B*, **61**:14751, 2000. 12, 13

[47] C. Panagopoulos and T. Xiang. *Phys. Rev. Lett.*, **81**(11):2336–2339, 1998. 12

[48] K Tanaka, W. S Lee, D. H Lu, A Fujimori, T Fujii, Risdiana, I Terasaki, D. J Scalapino, T. P Devereaux, Z Hussain, and Z.-X Shen. *Science*, **314**(5807):1910–1913, 2006. 12, 13

[49] W. S. Lee, I. M. Vishik, K. Tanaka, D. H. Lu, T. Sasagawa, N. Nagaosa, T. P. Devereaux, Z. Hussain, and Z.-X. Shen. *Nature*, **450**(7166):81–84, 2007. 12, 13, 75

[50] M. R. Norman, D. Pines, and C. Kallin. *Adv. Phys*, **54**:715, 2004. 13

[51] W.N Hardy, D.A Bonn, D.C Morgan, R Liang, and K Zhang. *Phys. Rev. Lett.*, **70**(25):3999–4002, 1993. 13, 92

[52] T. Kondo, Y. Hamaya, A. D Palczewski, T. Takeuchi, J. S. Wen, Z. J. Xu, G. Gu, J. Schmalian, and A. Kaminski. *Nat. Phys.*, **7**(1):21–25, 2010. 13, 15

[53] Yuan Li, V Balédent, G Yu, N Barišić, K Hradil, R A Mole, Y Sidis, P Steffens, X Zhao, P Bourges, and M Greven. *Nature*, **468**(7321):283, 2010. 14

[54] M.R: Norman, D. Pines, and C. Kallin. *Adv. Phys.*, **54**:715, 2005. 14

[55] T Chien, Z Wang, and N Ong. *Phys. Rev. Lett.*, **67**(15):2088, 1991. 15

[56] P.B Allen. *Phys. Rev. B*, **3**(2):305–320, 1971. 16

[57] J.W Allen and J.C Mikkelsen. *Phys. Rev. B*, **15**(6):2952–2960, 1977. 16

[58] S.V Shulga, O.V Dolgov, and E.G Maksimov. *Physica C*, **178**(4-6):266–274, 1991. 17

[59] E. van Heumen, E. Muhlethaler, A. B. Kuzmenko, H. Eisaki, W. Meevasana, M. Greven, and D. van der Marel. *Phys. Rev. B*, **79**:184512,, 2009. 18, 19, 21, 57

[60] L. de Medici, X. Wang, M. Capone, and A. J. Millis. *Phys. Rev. B*, **77**:014518, 2009. 22

[61] F Carbone, A. B Kuzmenko, H. J. A Molegraaf, E Van Heumen, V Lukovac, F Marsiglio, D Van Der Marel, H Berger, S Courjault, P. H Kes, and M Li. *Phys. Rev. B*, **74**(6):064510, 2006. 23

[62] D Ginsberg. *Phys. Rev. Lett.*, **8**(5):204–207, 1962. 23

[63] B. Miller and A. Dayem. *Phys. Rev. Lett.*, **18**(23):1000–1004, 1967. 23

[64] A. Rothwarf and B.N. Taylor. *Phys. Rev. Lett.*, **19**:27, 1967. 23, 24, 26, 47, 69, 72

[65] V.V. Kabanov, D. Mihailovic, and J. Demsar. *Phys. Rev. Lett.*, **95**:147002, 2005. 23, 24, 25, 26, 31, 53, 70, 72, 73, 80, 83, 84, 86, 125

[66] G. A. Sai-Halasz, C. C. Chi, A. Denenstein, and D. N. Langenberg. *Phys. Rev. Lett.*, **33**:215, 1974. 23

[67] V. F. Elesin. *JETP*, **39**:862, 1974. 23

[68] W.H. Parker. *Phys. Rev. B*, **12**:3667, 1975. 23, 24, 27, 84, 86, 91, 93

[69] V. F. Elesin, V. E. Kondrashov, and A. S. Sukhikh. *Sov. Phys. Solid State*, **21**:1986, 1979. 23

[70] J. Demsar et al. *Phys. Rev. Lett.*, **91**:267002, 2006. 24, 31, 72

[71] N Gedik, P Blake, R.C Spitzer, J Orenstein, R Liang, D.A Bonn, and W.N Hardy. *Phys. Rev. B*, **70**:014504, 2004. 24, 25, 31, 32, 53, 72, 80, 83, 86, 90, 92

[72] V.V. Kabanov, J. Demsar, B. Podobnik, and D. Mihailovic. *Phys. Rev. B*, **59**:1497, 1999. 25, 31, 32, 53, 70, 72, 80, 83, 86, 93

[73] P Gay, D.C Smith, C.J Stevens, C Chen, G Yang, S.J Abell, D.Z Wang, J.H Wang, Z.F Ren, and J.F Ryan. *J. Low Temp. Phys.*, **117**:1025, 1999. 25, 31, 53, 80, 83

[74] P Gay, C.J Stevens, D.C Smith, C Chen, and J.F Ryan. *Physica C*, **341**:2221, 2000. 25, 31, 53, 80, 83

[75] D Dvorsek, V.V Kabanov, J Demsar, S.M Kazakov, J Karpinski, and D Mihailovic. *Phys. Rev. B*, **66**:0205100, 2002. 25, 31, 53, 55, 56, 70, 80, 83

[76] N. Gedik, M. Langner, and J.Orenstein. *Phys. Rev. Lett.*, **95**:117005, 2005. 25, 31, 53, 80, 83, 90, 126

[77] R. A. Kaindl, M. A. Carnahan, and D. S. Chemla. *Phys. Rev. B*, **72**:060510, 2005. 25, 31, 53, 72, 80, 83

[78] Elbert E. M Chia, D Talbayev, Jian-Xin Zhu, H. Q Yuan, T Park, J. D Thompson, C Panagopoulos, G. F Chen, J. L Luo, N. L Wang, and A. J Taylor. *Phys. Rev. Lett.*, **104**:027003, 2010. 25, 31, 53, 70, 73, 83, 95

## REFERENCES


[79] Y. H. Liu et al. *Phys. Rev. Lett.*, **101**:137003, 2008. 29, 70, 80, 86, 110

[80] S.D. Brorson et al. *Solid State Commun.*, **74**:1305, 1990. 30, 70

[81] P. B. Allen. *Phys. Rev. Lett.*, **59**:1460, 1987. 30, 57, 59, 70

[82] S.D. Brorson et al. *Phys. Rev. Lett.*, **64**:2172, 1990. 30, 70

[83] L Perfetti, P.A Loukakos, M Lisowski, U Bovensiepen, H Eisaki, and M Wolf. *Phys. Rev. Lett.*, **99**:197001, 2007. 30, 57, 60, 81, 95

[84] F. Carbone, D.S. Yanga, E. Giannini, and A. H. Zewail. *Proc. Natl. Acad. Sci.*, **105**:20161, 2008. 30, 57, 60, 81, 95

[85] R.A Kaindl, M Woerner, T Elsaesser, D C Smith J.F Ryan, G.A Farnan, M.P McCurry, and D.G Walmsley. *Science*, **287**(5452):470–473, 2000. 31

[86] S.G. Han et al. *Phys. Rev. Lett.*, **65**:2708, 1990. 31

[87] A. Frenkel. *Phys. Rev. B*, **48**:9717, 1993. 31

[88] S.A Kovalenko, A.L Dobryakov, J Ruthmann, and N.P Ernsting. *Phys. Rev. A*, **59**(3):2369–2384, 1999. 33

[89] C.H. Brito Cruz, W.H. Knox R.L. Fork, and C.V. Shank. *Chem. Phys. Lett.*, **132**(4-5):341–344, 1986. 33

[90] W.T. Pollard, C.H. Brito Cruz, C.V. Shank, and R.A. Mathies. *J. Chem. Phys.*, **90**(1):199, 1989. 33

[91] F. Cilento, C. Giannetti, G. Ferrini, S. Dal Conte, T. Sala, G. Coslovich, M. Rini, A. Cavalleri, and F. Parmigiani. *Appl. Phys. Lett.*, **96**:021102, 2010. 33, 95

[92] Mira Seed and Rega 9050, manuals, Coherent Inc. 34

[93] T. Abebaw. Master's thesis. 34, 43

[94] M. E. Wall, A. Rechtsteiner, and L. M. Rocha. In *A Practical Approach to Microarray Data Analysis*. Kluwer, Norwell, 2003. 44

[95] E. R. Henry. *Biophys. J.*, **72**:652, 1997. 44

[96] P. Doruker, A. R. Atilgan, and I. Bahar. *Proteins*, **40**:512, 2000. 44

[97] O. Alter, P. O. Brown, and D. Botstein. *Proc. Natl. Acad. Sci.*, **97**:10101, 2000. 44

[98] M. Schmidt, S. Rajagopal, Z. Ren, and K. Moffat. *Biophys. J.*, **84**:2112, 2002. 44

[99] M Holcomb, C Perry, J Collman, and W Little. *Phys. Rev. B*, **53**(10):6734–6751, 1996. 51, 65

[100] J Demsar, B Podobnik, V.V Kabanov, Th Wolf, and D Mihailovic. *Phys. Rev. Lett.*, **82**:4918, 1999. 55, 70, 80

[101] J Hohlfeld, S.-S Wellershoff, J Güdde, U Conrad, V Jähnke, and E Matthias. *Chem. Phys.*, **251**(1-3):237–258, 2000. 55

[102] C.-K Sun, F Vallée, L.H Acioli, E.P Ippen, and J.G Fujimoto. *Phys. Rev. B*, **50**(20):15337–15348, 1994. 55

[103] E. G. Maksimov. *Phys.-Usp.*, **43**(10):965–990, 2007. 58

[104] J. E. Hirsch and F. Marsiglio. *Phys. Rev. B*, **62**:15131, 2000. 64

[105] M. R. Norman and C. Pepin. *Phys. Rev. B*, **66**:100506(R), 2002. 64

[106] C. Giannetti, F. Cilento, S. Dal Conte, G. Coslovich, G. Ferrini, H. Molegraaf, M. Raichle, R. Liang, H. Eisaki, M. Greven, A. Damascelli, D. van der Marel, and F. Parmigiani. *Submitted to Nat. Commun.* 68

[107] M. Tinkham and J. Clarke. *Phys. Rev. Lett.*, **28**:1366, 1972. 70

[108] A. Schmidt and G. Schon. *J. Low Temp. Phys.*, **20**:207, 1975. 70

[109] Eq. (4.7) is valid as long as $n_T << N_T$, where $N_T$ is the boson population density at equilibrium. The limit $n_T \sim N_T$ is achieved only in the close vicinity of $T_C$ (see Ref. (65) ). Fig. 4.17a clearly shows that $n_T$ decreases rapidly below $T_C$, setting the condition $n_T << N_T$. Thus we assume Eq. (4.7) to be valid few degrees below $T_C$. 72, 75, 94

[110] To obtain the value of the constant $n_{ph}$ contribution to the decay rate we use the experimental values of $\gamma$ at 38 K (Fig. 4.17)a and at 10 K, $\sim 4$ $\mu$J/cm$^2$ (Fig. 5.6a). We assume $\Gamma(T, \Delta)$ to be constant below 40 K (inset of Fig. 4.17b) and $n_T(10K) = 0$. Thus we have $\gamma(38K) = \Gamma_0 * (n_T + n_{ph})$ and $\gamma(10K) \sim \Gamma_0 * (n_{ph})$, from which we derive both $\Gamma_0$ and $n_{ph}$. 74

[111] S. Hufner and F. Muller. *Phys. Rev. B*, **78**(1):014521, 2008. 75

[112] A Yazdani. *J. Phys.: Condens. Matt.*, **21**(16):164214, 2009. 75

[113] C.J Lobb. *Phys. Rev. B*, **36**(7):3930–3932, 1987. 75

## REFERENCES


[114] A.I Sokolov. *Physica C*, **174**(1-3):208–214, 1991. 75

[115] A Junod, A Erb, and C Renner. *Physica C*, **317-318**:333–344, 1999. 75

[116] R.P Saichu, I Mahns, A Goos, S Binder, P May, S.G Singer, B Schulz, A Rusydi, J Unterhinninghofen, D Manske, P Guptasarma, M.S Williamsen, and M Rübhausen. *Phys. Rev. Lett.*, **102**:177004, 2009. 81, 95

[117] C. Giannetti, G. Zgrablic, C. Consani, A. Crepaldi, D. Nardi, G. Ferrini, G. Dhalenne, A. Revcolevschi, and F. Parmigiani. *Phys. Rev. B*, **80**:235129, 2009. 81, 95

[118] J Unterhinninghofen, D Manske, and A Knorr. *Phys. Rev. B*, **77**(18):180509, 2008. 86

[119] N. Cao, Y.-F. Wei, J.-M. Zhao, S.-P. Zhao, Q.-S. Yang, Z.-G. Zhang, and P.-M. Fu. *Chin. Phys. Lett.*, **25**(6):2257–2260, 2008. 86

[120] The slope obtained in this work in the range form 1 to 10 $\mu J/cm^2$ is 0.02 $\mathrm{ps}^{-1}/\mu J/cm^2$, which is compatible, within the experimental uncertainty, with the substantially constant decay rate measured by Gedik et al.(76) in the range from 0.1 to 1 $\mu J/cm^2$. 90

[121] R Cortes, L Rettig, Y Yoshida, H Eisaki, M Wolf, and U Bovensiepen. *arXiv.1011.1171v1*, 2010. 92

[122] P Howell, A Rosch, and P Hirschfeld. *Phys. Rev. Lett.*, **92**(3):037003, 2004. 92

[123] E. M. Lifshitz and L. P. Pitaevskii. *Physical Kinetics*. Butterworth-Heinemann, Oxford, 1981. 93

[124] G Doll, J Steinbeck, G Dresselhaus, M Dresselhaus, A Strauss, and H Zeiger. *Phys. Rev. B*, **36**(16):8884–8887, 1987. 104

[125] Thomas Mayerhöfer. *Journal of Optics A: Pure and Applied Optics*, **4**:540, 2002. 104, 111

[126] T Mayerhofer and J Popp. *Vibrational Spectroscopy*, **42**(1):118–123, 2006. 104, 111

[127] G Bianchi, C Chen, M Nohara, H Takagi, and J Ryan. *Phys. Rev. B*, **72**(9):094516, 2005. 110, 114, 115

[128] M. Schiró. *Phys. Rev. B*, **81**(8):085126, 2010. 115

[129] M. Schiró and M. Fabrizio. *Phys. Rev. Lett.*, **105**(7):076401, 2010. 115

# Publication List

- **G. Coslovich**, C. Giannetti, F. Cilento, G. Ferrini, and F. Parmigiani

  *"Quasi-particles dynamics in underdoped Bi2212 under strong optical perturbation"*

  AIP Conference Proceedings **1162**, pp. 177-185 (2009)

- C. Giannetti, **G. Coslovich**, F. Cilento, G. Ferrini, H. Eisaki, N. Kaneko, M. Greven and F. Parmigiani.

  *"Discontinuity of the ultrafast electronic response of underdoped superconducting $Bi_2Sr_2CaCu_2O_{8+x}$ strongly excited by ultrashort light pulses".*

  Physical Review B **79**, 224502 (2009), arXiv:0804.4822

  *This paper was selected for the Virtual Journal of Applications of Superconductivity*

  *This paper was selected for the Virtual Journal of Ultrafast Science*

- F. Cilento, C. Giannetti, G. Ferrini, S. Dal Conte, T. Sala, **G. Coslovich**, M. Rini, A. Cavalleri, F. Parmigiani.

  *"Ultrafast insulator-to-metal phase transition as a switch to measure the spectrogram of a supercontinuum light pulse".*

  Applied Physics Letters **96**, 021102 (2010), arxiv:0910.3785

- **G. Coslovich**, C. Giannetti, F. Cilento, S. Dal Conte, G. Ferrini, P. Galinetto, M. Greven, H. Eisaki, M. Raichle, R. Liang, A. Damascelli, and F. Parmigiani.
  *"Evidence for a photoinduced nonthermal superconducting-to-normal-state phase transition in overdoped* $Bi_2Sr_2Ca_{0.92}Y_{0.08}Cu_2O_{8+\delta}$*"*
  Physical Review B **83**, 064519 (2011), arXiv:1005.4320
- C. Giannetti, F. Cilento, S. Dal Conte, **G. Coslovich**, G. Ferrini, H. Molegraaf, M. Raichle, R. Liang, H. Eisaki, M. Greven, A. Damascelli, D. van der Marel and F. Parmigiani.
  *"Revealing the high-energy electronic excitations underlying the onset of high-temperature superconductivity in cuprates".*
  *submitted to Nature Communications*
- S. Dal Conte, C. Giannetti, F. Cilento, **G. Coslovich**, G. Ferrini, M. Raichle, R. Liang, A. Damascelli, and F. Parmigiani.
  *"Disentangling the electronic and phononic glue in high-Tc superconductors"*
  *in preparation*
- **G. Coslovich**, C. Giannetti, F. Cilento, S. Dal Conte, G. Ferrini, M. Raichle, R. Liang, A. Damascelli, and F. Parmigiani.
  *"The relation between pseudogap and superconductivity: Causality or Casualty?"*
  *in preparation (preliminary title)*

# Acknowledgements

First I would like to thank deeply my supervisor prof. Fulvio Parmigiani who has always supported me. He greatly stimulated my research activity and encouraged me to look forward in any case. I'm very grateful to Claudio Giannetti, my point of reference from the very beginning, thanks for the long time passed discussing about the physics behind our results. Many thanks to Federico Cilento, Stefano Dal Conte, Davide Bossini and Tadesse Abebaw who worked hard, days and nights, with me in the lab, I have really enjoyed working with you! Thanks to prof. Michele Fabrizio and prof. Uwe Bovensiepen who accepted to be referees of this thesis work, I'm grateful for your comments and suggestions. I acknowledge prof. Andrea Damascelli, prof. Gabriele Ferrini and Marco Schiró for fruitful discussions.

# Ringraziamenti

I ringraziamenti piú personali ovviamente in italiano. La fine del mio dottorato coincide anche con la fine della mia permanenza a Trieste e sono tante le cose che lascio qui. Questo non é solo il momento dei ringraziamenti quindi, ma anche dei saluti.

Grazie alla mia famiglia, a cui devo tutto.

Grazie nuovamente a Fulvio per tutto quello che ha fatto per me in questi anni e al gruppo T-ReX nella sua interezza per come mi ha fatto sentire a casa. Grazie ancora a Claudio per il suo instancabile entusiasmo e a tutto il gruppo di Brescia con cui ho condiviso soprattutto l'inizio di questo dottorato.

Grazie di cuore agli abitanti di casa Ardessi e a tutti gli amici che l'hanno animata. Sono fortunato ad avere vicino persone come voi. Vi aspetto tutti in California! (dove esporteremo l'osmiza prima o poi...)

Grazie ad Anna che mi é stata vicina in questi anni e mi ha sopportato piú di tutti! Le nostre strade si dividono, ma non i nostri cuori.

Infine grazie ai Trabant. Ancora non mi capacito dei quasi centomila chilometri percorsi assieme e degli oltre cento concerti fatti durante questo dottorato... Suonare con voi é sempre stata un'emozione indescrivibile. E grazie Michele anche per gli spunti grafici per la copertina!